Title

Towards establishing a human pluripotent stem cell-based in vitro model of dominant optic atrophy

Author

Pohl, Katherine Anne

Publication Date

2023

Peer reviewed|Thesis/dissertation

UNIVERSITY OF CALIFORNIA

Los Angeles

Towards establishing a human pluripotent stem cell-based *in vitro* model of dominant optic atrophy

A dissertation submitted in partial satisfaction of the requirements for the degree Doctor of Philosophy in Molecular Biology

by

Katherine Anne Pohl

2023

ABSTRACT OF THE DISSERTATION

Towards establishing a human pluripotent stem cell-based *in vitro* model of dominant optic atrophy

by

Katherine Anne Pohl

Doctor of Philosophy in Molecular Biology

University of California, Los Angeles, 2023

Professor Xian-Jie Yang, Chair

Dominant optic atrophy (DOA) is the most prevalent genetic optic neuropathy, affecting roughly 1:12,000 to 1:50,000 individuals worldwide. DOA patients exhibit retinal ganglion cell (RGC) degeneration, which leads to progressive bilateral vision loss. The majority of DOA cases are caused by mutations in the nuclear gene *optic atrophy 1* (*OPA1*), which encodes a dynamin-related GTPase that localizes to the inner mitochondrial membrane. Although *OPA1* is ubiquitously expressed in all human tissues, RGCs appear to be the primary cell type affected by *OPA1* mutations. It is therefore essential to study DOA in human RGCs to understand how an *OPA1* deficiency renders them particularly susceptible to degeneration. To overcome the scarcity of human RGCs, we have focused on establishing *in vitro* DOA disease models using human pluripotent stem cell (PSC)-derived 3D retinal organoids (ROs) that spontaneously develop human RGCs. We have established isogenic, *OPA1* mutant, human embryonic stem cell (ESC) lines using CRIPSR-Cas9 gene editing as well as induced pluripotent stem cell (iPSC) lines from DOA patients with distinct *OPA1* mutations. To derive isogenic control iPSCs, we have also corrected one DOA patient's mutation by performing CRISPR-Cas9-mediated

homology directed repair (HDR). Western blot analysis demonstrates that wild-type (WT) and *OPA1* heterozygous mutant PSCs have similar expression levels of the same five OPA1 protein isoforms and that the five isoforms are expressed relatively equally to one another. As expected, total OPA1 protein levels are reduced in PSCs that contain heterozygous *OPA1* nonsense mutations and are restored to WT control levels in an isogenic corrected line. Additionally, *OPA1* homozygous loss of function ESCs lack OPA1 expression. Structured illumination microscopy (SIM) reveals the *OPA1* homozygous loss-of-function ESCs have an altered mitochondrial morphology from WT PSCs and from PSCs with *OPA1* haploinsufficiency. Finally, cellular respiration assays show that *OPA1* mutant PSCs have significantly lower oxygen consumption rates (OCR) and mitochondrial ATP production rates than isogenic WT control PSCs. As expected, heterozygous *OPA1* mutant PSCs can derive 3D retinal organoids and develop RGCs. Like PSCs, WT and *OPA1* mutant ROs express the same OPA1 protein isoforms, but unlike PSCs, ROs express certain OPA1 protein isoforms more strongly than others. Research is ongoing to characterize the *OPA1* mutant ROs and RGCs in order to evaluate their potential use as reliable human models of DOA. Ultimately, when compared with ROs derived from their isogenic controls, these *OPA1* mutant, *human* PSC-derived RO disease models can reveal novel insights regarding the molecular mechanisms underlying the RGC-specific degeneration observed in DOA patients and facilitate the development of therapies that preserve or rescue vision in these patients.

The dissertation of Katherine Anne Pohl is approved.

Steven Andrew Barnes

April Dawn Pyle

Alfredo A. Sadun

Alexander M. Van der Bliek

Xian-Jie Yang, Committee Chair

University of California, Los Angeles

2023

DEDICATION

To the pursuit of knowledge.

TABLE OF CONTENTS

LIST OF FIGURES

CHAPTER 2

CHAPTER 3

CHAPTER 4

LIST OF TABLES

CHAPTER 2

CHAPTER 3

CHAPTER 4

ACKNOWLEDGMENTS

All the work described in the dissertation was directed by Dr. Xian-Jie Yang. Dr. Yang, thank you for working with me to design and pioneer a novel research project that incorporated my interests in stem cell biology and gene editing. You have prepared me to take on whatever may lie ahead.

I would like to thank my committee members, Drs. Steven Barnes, April Pyle, Alfredo Sadun, and Alexander Van der Bliek, for their scientific expertise and valuable insights, as well as for their support and words of encouragement throughout my PhD journey.

I would like to thank both my former and my current Gene Regulation, Epigenomics, and Transcriptomics (GREAT) home area directors, Dr. Mike Carey and Dr. Tom Vallim. Dr. Carey, thank you for supporting me from the very beginning and for pushing me to apply for the F31 predoctoral NRSA. Dr. Vallim, thank you for your dedication to your students. You approach situations both logically and compassionately, and I am so appreciative of the support you have given me. Thank you as well, to the wonderful SAOs of the MBIDP, you are much appreciated!

I would like to thank all of my former scientific mentors/principal investigators (PIs) whom I worked under prior to beginning my PhD: Dr. Janet Klein, PhD; Dr. Steven L'Hernault, PhD; and Dr. John Chute, MD.

I would like to thank the following members of the Yang Lab (past and present) for their scientific and technical support and insights, as well as for their camaraderie over the years: Kevin Nguyen, Johnny Ji, Thao Nguyen, Duc Hoang, Gary Qiao, Meera Suresh, Kun Do Rhee, and especially Xiangmei Zhang. May, thank you for being an outstanding teacher, scientific research partner,

“lab mom,” and friend to me over the past 5+ years. Your patience, compassion, and guidance are unmatched.

Thank you to all of my friends for the conversations, advice, and support, as well as the laughs, outings, and drinks. You continue to enrich my life and keep me grounded.

Lastly, I would like to thank my family—my mother, Julie, my late father, Dan Pohl, and my sisters, Claire and Emily—for always supporting my aspirations to study science and for their kind words and acts of encouragement. Thank you for providing me with the space I needed to accomplish my goals, and for being there when I needed you. I would also like to thank my parents for always valuing and encouraging my education.

CHAPTER 2 is a version of the manuscript that was accepted to *Frontiers in Genetics* (https://doi.org/10.3389/fgene.2023.1251216). KAP, XJY, and AAS contributed to the conception and design of the study. AHP and AAS identified DOA patients eligible to participate in the study. KAP and XJY wrote the IRB protocol used in the study. AAS and JAC interpreted DOA patient clinical data. KAP and XZ performed experiments described in the manuscript. KAP and XJY wrote the manuscript, and AAS and JAC contributed to the manuscript editing. The authors would like to thank the participating patients, the Cedars-Sinai Medical Center iPSC core in Los Angeles, and Rustum Karanjia, William Sultan, and Irene Tsui for their clinical assistance.

CHAPTER 3 is in preparation for publication.

Pohl, K.A., Zhang, X., Ji, J., Stiles, L., and Yang, X-J. The impact of *OPA1* heterozygous and homozygous loss-of-function mutations on the morphology and function of human pluripotent stem cell mitochondria. “In preparation”

KAP and XJY contributed to the conception and design of the study. KAP, XZ, LS, and JJ performed the experiments and KAP, LS, and XJY analyzed the results. KAP wrote the chapter, which is a modified and extended version of the manuscript that will be submitted for publication.

CHAPTER 4 details work that is part of an ongoing research project. KP and XZ performed the experiments and analyzed the results.

The work in this dissertation was supported by NIH grant 2R01EY026319 and CIRM grant DISC2-13475 awarded to XJY, NIH grants 5T32EY007026 and F31EY033242 awarded to KAP, NIH core grant P30EY000331, and an unrestricted grant from Research to Prevent Blindness to the Department of Ophthalmology at University of California, Los Angeles.

VITA

Education

Emory University, Atlanta GA

Bachelor of Science in Biology, Minor in Art History (2015)

Publications

Pohl, K.A., Zhang, X., Pham, A., Chan, J., Sadun, A. and Yang, X-J. Establishing induced pluripotent stem cell lines from two dominant optic atrophy patients with distinct *OPA1* mutations and clinical pathologies. *Frontiers in Genetics* **14** (2023). https://doi.org:10.3389/fgene.2023.1251216

Presentations

Pohl, K., Zhang, X., Yang, X.-J. "Establishing a Dominant Optic Atrophy Disease Model Using Human Pluripotent Stem Cell-derived Retinal Ganglion Cells". (2023, February 20). Invited talk at the XXV Biennial Meeting of the International Society for Eye Research. Gold Coast, Australia.

Selected Honors and Awards

NIH F31 Ruth L. Kirschtein Predoctoral Individual National Research Service Award (2021 – 2023)

International Society for Eye Research (ISER) Travel Fellowship Award (2023)

First Place Speaker Award (of 10 talks), Vision Science Division, Stein Eye Institute, University of California, Los Angeles (2022)

NIH T32 Vision Science Training Grant Recipient, Ruth L. Kirschtein National Research Service Award (2018 – 2021)

UCLA Graduate Dean's Scholar Award (2017)

Leadership and Activities

2021-2023 *New Ventures Innovation Fund Fellow,* UCLA Technology Development Group (TDG), Los Angeles, CA

2021-2023 *Graduate Student Representative,* Student Health Advisory Committee, UCLA, Los Angeles, CA

2021-2023 *UCLA Graduate Student Representative,* University of California Student Health Insurance Plan (UC SHIP) Executive Oversight Board

2020 *Teaching Assistant*, Cell Biology of the Nucleus (MIMG 132), Department of Microbiology, Immunology, and Molecular Genetics, UCLA, Los Angeles, CA

2019 *Teaching Assistant*, Molecular Biology of Cellular Processes (MCDB 144), Department of Molecular, Cell, and Developmental Biology, UCLA, Los Angeles, CA

CHAPTER 1

Introduction

1.1 The human retina

The retina is part of the central nervous system (CNS) and is formed from neuroectoderm. As the neural tube develops, it forms two, bilateral protrusions called the optic vesicles. The earliest signs of retinal development occur at four weeks gestation when the optic vesicles invaginate to form optic cups[1-3]. The inner layer of the optic cup becomes the neural retina, which enables vision by detecting light and converting it into chemical and electrical signals that are transmitted to the brain for visual processing via the optic nerve[4]. Located in the posterior of the eye, the retina is a highly structured, multilayered tissue composed of the following layers (from anterior to posterior): the inner limiting membrane (ILM), retinal nerve fiber layer (RNFL), ganglion cell layer (GCL), inner plexiform layer (IPL), inner nuclear layer (INL), outer plexiform layer (OPL), outer nuclear layer (ONL), outer limiting membrane (OLM), and photoreceptor layer[1,5]. These layers are largely defined by where the cell bodies and synaptic projections of the five main classes of retinal neurons, the ganglion cells, amacrine cells, bipolar cells, horizontal cells, and photoreceptors, reside. The GCL contains the retinal ganglion cell (RGC) bodies, the INL contains the amacrine, horizontal, and bipolar cell bodies, and the ONL contains the photoreceptor (rod and cone) cell bodies. The photoreceptor layer is composed of the inner and outer segments of the rods and cones, which capture and transduce light into electrochemical signals. Photoreceptors synapse with bipolar and horizontal cells in the OPL, and bipolar and amacrine cells synapse with RGCs in the IPL. These synapses belong to either the vertical or lateral signaling pathways. Vertically, the light-sensing photoreceptors transmit visual information to the RGCs through bipolar interneurons. The RGCs then serve as projection neurons to transmit this information to the brain via their long axons that run horizontally along the RNFL and converge to form the optic nerve. Laterally, horizontal and amacrine interneurons provide feedback and

feedforward signals between photoreceptors and bipolar cells, and between bipolar cells and RGCs, respectively[1,5]. Lastly, the two limiting membrane layers, the ILM and OLM, are formed in part by the most common glial cells in the retina, the Müller glia. The Müller glia span the entirety of the retina and provide key structural and metabolic support to retinal tissue. Adherens junctions between Müller glia and photoreceptor inner segments form the OLM, and Müller glia endfeet interact with basement membrane and extracellular matrix proteins at the ILM[6,7]. Inherent or extrinsic factors that damage or alter the function of any of these cell types can lead to gradual or acute vision loss.

1.2 Focus of the dissertation

This dissertation focuses on one of the most prevalent inherited optic neuropathies (IONs), dominant optic atrophy (DOA). Broadly speaking, any condition that involves damage to the optic nerve (which often results in vision loss) is considered an optic neuropathy. Interestingly, the most common inherited optic neuropathies, DOA and Leber's hereditary optic neuropathy (LHON), result from mitochondrial dysfunction. In the case of DOA, patients harbor mutations in nuclear genes that encode proteins with mitochondrial functions. In the case of LHON, patients harbor mitochondrial DNA mutations that affect complex I of the electron transport chain[8,9]. Although all of a patient's cells harbor his/her respective disease-causing mutation, the cells that make up the optic nerve, the RGCs, exhibit a particular vulnerability to the mitochondrial dysfunction that results in their degeneration. This necessitates that researchers studying IONs examine human RGCs specifically (as opposed to other cell types) to understand which of the cells' unique morphological features, molecular characteristics, and/or functional requirements render(s) them particularly prone to degeneration.

Existing hypotheses surrounding RGCs' vulnerability to mitochondrial defects center around the cells' high energy requirements and unique morphology. RGCs have one of the highest energy demands in the body as they need to transmit visual signals generated by the

photoreceptors over 50 mm to targets in the brain. They are also extremely prone to defects since they are exposed to ultraviolet (UV) light and have partially unmyelinated axons to maintain visual transparency. RGCs' long axons run unmyelinated along the inner retina to compose the RNFL, and only become myelinated after they turn ninety degrees, converge to form the optic nerve, and cross the lamina cribrosa to exit the eye[9]. RGC dendrites also require a large amount of energy, and predominantly use oxidative phosphorylation to generate ATP[10].

To meet this high energy requirement and to function normally, RGC mitochondria must be highly efficient and adaptable. This requires a delicate balance between mitochondrial biogenesis, fission and fusion, mitophagy, and transport. Mitochondria are predominately generated in the cell soma and are trafficked via microtubules to other areas of the neuron. Healthy RGCs have mitochondria in the soma, hillock, nodes of Ranvier, and synaptic regions, although the majority are concentrated in varicosities in the unmyelinated portion of the axon[11,12]. This makes sense, as the unmyelinated area of the axons requires more energy to generate action potentials due to the absence of saltatory conduction[13]. During development, RGC mitochondria are highly mobile. However, upon maturation of the RGC, mitochondria become more stationary at synapses, demonstrating their sustained need at sites of high energy. Interestingly, under stress conditions, mitochondria become mobile again, suggesting a need for heightened energy mobilization to other sites post-injury. Defects in trafficking preventing mitochondria from occupying high-energy sites are also hypothesized to have a role in RGC degeneration[11].

Unfortunately, hypotheses that RGCs' vulnerability to mitochondrial defects centers around the cells' high energy requirements and unique morphology have been difficult to prove. Studies of human RGCs have been historically difficult due to the rarity of primary retinal tissues (which cannot be cultured indefinitely) and scarcity of RGCs, which only comprise ~2% of the total retinal cells[14-16]. Consequentially, other human cell types have been used to study *OPA1* (the primary gene mutated in DOA patients) in relation to DOA[17,18]. However, these cell types are not

functionally, molecularly, or morphologically similar to RGCs and do not address why RGCs are preferentially prone to degradation[19-21]. Furthermore, animal models with differing *OPA1* mutations are nonuniform in their disease presentation and mitochondrial phenotypes, preventing overarching conclusions about *OPA1*-mediated DOA disease mechanisms from being made[22-32]. Recent single-cell transcriptomic analyses have also shown that human RGCs are quite different from rodent RGCs[33,34]. Therefore, although these studies have revealed insights into *OPA1*'s mitochondrial roles, the gene's particular functional requirement in human RGCs that would explain their susceptibility to degeneration is still not known.

The work described in this dissertation seeks to address the significant unmet need for human RGC models of DOA, which will allow researchers to examine the pathological mechanisms present in DOA patients' RGCs that render them particularly prone to degenerate. In the following chapters, I describe our efforts in establishing human pluripotent stem cell (PSC)-derived 3D retinal organoids (ROs) that produce RGCs, and discuss their potential to serve as *in vitro* DOA disease models. In Chapters 2 and 3, I generated multiple *OPA1* mutant, human PSC lines that can serve as starting material from which to develop DOA RGCs. I first derived induced pluripotent stem cell (iPSC) lines from DOA patients with distinct *OPA1* mutations and then additionally established embryonic stem cell (ESC) lines with heterozygous and homozygous *OPA1* mutations using CRISPR-Cas9 gene editing. After characterizing the molecular and mitochondrial effects these *OPA1* mutations have at the PSC level (Chapter 3), I examine the PSC lines' ability to develop into retinal organoids and RGCs (Chapter 4).

1.3 Dominant Optic Atrophy

1.3.1 DOA: Causes and symptoms

Dominant optic atrophy (DOA; OMIM #165500) is the most prevalent inherited optic neuropathy, affecting an estimated 1:10,000 to 1:50,000 individuals, depending on geographic location[35-40]. DOA is characterized by the loss of retinal ganglion cells (RGCs), which leads to

progressive, bilateral vision loss that is usually detectable in the first or second decade of life. A clinical hallmark of DOA that aids in its diagnosis is temporal optic nerve head pallor, which can be identified by fundus imaging[41]. Other clinical symptoms patients may exhibit include reduced visual acuity, color vision deficits, and desensitization of the central visual field[39,42-45]. Studies have also demonstrated that DOA patients tend to have smaller optic nerves, suggesting that they may be born with fewer RGCs[46,47].

The majority of DOA cases (~60-80%) are caused by mutations in the gene *optic atrophy 1* (*OPA1*; OMIM:*605290), a nuclear gene that encodes a dynamin-related GTPase located within the mitochondria[17,18,39,48,49]. To date, over 500 distinct, pathogenic *OPA1* mutations have been reported (http://www.LOVD.nl/OPA1)[50]. Mutations are found throughout the ~100 kilobase (kb) gene—primarily in exons, but also in introns, UTRs, and splice site regions. The majority of patients' mutations occur in either the GTPase domain or central dynamin region of *OPA1* (see section 1.4), specifically in exons 9, 14, 17, and 20[51]. Pathogenicity is dominant and can occur via dominant negative or haploinsufficiency mechanisms, depending on the type and location of the *OPA1* mutation[48]. Although autosomal dominant, the penetrance of *OPA1* mutations is ~43-88%[45,49]. Patients range in disease presentation, even within the same family, from asymptomatic to legally blind[39,52,53]. This suggests that individuals' unique genetic backgrounds and/or exposure to environmental factors may affect how severely they present with DOA symptoms.

Interestingly, although *OPA1* is expressed ubiquitously, the majority of DOA patients only exhibit ocular symptoms related to RGC degeneration. Around 20% of patients, however, present with extraocular symptoms, and are diagnosed with DOA+ (OMIM #125250, 165500). These symptoms include sensorineural hearing loss, chronic progressive external ophthalmoplegia, ataxia, myopathy, and peripheral neuropathy[52,54-57]. In extremely rare cases, individuals harbor biallelic (usually compound heterozygous) *OPA1* mutations and are usually classified as having Behr syndrome (OMIM #210000)[58]. These individuals present with severe neurological disease symptoms that include advanced, early-onset, optic atrophy, ataxia, peripheral neuropathy,

pyramidal signs, dysarthria, intellectual disability, and metabolic stroke[59-64]. In these cases, since some level of functioning is retained, at least one *OPA1* variant is predicted to be hypomorphic[50].

Apart from *OPA1*, other genes that have been associated with DOA include *OPA3, AFG3L2, SPG7, DNM1L, WFS1, SSBP1,* and *ACO2*[65,66]. Like *OPA1*, all are nuclear genes that encode proteins that have mitochondrial-associated functions. However, mutations in these genes are mostly associated with syndromic disease whereas most mutations in *OPA1* cause isolated optic atrophy, or non-syndromic disease[65].

1.3.2 DOA: Therapeutic approaches

Unfortunately, no approved therapies are currently available for DOA patients. Idebenone [2,3-dimethoxy-5-methyl-6-(10-hydroxydecyl)-1,4-benzoquinone], a short-chain quinone often described as a synthetic analog of coenzyme-Q10, is currently approved for LHON by the European Medicine Agency, and is often prescribed off-label to DOA patients. Response to idebenone varies, but an early start to therapy was predictive of more favorable responses to the treatment[67,68]. Visual improvements are attributed to idebenone's antioxidant properties and/or ability to stimulate respiratory chain activity[69]. *OPA1* mutations have been associated with increased reactive oxygen species (ROS) generation in multiple cell types, and antioxidant therapy has been suggested as an approach to decrease oxidative stress that likely contributes to *OPA1* mutation-driven pathogenesis[70-73]. In mitochondrial diseases such as LHON, idebenone is able to circumvent a non-functional complex I to restore ATP production by transferring electrons to complex III of the electron transport chain[74]. This mechanism of action may also benefit DOA patients given ATP synthesis driven by complex I substrates was significantly decreased in *OPA1* mutant fibroblasts compared to wild-type (WT) controls[75]. Notwithstanding, further studies are required to determine whether idebenone provides a reliably significant therapeutic benefit to DOA patients and to understand why some patients respond favorably to

the treatment while others do not. Also, apart from its questionable efficacy and failure to improve symptoms in all DOA patients, idebenone is not an ideal therapeutic option for DOA patients given its poor bioavailability (which requires repeat dosing three times daily) and lengthy time-to-effect period (it takes at least six months to show an improvement in symptoms)[67,76,77]. *In vitro* DOA disease models will hopefully come to serve as valuable tools that can be used to screen for therapeutic agents that mitigate downstream negative effects caused by *OPA1* dysfunction. Animal models will then be essential to evaluate system-wide pharmacodynamic and pharmacokinetic properties of the therapeutic agent, especially given how prevalent and essential mitochondria are to most human cells.

More permanent solutions to treat and to even cure DOA are currently being pursued preclinically. These primarily consist of cell and gene therapy approaches. Cell therapy approaches involve transplanting healthy RGCs into diseased retinas, promoting differentiation of existing cells in the retina into RGCs, and delivering cells that secrete neurotrophic or neuroprotective factors into diseased retinas to reduce the degeneration of existing RGCs[78-80]. Concerns to consider regarding cell therapy approaches include whether transplanted donor cells will face immunorejection, whether transplanted cells or cells that were newly differentiated *in vivo* can functionally integrate within the existing retinal framework and form appropriate synaptic connections, and whether the number of cells that are transplanted or differentiated *in vivo* is sufficient to provide therapeutic benefit. As DOA patients' cells all contain *OPA1* mutations, patients would best benefit from receiving donor cells that lack *OPA1* mutations or from receiving neuroprotective factors before experiencing significant RGC loss.

Lastly, much attention has revolved around gene therapy approaches to treat DOA. Unfortunately, given the heterogeneity of mutations present in the DOA patient population, one therapeutic approach cannot be used to treat all patients. However, approximately 50% of patient mutations are estimated to result in haploinsufficiency[53]. Therefore, a single therapeutic product that delivers a functional *OPA1* transgene to supplement the OPA1 expression from a patient's

WT allele could hypothetically treat approximately half of the patient population. In designing such a gene therapy, it is important to understand which *OPA1* mRNA and protein isoforms both WT and *OPA1* mutant RGCs express, and at which levels. As discussed in sections 1.4.1-1.4.3, *OPA1* undergoes complex transcriptional and post-translational processing that results in the generation of long (L-OPA1) and short (S-OPA1) protein isoforms. Tissues often express unique *OPA1* isoform signatures, and the ratio of long and short protein isoforms present in a cell determines how its mitochondria function[48,81,82]. Therefore, to successfully treat a patient's DOA, the supplemental transgene must sufficiently elevate the total level of *OPA1* expression as well as recapitulate or restore the specific ratio of long to short OPA1 protein isoforms present in healthy individuals' RGCs.

Maloney *et al.* found *OPA1* mRNA isoforms 1 and 7 to be most highly expressed in *OPA1* WT human retinal samples, and demonstrated that AAV2-mediated delivery of either isoform improved optokinetic response compared to untreated controls in a rotenone-induced mouse model of ocular complex 1 deficiency. However, neither the isoform 1 or isoform 7 transgene protected against RGC degeneration in the same mouse model[83]. Conversely, AAV2-mediated delivery of isoform 1 in a mouse model of DOA did not rescue visual function eight months post-injection, but did demonstrate a statistically significant protection of RGCs against degeneration compared to untreated control mice[84].

Although *OPA1* gene supplementation therapy holds promise, current approaches have shown limited efficacy and have been criticized for two main reasons. First, current vectors do not allow for fine-tuning of *OPA1* expression levels. This is concerning as *OPA1* overexpression can lead to aberrant changes in mitochondrial morphology[83,85,86]. Additionally, maintaining specific expression levels of the eight different *OPA1* mRNA isoforms and a specific ratio of long to short OPA1 protein isoforms is highly important to ensure proper mitochondrial functioning, and delivering a single *OPA1* isoform may not be adequate to complement the *OPA1* expression mediated by the WT allele. Determining which mRNA and protein isoforms are expressed in both

WT and *OPA1* mutant RGCs will undoubtedly advance therapeutic development on this front. To combat these concerns, other gene therapy approaches have been suggested that would maintain the *OPA1* gene's native machinery and thus theoretically preserve the appropriate expression levels of *OPA1* transcripts and proteins. These include using the endogenous *OPA1* promoter in vectors delivering an *OPA1* transgene or using CRISPR activation to upregulate the expression of *OPA1* from the WT allele[65,83]. However, the *OPA1* promoter is poorly defined, and off-target effects remain a concern for CRISPR-activation approaches[83].

As for the remainder of patients whose DOA is caused by dominant negative missense mutations, personalized gene editing therapies hold the most promise. Therapeutic approaches using CRISPR-Cas, prime, or base editing can be designed to correct patients' unique *OPA1* mutations, for in these instances, *OPA1* mutant proteins must be abolished for patients to regain normal functioning. Unfortunately, gene editing therapies are not 100% efficient when correcting mutations *in vivo*, and the generation of unwanted gene products due to inaccurate on-target gene editing and the risk of side effects generated by off-target binding events currently limit the practical implementation and translational feasibility of these gene editing approaches.

Moving forward, utilizing a variety of models to evaluate *OPA1*-mediated pathology and to assess whether therapeutic efforts can reverse or prevent disease symptoms is recommended. Human PSC-derived RGC models of DOA will be useful tools to both screen for and test therapeutic candidates that could treat DOA. As *OPA1* mutations cause RGCs to preferentially degenerate, findings using other human cell types such as fibroblasts cannot be assumed to be relevant to RGCs. However, human RO and RGC models currently lack features like a developed optic nerve and certain mature synaptic targets. Therefore, although rodents contain fewer *OPA1* isoforms than humans do, mouse models of DOA will continue to be useful to assess the safety and efficacy of experimental therapies[87-90]. Validating that experimental therapies show reproducible improvements in DOA disease symptoms across multiple disease models will ideally improve the therapy's odds of demonstrating clinical success in human patients.

1.4 *Optic atrophy 1* (*OPA1*)

1.4.1 *OPA1*: A genetic, transcriptional, and translational overview

The main gene responsible for DOA, *optic atrophy 1* (*OPA1*; OMIM:*605290), was mapped to chromosome 3q29 and definitively linked to the disease in the year 2000 by two independent groups[17,18]. *OPA1* is around ~104 kb long [National Center for Biotechnology Information (NCBI) Reference Sequence: NG_011605.1] and contains 31 exons (1-29, along with exons 4b and 5b). Exons 4, 4b, and 5b are alternatively spliced, generating eight different mRNA isoforms[48]. These isoforms encode proteins that are between 924 and 1,015 amino acids long. Interestingly, the beginning of exon 1 and all of exon 29 are untranslated[48].

Although it is a nuclear gene, *OPA1* encodes a dynamin-related GTPase that localizes within the mitochondria[17,18,39,48,49]. As such, *OPA1* was determined to contain a mitochondrial targeting sequence (MTS) [also called the mitochondrial import sequence (MIS)] within the first 90 amino acids of its basic N-terminal region[91,92]. Upon the preprotein's import into the mitochondria, a mitochondrial processing peptidase (MPP) cleaves the preprotein around the asparagine 87/phenylalanine 88 amino acid sites, effectively removing the MTS[92]. This gives rise to "long isoforms" of OPA1 protein (L-OPA1) that anchor to the inner mitochondrial membrane (IMM) via a transmembrane (TM) domain that is estimated to encompass the last 19 amino acids of exon 2[85,91]. OPA1 also exists as short protein isoforms (S-OPA1), which are generated via cleavage at one or more downstream sites—S1, S2, and S3, which are located within exons 5, 5b, and 4b, respectively[93]. These short isoforms are peripherally attached to the IMM or diffuse in the intermembrane space (IMS)[94,95]. L-OPA1 and S-OPA1 have been shown to have discrete roles, and the ratio at which they are present in a cell affects the cell's mitochondrial morphology and functioning[96]. Therefore, the ability of a cell to dynamically regulate *OPA1* transcriptional and proteolytic processing is essential for its survival and optimal functioning in both normal and stressed states.

1.4.2 *OPA1* transcript expression

Given its mitochondrial localization, *OPA1* is ubiquitously expressed. However, different tissues express different proportions of the eight mRNA isoforms[17,48]. Because *OPA1* mRNA isoforms are differentially cleaved into long and short protein isoforms that have been shown to have discrete mitochondrial functions, researchers have questioned whether the propensity of RGCs to degenerate in the context of DOA results from their expression of a unique combination of *OPA1* mRNA and/or protein isoforms[97].

There is currently more evidence against this claim, but which mRNA isoforms are expressed in human RGCs, and to which degree, has not been determined. In rodents, *Opa1* only has four mRNA isoforms (corresponding to human isoforms 1, 5, 7, and 8), as exon 4 is not differentially spliced[90,93]. WT and *Opa1* heterozygous mutant mouse retinas express isoforms 1, 7, and 8, with isoform 1 predominating[89]. The same has been shown in rat retina, RGCs, and brain[98]. Healthy human retina has also been shown to express isoforms 1 and 7, in addition to isoform 4. However, isoforms 1 and 4 only differ by three base pairs in length, and are thus difficult to distinguish on an agarose gel. Human fetal brain also strongly expressed isoforms 1 and 4, but conversely to human retina, expressed very low levels of isoform 7[48]. Interestingly, non-fetal human brain tissue most strongly expressed *OPA1* mRNA isoforms 5, 3, and 1, and very weakly expressed isoforms containing exon 5b (isoforms 4, 6, 7, and 8)[97]. In conclusion, it appears that human, mouse, and rat neural tissues commonly express *OPA1* mRNA isoform 1. However, where mouse and rat retinal and brain tissues share an identical *OPA1* mRNA expression signature, human retinal and brain tissues do not[48,89,90,97,98]. Therefore, although rodent data suggests that RGCs do not possess a unique *Opa1* mRNA isoform signature, it is incorrect to assume human RGCs will follow this pattern. Other, non-neural tissues corroborate this finding. For example, mouse heart, kidney, and liver *Opa1* mRNA isoforms signatures are identical, but human heart, kidney, and liver differ in both the abundance and presence of *OPA1* isoforms[48,90].

1.4.3 OPA1 proteolytic processing and expression

As mentioned briefly in section 1.4.1, after OPA1 preproteins are translated from mRNA isoforms in the cytoplasm, they enter the mitochondria via a MTS, which is then cleaved to generate L-OPA1 protein isoforms. S-OPA1 isoforms are subsequently generated when the S1 cleavage site is cleaved by the IM-associated metalloprotease, OMA1, and/or when the S2 and S3 cleavage sites are cleaved by the i-AAA protease, Yme1L. Adding to the complexity, Yme1L is constitutively active, whereas OMA1 activity is induced by intracellular conditions such as a decrease in mitochondrial membrane potential (MMP)[93,94,99,100]. All OPA1 isoforms contain the S1 site (as it falls within exon 5, which is not alternatively spliced). Additionally, isoforms 4 and 7 contain cleavage site S2 in exon 5b, and isoforms 3 and 5 contain cleavage site S3 in exon 4b. Isoforms 6 and 8 contain all three cleavage sites. Consequentially, *OPA1* mRNA isoforms 1 and 2 yield a single long and short protein isoform, isoforms 4 and 7 yield one long form and two short forms, and isoforms 3, 5, 6, and 8 (which all contain exon 4b) are fully processed to short forms[94].

The redundancy of protein products produced by multiple *OPA1* mRNA isoforms suggests that they have overlapping roles and that certain isoforms are able to compensate for the lack of others. Since L-OPA1 and S-OPA1 isoforms have been shown to have specific roles necessary for mitochondrial functioning, it is important to characterize their abundance in WT, as well as in *OPA1* mutant, RGCs[82,94,96]. OPA1 protein isoforms run as six bands between 80-100 kDa on a polyacrylamide gel, named a-d, d', and e. Bands a and b correspond to L-OPA1 isoforms and bands c-e correspond to S-OPA1 isoforms[90,93]. Various studies have reported varying results regarding which OPA1 protein isoforms are expressed in human, mouse, and rat retinal tissues[81,89,98,101,102]. For example, Aijaz *et al.* reported that human retinal tissue expressed a single ~90 kDa OPA1 isoform, which most likely represents band b[81]. Others similarly found that mouse and rat retinal tissue only expressed a ~90 kDa isoform[89,102]. Wang *et al.* also demonstrated that human retinal tissue expressed a single protein isoform, although the isoform was ~97 kDa. In

further disagreement with the previously mentioned studies, Wang *et al.*, in addition to other groups, found mouse and rat retinal tissues to express multiple OPA1 protein isoforms, as opposed to a single isoform[90,98,101]. However, the pattern of isoforms exhibited by the tissues differed across these studies[90,98,101].

The only report of OPA1 protein expression in RGCs demonstrates that the OPA1 protein isoforms expressed in RGCs do not differ from those expressed in "other retinal cell extracts." Both RGC and "other retinal cell" lysate from rats displayed four OPA1 protein bands—two bands around 90 kDa and two bands around 86 kDa[98]. The expression of OPA1 protein isoforms in human RGCs has not been reported, likely due to the scarcity of human RGCs available from donor eyes or difficulty purifying a large enough number of human PSC-derived RGCs. Further studies regarding the requirement for and relationship between OPA1 isoforms in different cell types will help elucidate why RGCs may be particularly prone to degenerate in the context of *OPA1* mutations.

Regarding the expression of OPA1 isoforms in WT vs *OPA1* mutant cells and tissues, there does not appear to be a difference in which protein isoforms are expressed. However, mouse and human cells with nonsense mutations did show a reduction in the total amount of OPA1 protein expressed, in alignment with the heterozygous mutations' proposed pathogenic mechanism of haploinsufficiency[19,89]. Ultimately, although findings suggest that *OPA1* mutant cells do not contain a unique protein isoform signature that could explain their pathology over WT cells, this information has not been verified by comparing healthy and *OPA1* mutant, human RGCs. If WT and *OPA1* mutant RGCs express the same OPA1 protein isoforms, and do so at the same ratio, a reduction in the amount of OPA1 protein produced (in the case of mutations leading to early stop codons) or problems with oligomerization (in the case of dominant negative mutations) are likely responsible for DOA patients' symptoms.

1.4.4 OPA1's functional roles in the mitochondria

Downstream of exon 5b, all OPA1 protein isoforms contain the same protein domains[90]. As mentioned, *OPA1* encodes a dynamin-related GTPase, which belongs to a class of proteins known to remodel biological membranes using GTPase activity. Therefore, like other dynamin family GTPases, *OPA1* encodes a GTPase domain (exons 8-15), central dynamin region (also called the middle domain) (exons 16-24), and a GTPase effector domain (GED) (exons 27-28)[48,103,104]. The GTPase domain binds and hydrolyzes GTP and is responsible for *OPA1*'s role in facilitating IMM fusion[105]. The central dynamin region has been shown to be involved in OPA1 oligomerization, and the GED helps to regulate the activity of the GTPase domain[106].

OPA1's GTPase-mediated fusogenic role and ability to oligomerize with itself and other proteins explain the protein's ability to perform a variety of inter- and intra-mitochondrial functions. In fact, OPA1 has been appropriately referred to as the "swiss army-knife" of mitochondria, as it mediates fusion, cristae remodeling, mtDNA maintenance, respiratory chain efficiency, and the sequestration and release of cytochrome *c*[65]. Often, these processes are tightly linked. The work in this dissertation however mainly examines the effects of *OPA1* mutations on mitochondrial fusion, cristae integrity, and bioenergetic function.

1.4.4.1 Fusion

The process of "mitochondrial dynamics" refers to a cell's ability to maintain an equilibrium between mitochondrial fission and fusion, and is essential for cellular health[107]. Mitochondrial fission can separate damaged mitochondria to be removed via mitophagy, and fusion can increase the energetic supply of the cell[12]. The processes of fission and fusion are reflected in the morphology of the mitochondria. Fission results in fragmental mitochondria, whereas fusion leads to filamentous, or elongated, mitochondria[108]. An excess or deficiency in either fission or fusion is deleterious to the cell[12,20,94].

OPA1 promotes mitochondrial fusion together with the mitofusin proteins, MFN1 and MFN2. Like OPA1, MFN1 and MFN2 are dynamin-related GTPases, and facilitate outer mitochondrial membrane (OMM) fusion, which must occur prior to inner mitochondrial membrane (IMM) fusion[109,110]. OPA1 and a lipid in the IMM called cardiolipin work in concert to promote IMM fusion. The IMMs of two mitochondria are able to fuse when cardiolipin on one IMM interacts with L-OPA1 on an opposing IMM. Interestingly, L-OPA1:L-OPA1 interactions across independent IMMs are not sufficient for fusion to occur, but L-OPA1 isoforms can sustain IMM fusion in cells lacking S-OPA1 as long as cardiolipin is present[111]. S-OPA1 isoforms cannot independently sustain fusion activity, but increase the efficiency of L-OPA1 isoform-dependent fusion activity[111-113].

Studies have shown that cells containing *OPA1* mutations or reduced levels of OPA1 protein have a fragmented mitochondrial network[18,20,98]. Increased fission could explain the RGC degeneration observed in DOA patients, as fused vs smaller, fragmental mitochondria are more resistant to stress and have higher concentrations of ATP[114,115]. Additionally, larger mitochondrial complexes are more likely to sustain energy under stressful conditions, as smaller mitochondrial fragments are preferentially degraded by autophagy[116].

1.4.4.2 Cristae structure and integrity

OPA1 also plays an essential role in maintaining cristae structure and integrity[85], a process demonstrated to be regulated independently from fusion[117]. Oligomerization of regulated amounts of soluble S-OPA1 and IMM-bound L-OPA1 keep cristae junctions tight, but L-OPA1 or S-OPA1 protein isoforms can individually maintain cristae structure if necessary[112,113]. Conversely, *in vitro* studies have shown that the lack of *OPA1* or the presence of *OPA1* pathogenic mutations leads to a dramatic disorganization of mitochondrial ultrastructure in human cell lines and in DOA patient fibroblasts[20,75,85]. As function is often tightly linked to form, it is no surprise that mitochondrial functions begin to deteriorate when the cristae lose their structure and integrity. Under normal

conditions, cristae stabilize the respiratory chain complexes, also located in the IMM, which allows proper bioenergetic functioning. Intact cristae also maintain the mitochondrial membrane potential (MMP) generated by the electron transport chain and prevent cytochrome *c* release-induced apoptosis[20,117,118]. Cytochrome *c* is normally sequestered between cristae junctions, but if cristae integrity is compromised and MMP drops, cytochrome *c* will escape into the cytosol and activate downstream caspases that result in apoptosis[20,73,119]. Such apoptotic signaling events followed by eventual cell death could explain the RGC degeneration observed in DOA patients[120].

1.4.4.3 Bioenergetics

RGCs have one of the highest energy demands in the central nervous system (CNS) as they need to transmit visual signals large distances from the retina to targets in the brain. To meet this high energy requirement, RGCs rely heavily on oxidative phosphorylation[121,122]. OPA1 has been shown to stabilize members of the super respiratory complex—also located in the IMM—by maintaining cristae shape, which in turn regulates oxidative phosphorylation activity[118]. Additionally, co-precipitation experiments demonstrated that OPA1 interacts with subunits in respiratory complexes I, II, III, IV, and V (ATP synthase)[75,123]. Interestingly, IMM-bound L-OPA1 isoforms and soluble S-OPA1 isoforms can both independently preserve bioenergetic function[82,113].

OPA1 mutations have been associated with decreases in mitochondrial ATP synthesis, oxygen consumption rate (OCR), and the bioenergetic efficiency of the respiratory complexes[19,21,75,113,118]. Specifically, human lymphoblasts from DOA patients with poor vision showed a decrease in complex I and complex II-driven ATP synthesis rates compared to *OPA1* WT controls and had lower endogenous respiration than DOA patients with normal vision[19]. Interestingly, *OPA1* haploinsufficient fibroblasts also had impaired complex I-driven ATP synthesis rates compared to WT fibroblasts, but did not demonstrate differences in growth or substantially lower ATP levels in either glucose or galactose media. Another study demonstrated

that fibroblasts from DOA and DOA+ patients had a mild complex IV defect, but not a significant enough one to alter the cells' *in vitro* respiration rate[75].

However, again, information gleaned from studying how other cell types behave in an *in vitro* environment may not necessarily be relevant in understanding the mechanisms responsible for the RGC-specific degeneration observed in DOA patients. Findings from cells of a similar origin however, are likely to be more applicable. For instance, neural progenitor cells (NPCs) with heterozygous *OPA1* mutations derived from the iPSCs of Parkinson's patients demonstrated much more significant and obvious decreases in OCR, total mitochondrial ATP, and complex I-driven ATP compared to WT NPCs than were observed between *OPA1* mutant and WT fibroblasts and lymphoblasts[124].

Separately, it is of interest to note that OPA1 interacts with ATP synthase to curb reactive oxygen species (ROS) production. As such, *OPA1* mutations have been associated with increased ROS generation in multiple cell types[71-73,125]. Whether human *OPA1* mutant RGCs have increased levels of ROS is a relevant area for future investigation, and would support the use of antioxidants as potential therapeutic agents.

In conclusion, OPA1's mitochondrial roles are often interdependent upon one another, and experiments need to be elegantly designed to determine cause from effect. For example, a decrease in *OPA1* can disrupt cristae morphology, which can lead to a drop in mitochondrial membrane potential. This will release cytochrome *c* into the cytosol, signaling apoptosis. Decreased membrane potential is also shown to increase proteolytic processing into short protein isoforms via OMA1, and an increase of short forms leads to higher mitochondrial fragmentation. If fragmentation is increased over fusion in *OPA1* mutant cells, the cell may be more likely to apoptose than to remove a high amount of damaged mitochondria via mitophagy. Therefore, before testable hypotheses can be made regarding the molecular mechanisms behind human RGC degeneration, it will be useful to establish baseline information such as

which *OPA1* mRNA and protein isoforms are expressed in the RGCs of healthy individuals and which are expressed in the RGCs of DOA patients with *OPA1* mutations.

1.5 Human DOA disease modeling

Although many studies have linked *OPA1* mutations to defects in mitochondrial morphology and functioning, how these defects are caused and how they lead to RGC degeneration in DOA patients remains unclear. The tissue specificity of DOA to the RGCs is somewhat surprising given OPA1 is a ubiquitously expressed mitochondrial protein, but underscores the need for human RGC models of DOA. These models can be generated by first establishing *OPA1* mutant human pluripotent stem cell (hPSC) lines, which can then be differentiated into RGCs *in vitro*[126-128].

Importantly, given the molecular and clinical heterogeneity of the DOA patient population, no one *OPA1* mutation will be able to recapitulate the full spectrum of disease. Mutations are found throughout the entire *OPA1* gene, and depending on the type of mutation, can cause haploinsufficiency or dominant negative-mediated disease[48]. Furthermore, the degree to which patients experience clinical symptoms varies widely, even across family members that have the same *OPA1* mutation[52,129]. Multiple studies have attempted to draw genotype-phenotype correlations or to infer novel *OPA1* variants' pathogenicity based on their genomic location or other defining characteristics (protein domain affected, type of mutation), but overarching conclusions have remained largely elusive [39,64,130,131]. The only widely accepted correlation is that individuals with missense mutations in the GTPase domain are associated with a greater risk of developing DOA+[54].

It may be particularly useful to initially generate DOA models from *OPA1* mutant iPSCs that have been reprogrammed from DOA or DOA+ patients, as the *in vitro* phenotypes can be compared to the patient's actual clinical presentation of disease to initially assess and establish the validity of the model. Having a full understanding of patients' genotypic and phenotypic

information allows other questions to be investigated including those pertaining to penetrance. For instance, iPSCs from two patients containing the same *OPA1* mutation but exhibiting different degrees of vision loss could be used to identify other internal/genetic or environmental factors that may influence phenotypic severity.

1.5.1 Previously established *OPA1* heterozygous mutant PSC lines

At the time of this publication, to my knowledge, there have been 12 *OPA1* heterozygous mutant human PSC lines generated. All lines were generated by reprogramming either peripheral blood mononuclear cells (PBMCs) or fibroblasts from DOA or DOA+ patients into iPSCs, except one in which WT fibroblasts were simultaneously reprogrammed and edited using CRISPR-Cas9 to generate an early stop codon in one allele of exon 2 in attempts to model haploinsufficiency[132]. However, two iPSC lines that produce an even shorter protein product (11 amino acids) than the aforementioned haploinsufficient line had already been previously generated from two related individuals containing a NM_130837.3:c.33ins9 mutation. These two lines are additionally interesting as the patients they were derived from had differing phenotypes despite harboring the same *OPA1* mutation. One line is derived from a woman who had DOA and the second is derived from her son who had both DOA and Parkinson's disease[129].

Of the 12 *OPA1* heterozygous mutant iPSC lines, three harbor missense mutations in exons 8, 13, and 14 of the GTPase domain: NM_015560.2:c.805T>C; p.Ser269Pro, NM_130837.3:c.1468T>C; p.Cys490Arg, and NM_015560.2:c.1334G>A; p.Arg445His, respectively. In line with findings that DOA+ patients more commonly have missense mutations in the GTPase domain, these lines are all derived from DOA+ patients and the mutations are expected to have a dominant negative effect[133-135].

Two lines, IISHDOi003-A and Oex2054SV.4 have mutations in the central dynamin region (exons 16-24). Although both are generated from DOA+ patients, one patient's mutation in exon 17 (NM_015560.2:c.1635C>A; p.Ser545Arg) is thought to have a dominant negative effect while

the other's mutation in exon 20 (NM_015560.2:c.1861C>T; p.Gln621Ter) is predicted to cause haploinsufficiency[136,137]. Huang *et al.* also report generating iPSC lines from two separate individuals with DOA containing a mutation in intron 24 (NM_015560.2:c.2496 + 1 G>T) that is predicted to affect the splicing of *OPA1* transcripts[138]. Lastly, two groups independently generated iPSC lines from separate individuals with DOA that both had one of the most frequently occurring *OPA1* mutations, NM_015560.2:c.2708_2711delTTAG[132,139]. This mutation has been shown to cause haploinsufficiency, and occurs in exon 27, which is part of the general effector domain (GED)[140].

1.5.2 Generating retinal ganglion cells from human PSCs

Once generated, human PSC lines containing *OPA1* mutation(s) can be differentiated into RGCs and used to establish *in vitro*, DOA disease models. Thanks to recent advances in stem cell biology and gene editing technology, *OPA1* mutant hPSCs can be more easily and readily generated than ever before, and hPSC-derived RGC differentiation protocols continue to diversify and improve. Notably, the differentiation procedures used to generate RGCs from hPSCs take either a predominately 2D or a 3D approach. 2D RGC differentiation protocols involve minimal, if any, manipulation of monolayer PSC cultures, and consist primarily of exposing developing cells to neural induction medium supplemented with a range of chemicals that induce RGC development[141,142]. 3D RGC approaches also utilize neural induction medium and various neural factors to drive PSCs towards a neural fate, but more closely mimic *in vivo* retinal development as PSCs self-organize into 3D retinal organoids (ROs) that resemble optic vesicles (OVs) and optic cups[143-145]. RGCs do not take significantly longer to develop using either 2D or 3D differentiation approaches[146], and because RGCs are the first neuronal cell type to develop in the retina, they are easier to obtain than other retinal neurons[15].

Choosing which hPSC-derived RGC differentiation protocol to use should be dependent on the purpose of one's assay or experiment. For instance, RGCs generated using 2D

differentiation protocols lack the same spatial organization found in the human retina, and may consequently have more significantly altered cellular input signals than RGCs grown in ROs (which maintain a RGC layer similar to the *in vivo* human retina's RGC layer[147,148]). Furthermore, 3D RGC generation protocols more closely mimic *in vivo* stages of retinal development. Therefore, if one's purpose is to investigate human disease mechanisms that affect RGCs, using a 3D protocol would generate RGCs more likely to behave similarly to RGCs *in vivo*. Similarly, if one was interested in RGCs relative to other retinal cell types, using a 3D organoid system is ideal (i.e., the percentage of RGCs could be assessed relative to other cell types). However, certain experimental assays (bioenergetics, axon projection, etc.) may be better suited to evaluating a purified population of RGCs in a monolayer, in which case generating an initially enriched 2D RGC culture would be advantageous and convenient.

Although current PSC-derived RGCs have some noticeable differences from RGCs *in vivo*— they lack an organized optic nerve and synaptic brain targets, they do not receive the same input signals as they do *in vivo*, and they begin to die in culture before other retinal neurons can fully mature (presumably due to a lack of nutrition and/or poor passive diffusion in the inner areas of the RO)[149,150]— they are the closest we can currently get to studying live, human RGCs. Much work remains to validate hPSC-derived disease models, but it is my hope that they will routinely be used in the future to complement animal disease models. In this way, maximal amounts of information could be obtained regarding molecular mechanisms underlying disease pathogenesis, and therapies could be further validated for safety and efficacy before entering human trials.

CHAPTER 2

Establishing induced pluripotent stem cell lines from two dominant optic atrophy patients with distinct *OPA1* mutations and clinical pathologies

Katherine A. Pohl[1,2], Xiangmei Zhang[1], Anh H. Pham[1,3], Jane W. Chan[1,3], Alfredo A. Sadun[1,3]*, Xian-Jie Yang[1,2]*

[1]Stein Eye Institute, Department of Ophthalmology, University of California, Los Angeles, Los Angeles, CA, United States

[2]Molecular Biology Institute, University of California, Los Angeles, Los Angeles, CA, United States

[3]Doheny Eye Institute, Department of Ophthalmology, University of California, Los Angeles, Pasadena, CA, United States

* Co-senior authors

2.1 Abstract

Dominant optic atrophy (DOA) is an inherited disease that leads to the loss of retinal ganglion cells (RGCs), the projection neurons that relay visual information from the retina to the brain through the optic nerve. The majority of DOA cases can be attributed to mutations in *optic atrophy 1* (*OPA1*), a nuclear gene that encodes a mitochondrial-targeted protein that plays important roles in maintaining mitochondrial structure, dynamics, and bioenergetics. Although *OPA1* is ubiquitously expressed in all human tissues, RGCs appear to be the primary cell type affected by *OPA1* mutations. It is therefore essential to study DOA in human RGCs to understand

how an *OPA1* deficiency renders them particularly susceptible to degeneration. Primary human RGCs are extremely limited, but advances in stem cell biology have made it possible to generate human RGCs from pluripotent stem cells (PSCs). To aid in generating human PSC-derived RGC models of DOA, we generated iPSC lines from two DOA patients carrying distinct *OPA1* mutations. One patient presents with more severe DOA symptoms whereas the other patient's symptoms are mild. These iPSC lines can be used to study DOA disease mechanisms *in vitro*, and findings can be compared with DOA patients' clinical presentations of disease to generate novel insights regarding *OPA1*-mediated RGC degeneration.

2.2 Introduction

Dominant optic atrophy (DOA; OMIM #165500) is the most prevalent inherited optic neuropathy, affecting an estimated 1:10,000 to 1:50,000 individuals worldwide[35,37-39]. DOA is characterized by the preferential degeneration of retinal ganglion cells (RGCs), whose axons make up the optic nerve. RGC loss causes progressive bilateral vision loss that often begins in the first decade of life. A hallmark of DOA which aids in its diagnosis is wedge-shaped, temporal optic nerve head pallor[41]. Other clinical symptoms include reduced visual acuity, color vision deficits, and central visual field defects[39,42-45]. DOA patients also tend to have smaller optic nerves, suggesting that they may be born with fewer RGCs[46,47].

The majority of DOA cases, ~60-80%, are caused by mutations in the gene *optic atrophy 1* (*OPA1*; OMIM:*605290), a nuclear gene that encodes a dynamin-related GTPase located within the mitochondria[17,18,45,104]. OPA1 protein plays important roles in mitochondrial fusion, cristae remodeling, and bioenergetic output[75,85,113,118,151-157]. To date, over 500 different pathogenic mutations throughout the ~100 kilobase (kb) *OPA1* gene have been documented (http://www.LOVD.nl/OPA1)[158]. Although autosomal dominant, *OPA1* mutations are ~43-88% penetrant[45,49]. Patients range in their disease presentation, even within families harboring the same mutation, from asymptomatic to legally blind[39,52,53]. A subset of patients develops

extraocular features including sensorineural hearing loss, ataxia, myopathy, and peripheral neuropathy. These patients are classified as having DOA+ (OMIM #125250, 165500), a diagnosis that has been correlated with missense mutations in the GTPase domain of OPA1[52,54-57]. In extremely rare cases, individuals have been found to harbor biallelic (usually compound heterozygous) *OPA1* mutations[58]. These individuals are usually classified as having Behr syndrome (OMIM #210000,) a severe neurological disease with symptoms that include advanced early-onset optic atrophy, ataxia, peripheral neuropathy, pyramidal signs, dysarthria, intellectual disability, and metabolic stroke[59-64].

Interestingly, although *OPA1* is expressed ubiquitously, the majority of DOA patients only exhibit RGC degeneration and by extension, signs and symptoms related to optic neuropathy. Due to the limited availability of human retinal tissues, non-human cells or human cell types other than RGCs have been used to study *OPA1* in relation to DOA[19,21,23-32,75,94,152,159]. Recent advances in stem cell technology have enabled the derivation of human retinal neurons from pluripotent stem cells (PSCs)[160-164], permitting *in vitro* DOA disease models to be established using patients' induced pluripotent stem cells (iPSCs). However, the heterogeneity of *OPA1* genotypes and phenotypes present in the DOA patient population, coupled with the incomplete penetrance of the disease, necessitates that a range of PSC lines containing distinct *OPA1* mutations be generated to properly model and understand *OPA1*-driven DOA. To help establish DOA models that recapitulate the spectrum of the disease, we generated iPSC lines from two DOA patients with heterozygous *OPA1* mutations that are distinct from those in previously reported iPSC lines[132,134-136,165-169]. Importantly, we also describe the clinical presentation of both DOA patients at the time of iPSC derivation, which is important information to consider when characterizing and validating disease models derived from these iPSC lines.

2.3 Results

2.3.1 Genetic and clinical presentation of DOA patients

Two DOA patients with previously determined, heterozygous *OPA1* mutations were recruited for the study. Both patients are male and of European ancestry. The first patient, referred to as “Patient 1,” presented with symptoms of DOA at age 7 and has a single G insertion in one allele of the *OPA1* gene in exon 19, which is part of the central dynamin region of the protein. This insertional mutation causes a frameshift that leads to an early stop codon, resulting in a predicted protein product of 652 amino acids as opposed to the 1,015 amino acids encoded by the full-length wild-type (WT) transcript (**Table 2-1**). The second patient, “Patient 2,” was relatively asymptomatic and found to have an *OPA1* mutation when his son with vision loss was diagnosed with DOA. Patient 2 has a heterozygous, two base pair AT deletion in exon 13, which encodes part of the GTPase domain of the OPA1 protein. This mutation also causes a frameshift and subsequent premature stop codon. The mutant transcript is predicted to encode a protein of 483 amino acids as opposed to the 1,015 amino acids encoded by the full-length WT transcript (**Table 2-1**).

At the time of enrollment and iPSC derivation, Patient 1 was 49 years old and Patient 2 was 60 years old. Neither patient was reported to have extraocular neurological disease or additional neural retina disorders. Additionally, both patients tested negative for bloodborne infectious diseases including hepatitis B, hepatitis C, HIV, and syphilis. The donor patients underwent a comprehensive ophthalmological examination in which visual acuity, tonometry, fundus imaging, Humphrey visual field (HVF) testing, and spectral-domain optical coherence tomography (SD-OCT) were performed.

Patient 1 displayed ophthalmologic symptoms of classical DOA. His visual acuity had declined to 20/100 -1 (OD) and 20/150 (OS) (**Table 2-1**), and fundus imaging showed typical, wedge-shaped retinal nerve fiber layer (RNFL) loss with temporal pallor (**Figure 2-1A**). HVF 30-2 testing revealed bilateral, cecocentral scotomas (**Figure 2-1B**). In addition, SD-OCT showed

RNFL thinning temporal to the optic disc, with some additional thinning in the inferior and nasal portions of the optic disc in the right eye (**Figure 2-2A**).

In contrast, Patient 2 has remained largely asymptomatic over his lifetime. Despite fundus images that showed temporal pallor of the optic nerve, visual acuity was 20/25 in both eyes (**Figure 2-1A, Table 2-1**). Visual field assessment detected a small paracentral scotoma (**Figure 2-1B**), which made it difficult for Patient 2 to focus on the central target during HVF 30-2 testing, resulting in high false positive and negative rates. The smaller field of HVF 10-2 testing allowed the patient to maintain central fixation on the target and detected the edge of the central scotomas, which are located superior temporally on HVF 10-2 (**Figure 2-1B**). SD-OCT revealed bilateral inferior RNFL thinning with more advanced superior and temporal thinning of the left eye (**Figure 2-2B**).

2.3.2 Generation of *OPA1* heterozygous mutant iPSCs from DOA patients

To generate iPSC lines from both DOA patients, peripheral blood mononuclear cells (PBMCs) were isolated from patients' blood samples and reprogrammed by episomally expressing the pluripotency factors OCT3/4, SOX2, KLF4, L-Myc, shp53, Lin28, and SV40LT[170,171]. Two independent iPSC lines (n1a and n1b) were established from each patient. Lines generated from Patient 1 and Patient 2 were named 1iDOAn1a/1iDOAn1b, and 2iDOAn1a/2iDOAn1b, respectively. Although all four iPSC lines were authenticated, data in this report depicts the n1a lines only.

Both 1iDOA and 2iDOA displayed typical pluripotent stem cell morphology and stained positive for alkaline phosphatase (AP) activity (**Figure 2-3A**). Immunocytochemistry was performed to further verify the expression of pluripotency markers by the iPSCs in comparison to an established human embryonic stem cell (ESC) line, UCLA1. All lines were shown to similarly co-express the PSC markers SOX2, OCT3/4, and NANOG (**Figure 2-3B**). Furthermore, 1iDOA and 2iDOA iPSCs displayed a normal male karyotype with 22-pair autosomes and XY

chromosomes (**Figure 2-3C**). The iPSC lines tested negative for mycoplasma and their unique genetic identities were confirmed using short tandem repeat (STR) analysis (not shown). To verify that the iPSC lines carried the DOA patients' specific *OPA1* mutations, genomic DNA was extracted from 1iDOA and 2iDOA iPSCs and used as a template to obtain PCR products spanning the expected mutation sites in exons 19 and 13, respectively. DNA sequencing analysis of the PCR products validated that each patient's existing heterozygous *OPA1* mutation was present in his iPSCs (**Figure 2-3D**).

2.3.3 Detection of ROS production in PSC lines

Since *OPA1* mutations may lead to elevated levels of cellular reactive oxygen species (ROS), we performed live cell imaging to label mitochondria and to detect ROS in the DOA patients' iPSC lines (1iDOA and 2iDOA) as well as in a control ESC line (H9). Mitochondria, (labeled with MitoTracker Red) were similarly distributed in all PSC lines (**Figure 2-4**). However, 2iDOA PSCs presented with higher levels of ROS compared to 1iDOA and H9 PSCs (**Figure 2-4A, C, and E**). All PSC lines displayed elevated levels of ROS when treated with the ROS-inducing agent menadione (**Figure 2-4B, D, and F**). Further detailed analysis will be necessary to determine the mechanism underlying the differential ROS production and whether *OPA1* mutations affect mitochondrial functioning in PSC-derived neurons.

2.4 Discussion

Although OPA1 function has been extensively studied, it remains an enigma why retinal projection neuron RGCs are particularly prone to degenerate when OPA1 functioning is compromised, given that OPA1 is a ubiquitously expressed mitochondrial protein. Historically, the scarcity of human RGCs has significantly limited researchers' ability to investigate this phenomenon. Over the last decade, human PSCs have emerged as replenishable sources that can be used to produce different somatic tissue and cell types. Since DOA has not been studied

in-depth using human RGCs, stem cell-based models provide unprecedented opportunities to investigate DOA disease mechanisms. However, given the molecular and clinical heterogeneity of the DOA patient population and incomplete penetrance of *OPA1* mutations, it is unlikely that an *in vitro* model from PSCs containing one specific *OPA1* mutation will be able to recapitulate the full spectrum of the disease. The iPSC lines from the two DOA patients reported here carry *OPA1* mutations distinct from those in previously reported iPSC lines[132,135,136,165-169], thus providing additional tools to study DOA using human PSC-based RGC models. Furthermore, the clinical records and DOA-associated ophthalmological symptoms for each DOA patient at the time of iPSC derivation will be useful information when comparing *in vitro* cellular level findings with clinical manifestations.

Despite the autosomal dominant inheritance pattern of DOA, the disease pathogenicity can occur via dominant negative or haploinsufficiency mechanisms, depending on the type and location of the *OPA1* mutations[48]. The two DOA patients examined in this study have heterozygous *OPA1* frameshift mutations that are predicted to produce truncated proteins. Ophthalmic examinations showed that Patient 1, whose mutation falls within the central dynamin region of OPA1 (p.Glu650GlyfsTer4), has more severe and extensive DOA symptoms. Previous studies have established iPSC lines from DOA+ patients with mutations in the central dynamin region[136,166], suggesting a correlation of this region with a more severe disease pathology. However, DOA+ has been most strongly correlated with missense mutations in the GTPase domain[52,54-57]; all iPSC lines previously generated with *OPA1* mutations in the GTPase domain have missense mutations[133-135]. Interestingly, although Patient 2's mutation (p.Ile473PhefsTer12) falls within the GTPase domain, he has remained largely asymptomatic. Given his mutation leads to an early stop codon, this suggests that OPA1 proteins with a partially truncated GTPase domain may act differently from OPA1 proteins with a mutated GTPase domain. To our knowledge, this also is the first report of an iPSC line generated from a DOA patient with an *OPA1* mutation that presents with mild symptoms. Separately, the initial characterization of 2iDOA iPSCs

demonstrated that they exhibited higher cellular ROS compared to 1iDOA iPSCs or WT H9 ESCs. This suggests that under *in vitro* culture conditions, effects of *OPA1* mutations may be more readily detected.

Ultimately, the availability of *OPA1* mutant iPSC lines can benefit the further characterization of *OPA1* mutant iPSC-derived RGCs, which can be used to elucidate the pathological mechanisms underlying DOA and to identify and test gene and molecular therapies. Additionally, increasing evidence indicates that mitochondrial dysfunction plays an important role in neurodegenerative and aging-related diseases[9,124]. Therefore, findings from *OPA1* mutant iPSC-derived disease models can likely provide important insights into other neurodegenerative diseases that share common metabolic deficiencies with DOA.

2.5 Methods

2.5.1 Patient enrollment and ophthalmic examinations

This research was conducted at the University of California, Los Angeles under the institutional review board (IRB) protocol #19-000879, and approved by the Office of the Human Research Protection Program (OHRPP). All participants signed informed consent and Health Insurance Portability and Accountability Act (HIPAA) research authorization forms to enroll in the study. Participants were outpatients of the Doheny Eye Clinics of UCLA. Detailed clinical data including family history, visual acuity, tonometry, fundus photography (Optos), Humphrey visual field (Zeiss), and optical coherence tomography (Patient 1, Heidelberg Engineering; Patient 2, Zeiss) was collected.

2.5.2 Generation of DOA patient iPSCs

Peripheral blood was collected from DOA patients the same day the ophthalmologic tests were performed. Peripheral blood mononuclear cells (PBMCs) were reprogrammed into iPSCs at the Cedars Sinai Medical Center iPSC core using a non-integration method as previously

described[170]. Two independent iPSC lines were established for each DOA patient. The iPSC lines were named as 1iDOAn1a and 1iDOAn1b for Patient 1, and 2iDOAn1a and 2iDOAn1b for Patient 2, respectively. The characterization included mycoplasma testing, alkaline phosphatase staining, G-band karyotyping, and short-tandem repeat (STR) cell line authentication. Lines are referred to as 1iDOA and 2iDOA throughout this manuscript, but experiments described primarily used n1a clones. 1iDOA carries the heterozygous *OPA1* mutation NC_000003.12:g.193648807dup and 2iDOA carries the heterozygous *OPA1* mutation NC_000003.12:g.193643567_193643568del.

2.5.3 Human PSC cell cultures

Human ESCs and iPSCs were maintained in mTeSR plus medium (Stemcell Technologies) supplemented with 1% Antibiotic Antimycotic (Gibco/ThermoFisher Scientific) on Matrigel (Corning) coated plates at 37°C with 5% CO_2. PSCs were passaged by dissociating monolayer cells into a single-cell suspension with Accutase (Stemcell Technologies). Single cells were plated in mTeSR plus supplemented with 1% Antibiotic Antimycotic and 10 μM of Y-27632 (Stemcell Technologies) for 24 hours, after which the medium was replaced with mTeSR plus with 1% Antibiotic Antimycotic. The medium was changed no less frequently than every other day.

2.5.4 Immunofluorescent staining and imaging

PSCs grown on Matrigel-coated NUNC™ Thermanox™ 13 mm plastic coverslips (ThermoFisher Scientific) were fixed in 4% paraformaldehyde in PBS for 2 minutes and then incubated in blocking solution (0.1% TritonX-100, 2% donkey serum, 10% FBS in DMEM). Coverslips were incubated with primary antibodies, followed by secondary antibodies and DAPI diluted in blocking solution (**Supplementary Table 2-1**). All incubations were for 1 hour at room temperature, and staining periods were followed by three, 5-minute washes in PBS with 0.1% Tween 20. Coverslips were mounted on glass slides (Fisher Scientific) with mounting media (Fluro-Gel, Electron Microscopy

Sciences) and imaged using the Olympus Flowview FV1000 (upright) scanning laser confocal microscope with Plan-APO objectives.

2.5.5 Sequencing of genomic PCR products

Prior to enrolling in the study, each DOA patient's specific *OPA1* mutation was classified/diagnosed via exon sequencing. To confirm the presence of these mutations in the DOA patients' iPSC lines, genomic DNA was isolated from iPSCs using the Purelink genomic DNA Mini Kit (Invitrogen). 200 ng of DNA was used a template in each PCR reaction using Hot Star Taq DNA Polymerase (Qiagen) and primers flanking the respective *OPA1* mutation site (**Supplementary Table 2-2**). Thermocycler conditions were as follows: 15 min at 95°C; 35 cycles of 30 seconds at 94°C, 30s at 59°C and 1 min at 72°C; and 10 min at 72°C. PCR products were Sanger sequenced using the primers listed in **Supplementary Table 2-2.**

2.5.6 Cellular ROS and mitochondrial imaging

PSCs grown as a monolayer were washed once with PBS and then incubated in mTeSR plus medium with or without 100 μM of menadione (Sigma) at 37°C for 1 hr. All cells were then incubated in mTeSR plus with 5 μM of CellROX Green Reagent (Invitrogen), 250 nM of MitoTracker Red CMXRos (Invitrogen), and 5 μg/mL of Hoechst 33342 (Invitrogen) at 37°C for 30 min (**Supplementary Table 2-1**). Cells were then washed once in PBS and immediately imaged in HBSS without phenol red using an Olympus IX81 scanning laser confocal microscope with Plan-APO objectives. All images were captured under identical conditions.

2.6 Figures and Tables

Table 2- 1. Summary of patients' *OPA1* mutations and clinical symptoms

***OPA1* Genotype**		
	Patient 1	Patient 2
Mutation	NM_130837.3:c.1948dup; NP_570850.2:p.(Glu650GlyfsTer4)	NM_130837.3:c.1417_1418del; NP_570850.2:p.(Ile473PhefsTer12)
Effect	Truncated protein (652 vs 1,015 amino acids)	Truncated protein (483 vs 1,015 amino acids)
Exon affected	19	13
Location	Central dynamin region	GTPase domain
Clinical Presentation		
	Patient 1	Patient 2
Visual Acuity	Right (OD): 20/100 -1 Left (OS): 20/150	Right (OD): 20/25 Left (OS): 20/25
IOP	OD: 16, OS: 15	OD: 14, OS: 14
Other	Slight hearing problems; cataract	Largely asymptomatic

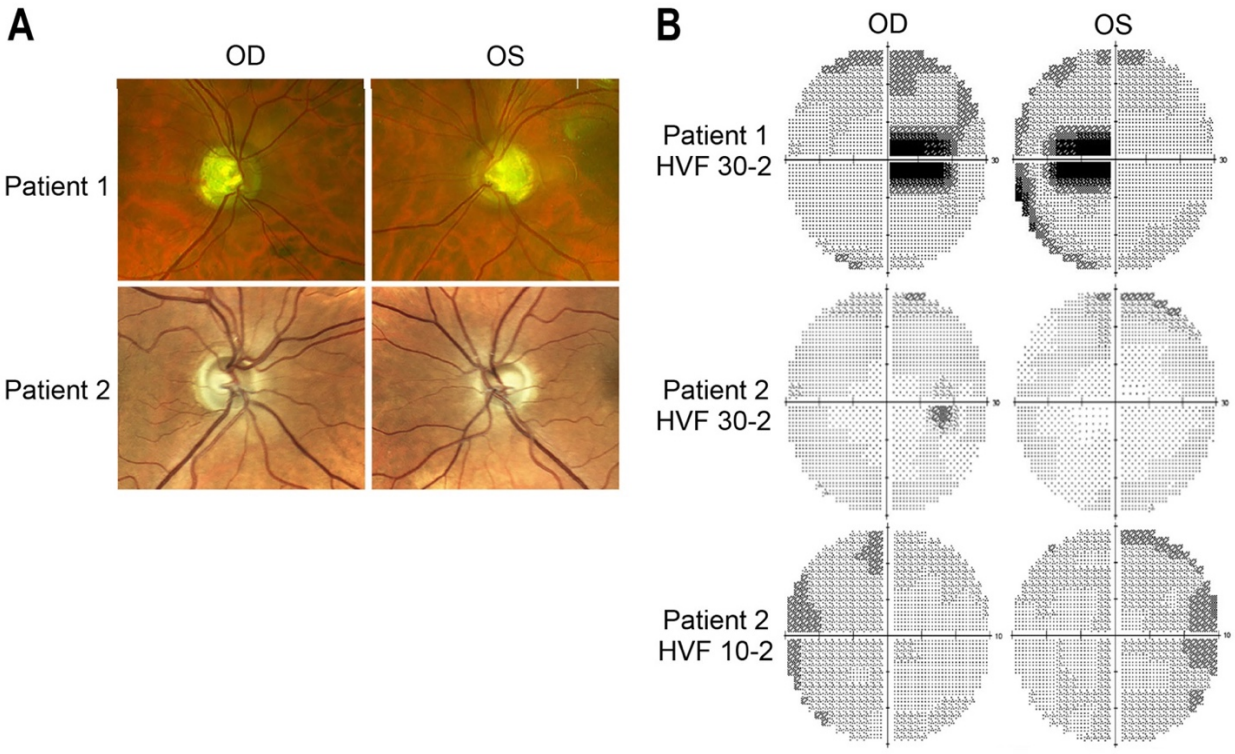

Figure 2- 1. Fundus imaging and visual field testing

(A) Fundus images of Patient 1 and Patient 2 displaying bilateral, temporal optic nerve pallor. (**B)** Humphrey visual field (HVF) testing reports. Patient 1's HVF 30-2 showed bilateral, temporal, paracentral scotomas. Patient 2's HVFs detected small paracentral scotomas. OD: *oculus dexter*, right eye; OS: *oculus sinister*, left eye.

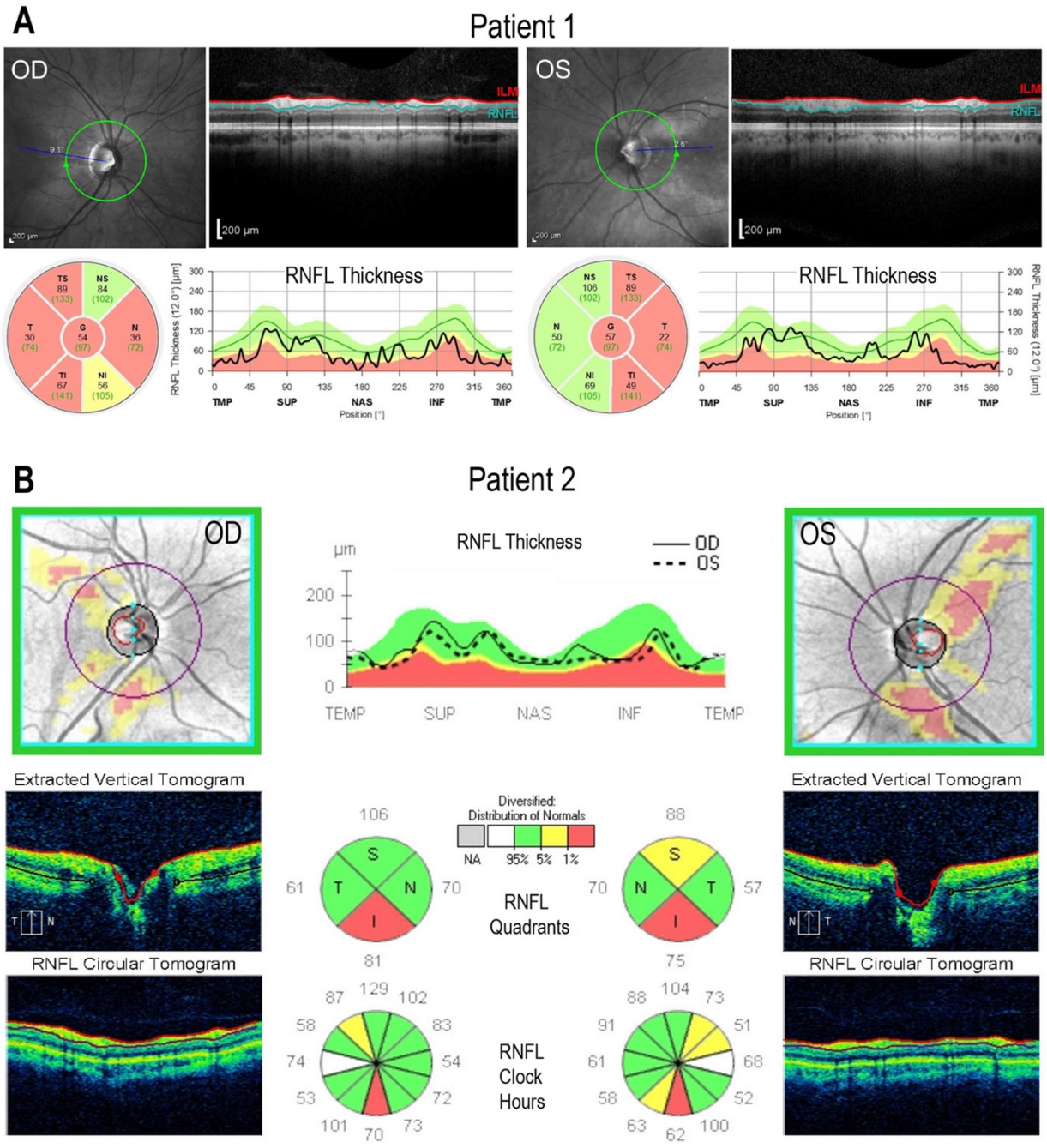

Figure 2- 2. Retinal lamination imaging by optical coherence tomography

(A) Patient 1's optical coherence tomography (OCT) results demonstrate bilateral retinal nerve fiber layer (RNFL) thinning, most significantly in the temporal zone, involving both superior and inferior regions. **(B)** Patient 2's OCT results reveal bilateral, inferior RNFL thinning,

accompanied by some superior fiber loss in both retinas. ILM: inner limiting membrane; RNFL: retinal nerve fiber layer; TMP (T): temporal; SUP (S): superior; INF (I): inferior; NAS (N): nasal.

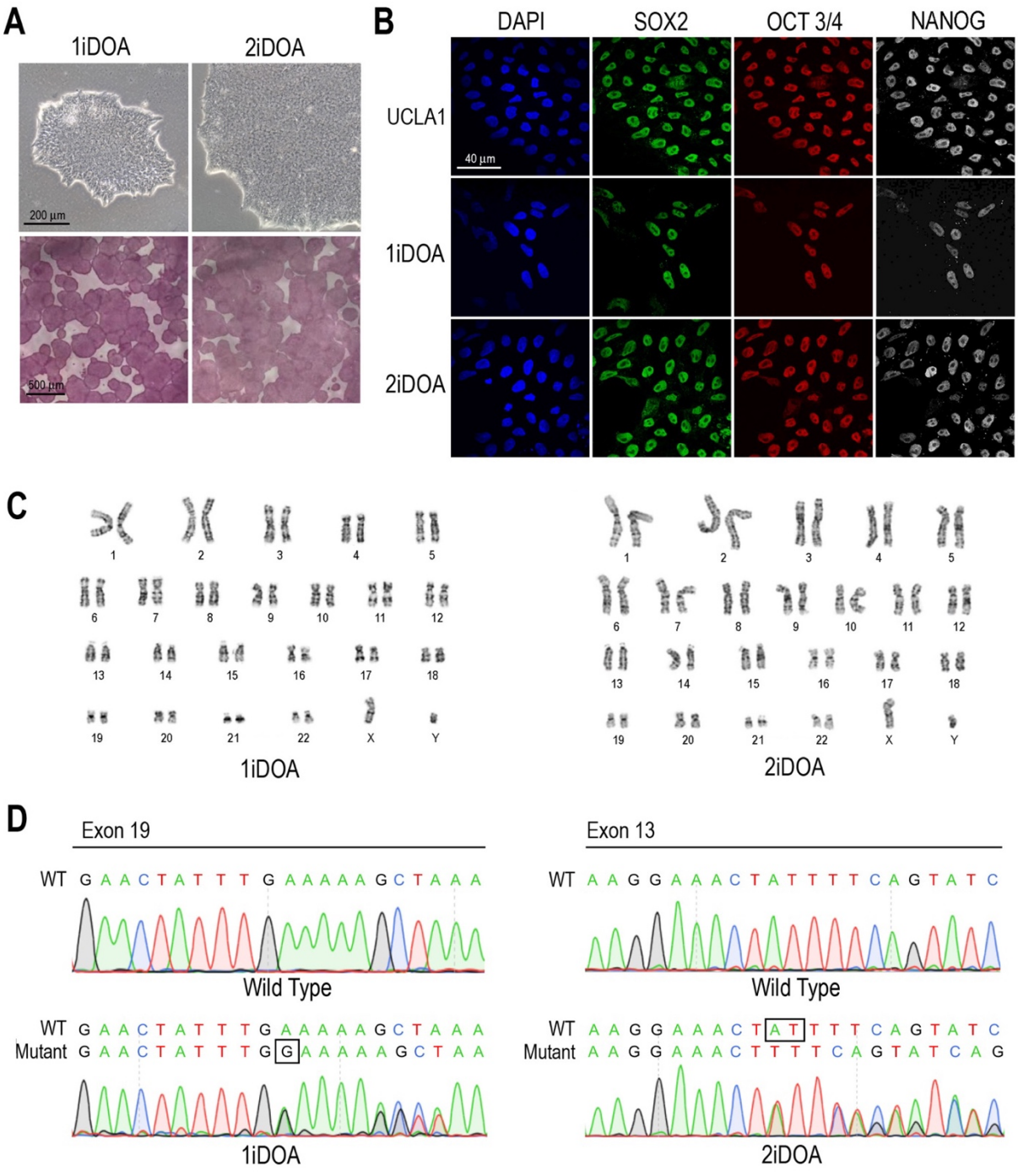

Figure 2- 3. Characterization of *OPA1* mutant iPSCs from DOA patients

(A) Brightfield images of iPSCs reprogrammed from DOA Patients 1 (1iDOA) and 2 (2iDOA) display normal pluripotent stem cell morphology (top row) and stain positive for alkaline phosphatase (bottom row). Scale bars: 200 µm (top row), 500 µm (bottom row). **(B)** 1iDOA and

2iDOA iPSCs express the pluripotent stem cell markers SOX2, OCT3/4, and NANOG similarly to the WT ESC line, UCLA1. Scale bar: 40 μm, all panels. **(C)** Both iPSC lines display a 46, XY normal, male karyotype. **(D)** DNA sequences of iPSC lines 1iDOA and 2iDOA (bottom row) aligned to the corresponding regions of *OPA1* in the WT reference genome (top row). Sequences confirm that 1iDOA contains a heterozygous, single base pair (G) insertion in exon 19 and that 2iDOA has a heterozygous, two base pair (AT) deletion in exon 13. Peaks reflect both WT and mutant allele bases at a given position. Allele sequence identities are clarified above peaks. Boxed regions indicate bases inserted (1iDOA, mutant allele) or deleted (2iDOA, WT allele).

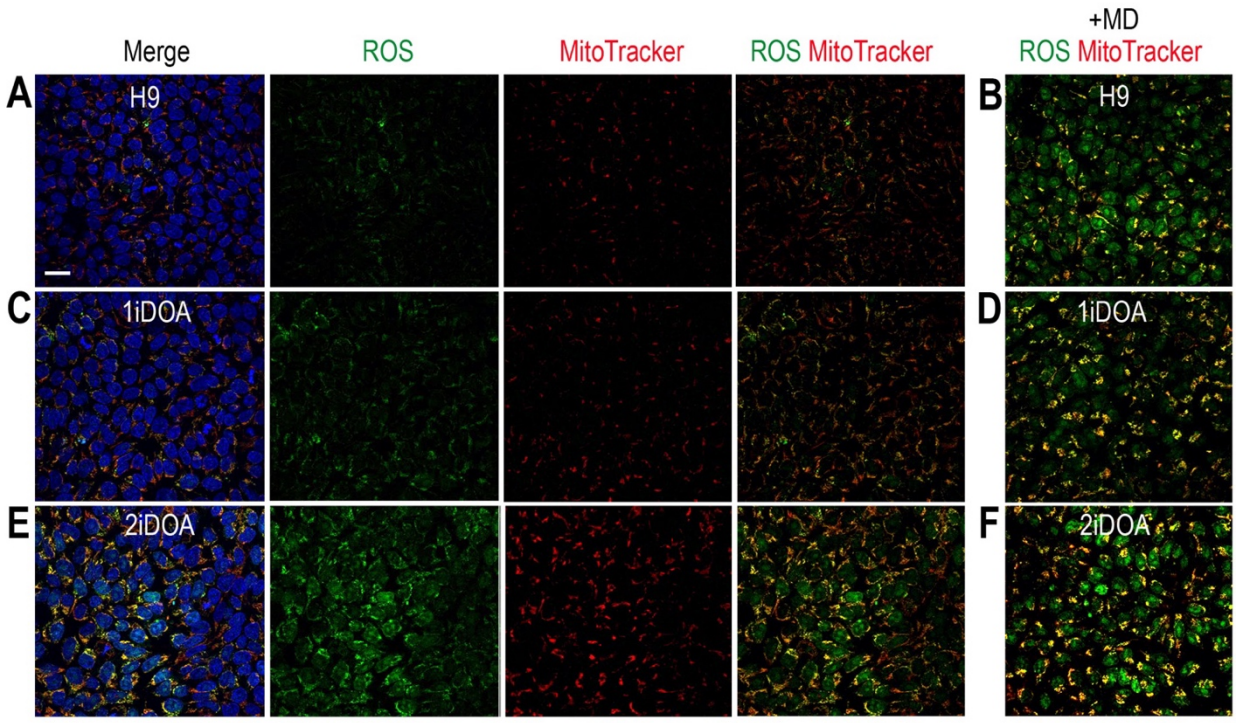

Figure 2- 4. Detection of ROS production in PSC lines

Detection of mitochondria and cellular ROS in pluripotent stem cell (PSC) lines was performed using live cells. (**A, C, and E**) Representative signals of ROS (green) and MitoTracker (red) in 1iDOA, 2iDOA, and H9 PSCs. ROS and MitoTracker signals are overlaid in the far right panels and nuclei are also shown via DAPI staining in the far left panels. (**B, D, and F**) Representative ROS and MitoTracker signals after the PSC lines were treated with menadione for 1 hour to induce ROS. Scale bar: 20 μm, all panels. ROS: Reactive oxygen species.

2.7 Supplementary Tables

Supplementary Table 2- 1. Antibodies and Fluorescent Reagents

	Antibody	Company	Catalog Number	Dilution or Final Concentration
Primary	SOX2	Santa Cruz	sc17320	1:50
	NANOG	abcam	ab21624	1:100
	OCT3/4 (C-10)	Santa Cruz	sc5279	1:50
Secondary	Donkey α goat Alexa Fluor® 488	Invitrogen	A-11055	1:500
	Donkey α rabbit Alexa Fluor® 647	Invitrogen	A-31573	1:500
	Donkey α mouse Alexa Fluor® 594	Invitrogen	A-21203	1:500
Other Reagents	DAPI	Sigma	D9542	10 μg/mL
	Hoechst 33342	Invitrogen	H3570	5 μg/mL
	MitoTracker Red CMXRos	Invitrogen	M7512	250 nM
	CellROX Green Reagent	Invitrogen	C10444	5 μM

Supplementary Table 2- 2. PCR and Sequencing Primers

Location	Direction, Use	Sequence
Exon 19	Forward, Sequencing	5'—CCTCCCTTTGGTTATCTCTG—3'
	Forward, PCR	5'—CACATAACGTGAACAAGTGT—3'
	Reverse, PCR and Sequencing	5'—TACTCAGAATGGAGAACCTG—3'
Exon 12/13	Forward, PCR and Sequencing	5'—GTGAGCGTCTTATCTGAATGG—3'
	Reverse, PCR and Sequencing	5'—CCCCTGTGTCTACATTATAGC—3'

CHAPTER 3

The impact of *OPA1* heterozygous and homozygous loss-of-function mutations on the morphology and function of human pluripotent stem cell mitochondria

3.1 Introduction

Dominant optic atrophy (DOA; OMIM #165500) is the most common inherited optic neuropathy worldwide. In most populations, the disease prevalence is 1:25,000-1:35,000, but it can be as high as 1:10,000 in areas with an established founder effect. Usually within the first two decades of life, individuals with DOA begin to lose their retinal ganglion cells (RGCs), which are essential for vision[35,37-40,42,131]. RGCs transmit inputs received from other retinal neurons to the brain for visual processing via their long axons, which converge to form the optic nerve[1,5]. Most individuals' DOA is caused by heterozygous mutations in the gene *optic atrophy 1* (*OPA1*; OMIM:*605290), which encodes a dynamin-related GTPase[17,18]. Although *OPA1* is expressed by most tissues, the majority of DOA cases are non-syndromic and patients only exhibit visual symptoms related to RGC degeneration—namely progressive, bilateral vision loss. A hallmark of DOA that aids in its diagnosis is temporal optic nerve head pallor, which is attributed to the preferential loss of RGCs in the papillomacular bundle[41,47]. Other symptoms include reduced visual acuity, color vision defects, and central visual field defects[39,42-45].

Notably, there is a high level of heterogeneity in the *OPA1* mutations DOA patients have. To date, over 500 pathogenic *OPA1* mutations have been reported (http://www.LOVD.nl/OPA1), and depending on the type and location of the mutation, disease can occur via dominant negative or haploinsufficient mechanisms[48,158]. Furthermore, although autosomal dominant, *OPA1* mutations are only ~43-88% penetrant [45,49]. Patients vary widely in their disease presentation from asymptomatic to legally blind, even within families harboring the same mutation[39,52,53]. Despite studies' attempts to draw genotype-phenotype correlations or to infer novel *OPA1* variants'

pathogenicity based on their genomic location or mechanism of action, overarching conclusions have remained largely elusive[39,64,130,131].

Molecularly, the human *OPA1* gene has eight mRNA isoforms that result from the alternate splicing of three of its 31 exons (4, 4b and 5b)[48,97]. All eight OPA1 precursor proteins contain an N-terminal mitochondrial targeting sequence (MTS) that allows them to enter into mitochondria where they are further processed into long and short protein isoforms[92]. Cleavage of the MTS by the mitochondrial processing peptidase (MPP) generates long isoforms (L-OPA1) that are anchored to the inner mitochondrial membrane (IMM). L-OPA1 can be further processed by peptidases at multiple downstream cleavage sites to generate short isoforms (S-OPA1) that are peripherally attached to the IMM or are diffuse in the intermembrane space (IMS)[91,93,94]. Dynamic regulation of L-OPA1 and S-OPA1 isoforms is essential to maintain and modulate mitochondrial functioning under both normal and stressed states.

Functionally, OPA1 acts to maintain mitochondrial structure and function by promoting mitochondrial fusion, maintaining cristae integrity, and supporting bioenergetic output. OPA1 promotes mitochondrial fusion together with the mitofusin proteins MFN1 and MFN2 (which are also dynamin-related GTPases)[109,110,172], and studies have shown that cells containing *OPA1* mutations or reduced levels of OPA1 protein have a fragmented mitochondrial network[18-20,82,88,89,94,134]. Interestingly, L-OPA1 isoforms are sufficient to maintain fusion, whereas S-OPA1 isoforms are not[92,113]. Independently of fusion, *OPA1* also regulates cristae structure and integrity[20,117]. *In vitro* studies have shown that *OPA1* dysfunction leads to a dramatic disorganization of mitochondrial ultrastructure in human cell lines and patient fibroblasts[20,85,130]. Furthermore, cristae structure and integrity have been directly related to mitochondrial respiratory efficiency[118]. OPA1 has been shown to stabilize supercomplexes of the respiratory chain—also located in the IMM—by maintaining cristae shape, and defects in *OPA1* have been associated with decreases in mitochondrial ATP synthesis, oxygen consumption rate (OCR), and the bioenergetic efficiency of the respiratory complexes[19,75,82,113,118,134,173,174].

Although DOA has been clinically characterized and *OPA1* has been studied extensively, RGCs' particular susceptibility to degenerate over other cell types when OPA1 functioning is compromised remains unclear. Studies have failed to show a direct link between one or more biological processes that are disrupted by *OPA1* mutations and one or more features specific to human RGCs. Rodents do not have as many *OPA1* mRNA isoforms as humans do because of differences in alternative splicing, and human cell types other than RGCs are not affected in ~80% of individuals with *OPA1* mutations[54,90,93]. This necessitates that human RGCs be examined to elucidate the pathological mechanisms responsible for their *OPA1*-mediated degeneration. It is likely that the RGC death observed in DOA patients is a result of *OPA1*-mediated mitochondrial dysfunction coupled with RGCs' high energy requirements and unique architecture—particularly their long axons that are partially unmyelinated[175-177]. However, proving this has been difficult due to the rarity of primary retinal tissues and scarcity of RGCs, which only comprise ~2% of the total retinal cells[14-16].

Here, we describe the generation of human *OPA1* mutant pluripotent stem cell (PSC) lines that can be differentiated into RGCs to establish human *in vitro* disease models of DOA. To definitively attribute observed phenotypic differences to the presence or absence of an *OPA1* mutation, wild-type (WT) and *OPA1* mutant cells being compared to one another should otherwise have identical genetic backgrounds. To this end, we established multiple isogenic pairs of WT and *OPA1* mutant PSC lines. First, we performed CRISPR-Cas9 gene editing on a WT embryonic stem cell (ESC) line to generate isogenic *OPA1* heterozygous and homozygous mutant ESC lines; these lines are predicted to have complete loss of OPA1 function on one or both alleles, respectively. To our knowledge, this is the first report of an *OPA1* homozygous loss of function ESC line. Separately, we established another set of isogenic WT and *OPA1* mutant PSC lines by using CRISPR-Cas9-mediated homology directed repair (HDR) to correct the *OPA1* mutation present in 1iDOA iPSCs (see sections 2.3.1 and 2.3.2 regarding the generation of 1iDOA iPSCs).

To ensure that all of the WT and *OPA1* mutant PSC lines generated could be reliably used to establish human disease models and to study the role of *OPA1* in human disease, we classified their OPA1 expression levels and verified that OPA1 correctly localized to the mitochondria. Although the majority of DOA patients with *OPA1* mutations only present with ophthalmological symptoms related to their RGC degeneration, others have reported that molecular and functional differences exist between WT and *OPA1* mutant PSCs[134,138]. This suggests that *OPA1* mutations could play a role over the course of development in driving disease, as opposed to only affecting RGCs that have reached maturity. Therefore, given OPA1's mitochondrial roles, we proceeded to characterize the *OPA1* WT, heterozygous mutant, and homozygous mutant PSC lines' mitochondrial morphology and bioenergetic output. Although *OPA1*'s effect on PSC mitochondrial morphology remains unclear, basal and maximal respiration, reserve capacity, and mitochondrial ATP production were consistently reduced in *OPA1* mutant PSC lines compared to WT controls.

3.2 Results

3.2.1 Generation of isogenic *OPA1* mutant ESC lines using CRISPR-Cas9 gene editing

To generate *in vitro*, human, DOA disease models, one must first obtain or generate PSCs containing *OPA1* mutations. In order to create both *OPA1* heterozygous and homozygous mutant ESC lines, I used CRISPR-Cas9 gene editing. Notably, because the mutant lines generated will be isogenic to, or have the same genetic background as, the WT line from which they were derived, this approach allows phenotypic differences observed between the ESC lines to be attributed directly to their *OPA1* genotype. As such, the WT human ESC line, UCLA1 was electroporated with ribonucleotide protein (RNP) complexes consisting of a single guide RNA (sgRNA) targeting exon 1 of the *OPA1* gene (sgRNA_exon1) and Cas9 protein. The sgRNA was designed to bind near the *OPA1* translation start site (TSS) to maximize the disruption of protein production from one or both alleles (**Figure 3-1A**). After electroporation, the UCLA1 ESCs were expanded, and genomic DNA was extracted from the population of cells to determine

sgRNA_exon1's editing efficiency. Sanger sequencing traces from the edited population of UCLA1 ESCs were compared to traces from non-edited UCLA1 ESCs using the Inference of CRISPR Edits (ICE) tool, which calculates the percentage of insertions or deletions (INDELS) generated by the non-homologous end joining (NHEJ) pathway after Cas9 creates a double-stranded break (DSB)[178]. Results indicated that sgRNA_exon1 was 97% efficient, and 82% of the edits generated were predicted to disrupt OPA1 protein function (not shown).

To identify cells with edits that would allow for the establishment of heterozygous or homozygous *OPA1* loss-of-function ESC lines, a portion of the edited cell population was subsequently plated as single cells at clonal density. Once single cell-derived colonies were large enough, genomic DNA was harvested, and the genomic region flanking the *OPA1* DSB site was amplified via PCR and then Sanger sequenced. The ICE program was used to identify individual clones that were genetically homogenous and contained indels that led to an early stop codon on one or both alleles (thereby generating *OPA1* heterozygous mutant and *OPA1* homozygous mutant ESC lines, respectively). Notably, because sgRNA_exon1 was so efficient, we were only able to identify a single clone that we hypothesize can serve as an *OPA1* heterozygous loss-of-function line. This line, named E10, technically has compound heterozygous *OPA1* mutations (**Supplementary Table 3-1**). One allele, here called "allele 1," is identical to the WT *OPA1* sequence, save a G>A missense mutation that changes the fifth amino acid, arginine, to histidine (**Figure 3-1B**). Although we cannot rule out that this missense mutation has a deleterious effect on OPA1 functioning, arginine and histidine both have positively charged side chains, and prediction software scored the mutation as having a very low likelihood of being pathogenic[179]. E10's other allele, "allele 2," has a 16 base pair deletion and 3 base pair insertion that disrupts the TSS/ATG start codon (**Figure 3-1B**). Because allele 1's missense mutation is not predicted to cause disease and allele 2 is not predicted to encode any OPA1 protein, we believe that E10 can be used to model "true" haploinsufficiency, meaning cells have lost the function of an entire OPA1 allele, or 50% of OPA1 expression.

Separately, we identified a clone containing the same one base pair insertion on both alleles (**Supplementary Table 3-1**). This *OPA1* homozygous mutant line was named D9 and is predicted to encode an OPA1 protein product only 11 amino acids long (**Figure 3-1B**). The protein terminates immediately prior to exon 2, and because the stop codon is prior to the N-terminal transmembrane (TM) domain on both alleles, the shortened OPA1 protein is not expected to localize correctly to the IMM or to generate L-OPA1 or S-OPA1 isoforms[91,92]. Given that *Opa1* knockout mice are embryonic lethal[88,89] and that there have not been any reports to our knowledge of a human *OPA1* homozygous loss-of-function human PSC line to date, we were surprised to find that D9 PSCs are able to survive in culture similarly to WT PSCs. Both E10 and D9 PSCs exhibit normal pluripotent stem cell morphology (**Figure 3-1C**) and express pluripotent stem cell markers similarly to the WT ESC line from which they were derived, UCLA1 (**Figure 3-1D**).

3.2.2 Generation of the line 1iDOA-CR via CRISPR-Cas9 correction of 1iDOA's *OPA1* mutation

Given that iPSCs confer different advantages than ESCs when used to generate disease models, we previously also generated two *OPA1* heterozygous mutant iPSC lines, 1iDOA and 2iDOA, by reprogramming DOA patients' peripheral blood mononuclear cells (PBMCs) into iPSCs (section 2.3.2). Phenotypic findings from iPSC-derived, *in vitro* disease models can be compared back to patients' clinical records to determine how closely the model recapitulates patients' disease symptoms. However, to have a true isogenic WT control to compare these lines with, the iPSC lines' mutations must be corrected. In order to have another isogenic pair of WT and mutant *OPA1* PSCs to model and study DOA, we used CRISPR-Cas9-mediated homology directed repair (HDR) to correct the heterozygous *OPA1* mutation NM_130837.3:c.1948dup, NP_570850.2:p.(Glu650GlyfsTer4) in exon 19 of 1iDOA iPSCs.

For HDR to occur, 1iDOA iPSCs were nucleofected with RNPs consisting of sgRNA_exon19 and Cas9 protein, along with a single-stranded oligodeoxynucleotide (ssODN)

repair template. The sgRNA, sgRNA_exon19, was designed to take advantage of the fact that 1iDOA iPSCs' *OPA1* mutation (a one base pair G insertion) creates a PAM site unique to the mutant allele (**Figure 3-2A, B**). This provides a dual advantage that, 1. only the mutant allele will be cut by Cas9, and 2. the corrected allele will avoid further cutting activity by Cas9 as correcting the mutation simultaneously removes the PAM site. The ssODN/HDR donor template was designed to be complementary to the target strand and purchased as an Ultramer from Integrated DNA Technologies (IDT) in regards to previous literature[180]. The template was 124 base pairs in length (60 base pair homology arms, beginning left of the Cas9 cut site and right of the last base discrepancy between the target sequence and the ssODN), and included IDT's Alt-R HDR modifications to increase oligo stability and rate of repair (**Supplementary Table 3-2**). Sequence modifications in the ssODN eliminate the G insertion mutation and introduce a silent mutation (T>C, **Figure 3-2A**). Removing the G insertion corrects 1iDOA's *OPA1* mutation and eliminates the PAM site, preventing further editing of the corrected allele after successful recombination. The silent mutation introduces a novel BstBI restriction enzyme site on the corrected allele (**Figure 3-2A, B**) that facilitates the identification of correctly edited clones and allows the corrected 1iDOA line to be distinguished from other *OPA1* WT lines. We identified one clone that was correctly edited, and named it 1iDOA-CR (for 1iDOA CRispr CoRrected). Successful recombination in 1iDOA-CR iPSCs was verified via Sanger sequencing (**Figure 3-2B**) and restriction digest (**Figure 3-2C**). Importantly, following CRISPR-Cas9 gene editing, we show that 1iDOA iPSCs whose *OPA1* mutation was successfully corrected (1iDOA-CR iPSCs) remained karyotypically normal (**Figure 3-2D**) and continued to express the pluripotency markers OCT3/4, SOX2, and NANOG (**Figure 3-2E**).

3.2.3 PSCs with *OPA1* mutations that lead to early stop codons express the same OPA1 isoforms as *OPA1* WT PSCs at reduced levels

The *OPA1* genotypes of all PSC lines discussed in this paper are summarized in **Supplemental Table 3-1**. 1iDOA and 2iDOA are iPSC lines that we previously generated from DOA patients with distinct *OPA1* heterozygous mutations (see sections 2.3.1 and 2.3.2). All *OPA1* heterozygous mutant (E10, 1iDOA, and 2iDOA) and homozygous mutant (D9) lines generated are predicted to have early stop codons on one or both alleles of *OPA1*. To examine how these mutations affect the expression of total OPA1 protein, as well as the expression and ratio of long and short OPA1 protein isoforms, we performed western blot analysis using an OPA1 antibody that binds to amino acids 708-830 (BD Biosciences, #612606). In the longest *OPA1* transcript, isoform 8 (NM_130837.3), this region of amino acids falls within exons 20-23 and is downstream of all the *OPA1* mutant PSC lines' predicted stop codons. Therefore, the OPA1 antibody should not bind to truncated OPA1 proteins produced from E10, 1iDOA, 2iDOA, or D9's mutant alleles.

(Two separate western blots are depicted in **Figure 3-3A**. The blot on the left was run after E10 and D9 were generated from WT UCLA1 ESCs, and confirmed the OPA1 protein expression profiles predicted from their respective genotypes. The blot on the right was run to compare the relative OPA1 protein levels across all *OPA1* WT, heterozygous, and homozygous mutant PSC lines generated and/or examined in this dissertation.)

As expected, we see around a 50% reduction in the level of OPA1 protein expressed in the heterozygous mutant lines E10, 1iDOA, and 2iDOA, and no OPA1 protein expression in the homozygous mutant line D9 (**Figure 3-3A**). Notably, because the OPA1 antibody binds downstream of 1iDOA, 2iDOA, and D9's shortened protein products, we cannot determine the level at which these mutant proteins are expressed, or in the case of 1iDOA and 2iDOA, whether their truncated OPA1 protein products dominantly interfere with WT OPA1 protein functions. However, it is likely their *OPA1* mutations cause DOA via haploinsufficiency. E10 and D9 are also

predicted to cause pathogenesis via lack of adequate WT *OPA1* expression on one or both alleles, respectively.

Separately, western blot results also demonstrate that correction of 1iDOA's mutation restores OPA1 expression to levels comparable with the other *OPA1* WT lines, H9 and UCLA1 (**Figure 3-3A**, right). Interestingly, under normal PSC culture conditions, the *OPA1* WT and mutant PSC lines appear to uniformly express all OPA1 protein isoforms. Bands a and b represent L-OPA1 isoforms while bands c-e represent S-OPA1 isoforms (**Figure 3-3A**). COX4 was used as a mitochondrial loading control, and its similar expression levels across all PSC lines suggest that a reduction in OPA1 protein can be attributed to a line's *OPA1* mutation(s) rather than a change in cells' mitochondrial mass (**Figure 3-3A**, right).

We further examined OPA1 expression levels and investigated the protein's localization in PSCs via immunofluorescence. OPA1 colocalized with the outer mitochondrial membrane protein TOM20, indicating that it correctly homes to the mitochondria (**Figure 3-3B**). In agreement with western blot results, immunofluorescent images demonstrated that *OPA1* mutant PSCs expressed lower levels of OPA1 compared to WT PSCs, and that correcting 1iDOA's *OPA1* mutation increased OPA1 expression levels. Similarly to how all cell lines expressed similar levels of COX4 (**Figure 3-3A**, right), all lines demonstrated robust TOM20 expression, again indicating that *OPA1* mutant PSCs' reduced levels of OPA1 are caused by their mutation(s) and cannot be attributed to a reduction in the amount of mitochondria present in the cells (**Figure 3-3B**).

3.2.4 Super resolution microscopy reveals PSC mitochondria can be "structured" or "diffuse"

We next examined if *OPA1* mutations affected PSCs' mitochondrial morphology. PSCs were stained with anti-OPA1 and anti-TOM20 antibodies (**Supplementary Table 3-4**), the latter of which was used to visualize the mitochondrial network of each cell, and then imaged at a high resolution using structured illumination microscopy (SIM). Traditionally, mitochondrial networks

have been described as being either “filamentous/elongated/tubular,” or “fragmented/punctated”[20,94,95]. However, at high resolution, individual mitochondria are more visible and distinguishable, and I found that PSC’ mitochondria are better described as being more “structured” or “diffuse.” Structured mitochondria have more defined outer mitochondrial membranes, and are distinguishably more oval or circular in shape. Diffuse mitochondria lack distinguishable borders/membranes and do not form distinguishable shapes. When comparing the isogenic ESC lines UCLA1, E10, and D9 to one another, D9’s mitochondria consistently appeared more diffuse than UCLA1 and E10’s mitochondria (**Figure 3-4**, left column). UCLA and E10 had more structured networks of mitochondria that in many areas looked highly similar. However, UCLA1 had more mitochondria that were individually distinguishable due to their round shape. When comparing the iPSC lines 1iDOA-CR, 1iDOA, and 2iDOA to one another, all lines had mostly structured mitochondrial networks (**Figure 3-4**, right column). Interestingly however, both *OPA1* heterozygous mutant lines had more mitochondria than 1iDOA-CR that were individually distinguishable due to their round shape (**Figure 3-4**, right column).

OPA1 expression loosely correlated with TOM20 expression in all cell lines examined, and extra-mitochondrial expression was observed (**Figure 3-4**). Although the OPA1 antibody used appears specific in western blot and lower magnification immunofluorescent staining applications, some non-specificity may be present at the super resolution scale. This extra-mitochondrial antibody localization will need to be further investigated further before definitive conclusions can be drawn from super resolution images regarding OPA1 localization patterns or expression levels.

3.2.5 *OPA1* loss of function on one or both alleles progressively decreases PSCs’ OCR and mitochondrial ATP production compared to isogenic *OPA1* WT PSCs

Lastly, we investigated whether *OPA1* mutations affect the functioning of PSC mitochondria. We used the Seahorse assay (Agilent) to first measure differences in the

bioenergetics of the isogenic ESC lines UCLA1, E10, and D9. Approximately 24 hours after the *OPA1* mutant and WT PSCs were uniformly plated in mTeSR plus culture medium (Stemcell Technologies), cell lines' oxygen consumption rate (OCR) and extracellular acidification rate (ECAR) were simultaneously measured and used to estimate their oxidative phosphorylation and glycolysis activity levels. In comparison to UCLA1 *OPA1* WT PSCs, isogenic E10 *OPA1* heterozygous mutant PSCs displayed reduced levels of basal, maximal, and ATP-linked respiration, as well as a decreased reserve capacity. In line with their bi-allelic *OPA1* mutations, D9 PSCs exhibited the largest reduction in all these parameters compared to UCLA1 PSCs (**Figure 3-5A, C**). Conversely, levels of basal and oligomycin-induced ECAR were unchanged across the isogenic lines (**Figure 3-5B, D**). In accordance with these trends, the mitochondrial ATP production rate was significantly elevated in UCLA1 cells compared to E10 cells, and in E10 cells compared to D9 PSCs, whereas the glycolytic ATP rate was unchanged across the isogenic lines (**Figure 3-5E**). However, given that ESCs predominantly use glycolysis as an energy source, UCLA1, E10, and D9 ESCs did not have significantly different rates of total ATP production (**Figure 3-5E**).

We also included the WT ESC line H9 in the experiment as another WT reference point, given that differences in the genetic background of PSC lines have been shown to cause variation in their behavior[181,182]. H9 and UCLA1 were not significantly different across most bioenergetic parameters, but H9's lower trending OCR and higher trending ECAR led it to have a significantly lower ratio of OCAR/ECAR (**Figure 3-5D**). Interestingly H9's OCR-associated parameters, mitochondrial ATP production, and total ATP production were not significantly higher than those of E10, but were significantly higher than those of D9 (**Figure 3-5C, E)**. These results highlight the importance of comparing cell lines that have the same genetic background when assessing the impact of genetic mutation(s).

3.2.6 The *OPA1* heterozygous mutant iPSCs 1iDOA and 2iDOA demonstrate decreased OCR, ECAR, and ATP production compared to the *OPA1* WT PSCs H9 and 1iDOA-CR

We additionally examined the OCR, ECAR, and ATP production rates of our second set of isogenic PSC lines, 1iDOA and 1iDOA-CR, along with H9 and 2iDOA. *OPA1* WT control ESCs (H9), *OPA1* mutant iPSCs (1iDOA and 2iDOA), and 1iDOA CRISPR corrected iPSCs (1iDOA-CR) were analyzed using a Seahorse XFe96 Analyzer approximately 24 hours after being plated in mTeSR plus culture medium (Stemcell Technologies). Both 1iDOA and 2iDOA had reduced levels of basal, maximal, and ATP-linked respiration, as well as a decreased reserve capacity, compared to the WT PSC lines H9 and 1iDOA-CR (**Figure 3-6A, C**). In contrast to the isogenic ESC lines UCLA1, E10, and D9 however, 1iDOA and 2iDOA also had significantly lower levels of ECAR compared to WT PSCs (**Figure 3-6B, D**). Therefore, because mutant cells' OCAR and ECAR both decreased compared to WT cells, all PSC lines in the assay did not have significantly different ratios of OCAR/ECAR (**Figure 3-6D**). As expected, the ratios demonstrate that all PSC lines use glycolysis more than oxidative phosphorylation. In concordance with mutant PSCs' reduced OCAR and ECAR, mitochondrial, glycolytic, and total ATP rates were also significantly reduced in mutant compared to WT PSCs (**Figure 3-6E**). When comparing the two WT PSC lines, 1iDOA-CR had a significantly higher ECAR than H9, and consequently, a higher glycolytic ATP production rate (**Figure 6B, D, E**). Otherwise, H9 performed much more similarly to 1iDOA-CR (**Figure 3-6**) than to UCLA1 (**Figure 3-5**).

3.3 Discussion

Although *OPA1* has been extensively studied in multiple human cell lines and readily accessible cell types such as fibroblasts, these studies do not address the main conundrum in the field of DOA research: why are RGCs particularly sensitive to *OPA1* mutations? To be able

to better answer this question, we generated iPSC lines from DOA patients with *OPA1* mutations and used gene editing technology to generate *OPA1* heterozygous and homozygous loss-of-function mutant ESC lines. Using existing differentiation protocols, these *OPA1* mutant PSC lines can then be used to generate human RGCs *in vitro*, which can be compared to WT PSC-derived RGCs to better understand *OPA1*'s role in driving DOA pathogenesis. Using both *OPA1* ESC and iPSC lines for disease modeling is ideal, as each confers their own specific advantages as a model. Since the advent of gene editing technology, we are no longer restricted to studying *OPA1* mutations that occur naturally in human patients. By using CRISPR-Cas9 to edit the WT ESC line, UCLA1, we were able to derive *OPA1* mutant ESC lines that lack a functional OPA1 protein on one or both alleles. These lines can serve as valuable research tools to better understand *OPA1*'s role in development and disease. Editing a WT cell line is also advantageous in that all derivative lines will be isogenic, or have the same genetic background as one another. By comparing isogenic human PSC lines either with or without *OPA1* mutations, we can more confidently attribute phenotypic differences observed *in vitro* to a line's *OPA1* mutation and avoid issues of incomplete penetrance observed in patient pedigrees.

Conversely, iPSC lines derived from DOA patients with *OPA1* mutations must be corrected *in vitro* using gene editing to generate an isogenic control iPSC line to which the mutant cells can be compared. However, iPSCs are advantageous as *in vitro* phenotypes of DOA patients' iPSC-derived RGCs can be directly compared back to the patients' ophthalmological data. Observations from a patient's cells *in vitro* and his/her clinical manifestations of disease will provide reciprocal insights that will aid in validating how closely our PSC-based model recapitulates the DOA patient's disease symptoms and in informing what mechanisms underlie these symptoms. Given the heterogeneity of *OPA1* genotypes and phenotypes present in the DOA patient population, examining a range of PSC lines with differing *OPA1* mutations will be necessary to fully understand *OPA1*-driven DOA pathogenesis.

Therefore, the PSC lines we generated in this chapter and in Chapter 2 are distinct from those previously reported in the literature (**Supplementary Table 3-1**; section 1.5.1).

In examining the WT and *OPA1* mutant PSC lines we generated, we observed that the *OPA1* heterozygous mutant cells expressed the same signature of OPA1 isoforms as their WT counterparts, in agreement with previous findings[19,75,123,134]. However, as predicted by their nonsense mutations, the *OPA1* heterozygous mutant PSCs had reduced levels of OPA1 protein compared to WT PSCs, and correcting 1iDOA's mutation restored OPA1 protein expression to WT levels. All PSC lines expressed five OPA1 protein isoforms, named a-e[94], at relatively equal ratios. Interestingly, mouse embryonic fibroblasts (MEFs) and human embryonic kidney (HEK) 293T cells were also found to express OPA1 protein isoforms a-e[94]. This suggests that naïve cells initially express all[*] OPA1 protein isoforms and down or upregulate specific OPA1 isoforms to serve particular functional requirements as they acquire cell-specific fates (or during the process of fate specification). This also suggests that *OPA1* heterozygous mutant PSCs do not have altered transcriptional or post-translational OPA1 processing (which would cause them to express a different ratio of long to short OPA1 isoforms from WT PSCs) and that functional differences observed between WT and *OPA1* heterozygous mutant PSCs may result from differences in total OPA1 protein expression levels.

When visually examining the PSCs' mitochondria at super resolution, we did not find any drastic differences between the mitochondria of the WT and *OPA1* mutant PSC lines, morphologically speaking. At super resolution, I found it difficult to classify mitochondrial networks as either filamentous/elongated or fragmented/punctate, as has been the common practice, and instead describe mitochondria as falling on scale between being highly "structured" or fully "diffuse". The literature clearly demonstrates that cells lacking OPA1

[*]There were traditionally thought to be a total of five possible OPA1 protein isoforms, called a-e. A sixth isoform called d' was later discovered. I observe six isoforms in retinal organoids, but only detect five isoforms in PSCs when lysate was analyzed under the same conditions (**Chapter 4, Figure 4-5A).**

expression have highly fragmental mitochondrial networks[20,94]. Given that the *OPA1* homozygous loss-of-function mutant PSC line I generated expressed extremely low to no OPA1 protein via western blot and immunofluorescent staining assessments and displayed a highly diffuse mitochondrial network, I assume that diffuse mitochondria are equivalent to fragmental mitochondria. Conversely, the WT and *OPA1* heterozygous mutant PSC lines both had mitochondrial networks that were significantly more structured, meaning the outer mitochondrial membranes of individual mitochondria were more easily identifiable. Although *OPA1* mutations are generally associated with fusion defects, and by extension, fragmental mitochondria, a closer look at the literature reveals this is not always the case.

Before comparing our findings with those in the literature however, it is important to note that the PSCs were cultured in mTeSR medium (Stemcell Technologies), which contains a relatively high level of glucose (15 mM)[183]. Cells with an abundant source of glucose can rely on glycolysis to generate ATP, as opposed to oxidative phosphorylation. As glycolysis occurs independently of the mitochondria whereas oxidative phosphorylation requires functional mitochondria, the effects of *OPA1* mutations may only be detectable in cells reliant on oxidative phosphorylation. For instance, similar to our findings, Zanna *et al.* showed that the morphology of mitochondria in WT and *OPA1* heterozygous mutant fibroblasts grown in glucose medium (presumably containing 25mM of glucose) were not significantly different, and that there was a low abundance of fragmental mitochondria in these cells[75]. However, when the same WT and *OPA1* heterozygous mutant fibroblasts were grown in 5 mM galactose medium lacking glucose, the *OPA1* heterozygous mutant fibroblasts had a significantly higher number of fragmental mitochondria than the WT fibroblasts[75]. It would be interesting to assess if the *OPA1* heterozygous mutant PSC lines we generated exhibit increased mitochondrial fragmentation in galactose medium when forced to use their mitochondria for oxidative phosphorylation, and to compare their mitochondrial morphology to that of homozygous mutant PSCs in both glucose and galactose media.

Interestingly, another study conducted by Olichon *et al.* found that fibroblasts from one DOA patient had fragmental mitochondria while fibroblasts from a separate DOA patient had mitochondria that were filamentous like the control line[86]. All fibroblasts were cultured in RPMI-1640, which contains ~11 mM glucose (ThermoFisher Scientific). Interestingly, the fibroblasts that displayed a more fragmented mitochondrial network had an *OPA1* missense mutation, whereas the fibroblasts that retained a filamentous mitochondrial network had an *OPA1* mutation that led to an early stop codon[86]. Remarkably, all of the heterozygous mutant PSC lines I generated and all of the heterozygous mutant fibroblast lines described by Zanna *et al.* also had mitochondrial networks that lacked high levels of fragmentation and had *OPA1* mutations that led to an early stop codon. Interestingly, the *OPA1* missense mutation that caused fibroblasts to have more fragmental mitochondria[86] occurred in the GTPase domain, which is responsible for *OPA1*'s role in facilitating IMM fusion[105]. However, multiple PSC lines that have heterozygous *OPA1* mutations that cause early stop codons to occur prior to the GTPase domain do not have highly fragmental mitochondria in glucose media. This suggests that missense mutations in the GTPase domain cause pathogenesis by interacting with the other allele's WT copy of OPA1 to impair the cell's normal IMM fusogenic abilities.

Furthermore, in agreement with our findings, both aforementioned studies demonstrated that WT and *OPA1* heterozygous mutant cells with early stop codons did not differ in the specific OPA1 protein isoforms they expressed[75,86]. Conversely, the fibroblasts that had fragmental mitochondria and contained an *OPA1* missense mutation expressed a different OPA1 protein isoform signature than WT and *OPA1* haploinsufficient cells. Further investigation is needed to determine if *OPA1* missense mutations consistently cause mitochondrial fragmentation in glucose media and if the mitochondrial fragmentation and altered proteolytic processing observed are consistently linked processes. To this point, two additional studies demonstrated that another *OPA1* missense mutation also causes mitochondrial fragmentation, but the cell culture medium used in the studies was not reported[134,173]. In one of these studies,

fibroblasts carrying the *OPA1* missense mutation did not express different OPA1 protein isoforms than WT fibroblasts, suggesting that a cell's ability to control mitochondrial dynamics is not always reflected in which OPA1 protein isoforms it expresses[134].

It is also possible that the WT and *OPA1* heterozygous mutant PSCs we examined do have nuanced mitochondrial morphologies, and that an automated analysis of tens to hundreds of cells per line would reveal such nuances.

Regarding the *OPA1* WT, heterozygous mutant, and homozygous mutant PSC lines' bioenergetic functioning, interestingly, all *OPA1* mutant PSC lines had significantly decreased oxygen consumption rates (OCR) and mitochondrial ATP production rates compared to their isogenic WT controls. The *OPA1* mutant ESCs isogenic to the WT control ESC line, UCLA1, had significant decreases in reserve capacity and in their basal, maximal, and ATP-linked respiration that were proportional to the loss of *OPA1* function on one or both alleles (E10 and D9, respectively). Given OPA1's mitochondrial roles, it was not surprising that *OPA1* mutations affected cells' oxidative phosphorylation, but not glycolysis, efficiencies, which were estimated by cells' OCR and extracellular acidification rate (ECAR), respectively. Notably, as human PSCs predominately use glycolysis[184], the decrease in *OPA1* mutant PSCs' mitochondrial ATP production was not large enough to significantly decrease the lines' total ATP production; in other words, total ATP production was not significantly different across UCLA1, E10, and D9 ESCs. In support of these findings, we have not detected any growth defects in E10 or D9 ESCs under normal culture conditions (glucose). Therefore, *OPA1* mutant PSCs are able to maintain levels of ATP sufficient for normal functioning under standard PSC culture conditions regardless of their *OPA1* mutation(s), mitochondrial morphology, and reduction in oxidative phosphorylation efficiency. However, *OPA1* mutations likely do not have as marked effects on PSCs' overall health and functioning as they would on cells heavily reliant on oxidative phosphorylation, like the RGCs.

Interestingly, while the 1iDOA and 2iDOA *OPA1* heterozygous mutant iPSC lines also had a reduced reserve capacity and basal, maximal, and ATP-linked respiration rates compared to WT PSCs, they also had reduced basal and oligomycin-induced extracellular acidification rates, indicating that oxidative phosphorylation and glycolysis were impaired in DOA patients' iPSCs. Therefore, although total ATP production was significantly reduced in 1iDOA and 2iDOA iPSCs compared to WT controls, the *OPA1* mutant and WT PSCs did not have significantly different basal OCR:ECAR ratios, which as expected, indicated the PSCs favored glycolysis over oxidative phosphorylation. It will be interesting to assess whether ECAR is consistently reduced in 1iDOA and 2iDOA iPSCs or in other *OPA1* mutant PSC lines found in the literature, as studies tend only to report cells' oxygen consumption rates[124,134,185]. Regardless, we did not detect any obvious growth differences between WT and 1iDOA and 2iDOA PSCs, and given their OPA1 protein expression levels and not overly diffuse mitochondrial network morphologies, the level of ATP they are able to maintain is sufficient under the current culture conditions (section 3.4.1).

Additionally, in examining the bioenergetic profiles of the three WT PSC lines, H9, UCLA1, and 1iDOA-CR, it is apparent that cells' individual genetic backgrounds, in addition to their *OPA1* mutation status, influence their OCR, ECAR, and ATP production. This has also been observed by Sladen *et al*[132]. For instance, while H9 ESCs were significantly more glycolytic than UCLA1 ESCs, 1iDOA-CR iPSCs were more glycolytic than H9 ESCs. Interestingly, UCLA1 ESCs had a significantly higher ratio of basal OCR:ECAR than H9 ESCs that indicated they used oxidative phosphorylation and glycolysis relatively equally. In fact, the E10 *OPA1* heterozygous mutant ESCs isogenic to UCLA1 also had a significantly higher overall ratio of OCR:ECAR than H9 WT ESCs. These differences in basal bioenergetics may explain why individuals with the same *OPA1* mutation can vary drastically in the severity of DOA symptoms they present with, and emphasize the importance of using isogenic control lines when evaluating the effects of *OPA1* mutations.

3.4 Methods

3.4.1 Human pluripotent stem cell culture

Human ESCs and iPSCs were maintained in mTeSR plus medium (Stemcell Technologies) supplemented with 1% Antibiotic Antimycotic (Gibco/ThermoFisher Scientific) on Matrigel (Corning) coated plates. PSCs were passaged by dissociating monolayer cells into a single-cell suspension with Accutase (Stemcell Technologies). Single cells were plated in mTeSR plus supplemented with 1% Antibiotic Antimycotic and 10 μM Y-27632 (Stemcell Technologies) for 24 hours, after which media was replaced with mTeSR plus with 1% Antibiotic Antimycotic. Media was changed no less frequently than every other day. PSCs were maintained at 37°C, 5% CO_2.

3.4.2 Generation of isogenic *OPA1* mutant ESC lines using CRISPR-Cas9 gene editing

Human, wild-type, UCLA1 ESCs (NIH-0058) were grown on Matrigel (Corning) coated plates in mTeSR plus (Stemcell Technologies) supplemented with 1% Antibiotic-Antimycotic (Gibco/ThermoFisher Scientific) to 80% confluence and subsequently dissociated to a single-cell suspension using Accutase (Stemcell Technologies). RNPs composed of 300 pmol of the synthetic, single guide RNA, "sgRNA_exon1" (Synthego) (**Supplementary Table 3-2**), and 40 pmol of Cas9 protein (Synthego) were mixed with $5x10^5$ UCLA1 ESCs in P3 Primary Cell Nucleofector solution (Lonza) and nucleofected in a Lonza Nucleofector cuvette (S) using electroporation program CA-137 on a 4D-nucleofector with X-unit (Lonza). Nucleofected cells were cultured as a population in mTeSR plus, 1% Antibiotic-Antimycotic, and 10% Clone R (Stemcell Technologies); Clone R was removed after 24 hours. To assess the efficiency of CRISPR-Cas9 editing within the nucleofected cell population, genomic DNA was extracted from a portion of the cells using the Purelink genomic DNA mini kit (Invitrogen). DNA was amplified using Hot Star Taq DNA Polymerase (Qiagen) and PCR primers flanking the double-stranded DNA break site (XJY1349 and XJY1350, **Supplementary Table 3-3**). Thermocycler conditions

were as follows: 15 min at 95°C; 35 cycles of 30 seconds at 94°C, 30s at 66.3°C, and 1 min at 72°C; and 10 min at 72°C. PCR products were Sanger sequenced using primer XJY1350 (**Supplementary Table 3-3**). The rate of editing in the nucleofected population was assessed using the Inference of CRISPR Edits (ICE) tool (https://ice.synthego.com)[178]. A PCR-amplified DNA sequence from UCLA1 cells electroporated without any CRISPR reagents was used as a control file.

To enable clonal selection, a portion of cells from the nucleofected population was plated at a density of 1 cell/well in Matrigel-coated 96 well plates and cultured in mTeSR plus, 1% Antibiotic-Antimycotic, and 10% Clone R. Clone R was removed once colonies reached ~20 cells. Individual colonies were manually isolated and expanded. To determine if colonies were in fact derived from a single cell and genetically pure, and to examine the specific mutations present in individual clones, DNA sequences spanning the double-stranded DNA break site were aligned to a PCR-amplified DNA sequence from UCLA1 cells electroporated without any CRISPR reagents using the ICE tool (Synthego). Briefly, genomic DNA was isolated from clones using the Purelink genomic DNA mini kit (Invitrogen), and the region of *OPA1* spanning the double-stranded DNA break site was amplified using Q5 Hot Start HiFi Polymerase (New England Biolabs Inc.) and PCR primers XJY1361 and XJY1362 (**Supplementary Table 3-3**). Thermocycler conditions were as follows: 30 seconds at 98°C; 30 cycles of 8 seconds at 98°C, 30 seconds at 60°C, and 30s at 72°C; and 2 min at 72°C. PCR products were Sanger sequenced using primer XJY1361 (**Supplementary Table 3-3**). *OPA1* heterozygous (E10) and homozygous mutant (D9) ESC lines were identified from clones with insertions or deletions that produced early stop codons on one or both alleles.

3.4.3 Generation of the line 1iDOA-CR via CRISPR-Cas9 correction of 1iDOA's *OPA1* mutation

Prior to nucleofection, 1iDOA iPSCs (see section 2.3.2) were dissociated to a single cell suspension using Accutase (Stemcell Technologies), counted using Trypan blue exclusion (Gibco), and resuspended at a concentration of 25,000 cells/μL in P3 Primary Cell Nucleofector solution (Lonza). While cells were prepared, RNPs composed of 200 pmol of the synthetic sgRNA, "sgRNA_exon19" (Synthego) (**Supplementary Table 3-2**), and 120 pmol of Cas9 protein (Macrolabs) were made and incubated at room temperature for 10-15 min. Alt-R HDR donor oligo (Integrated DNA Technologies) (**Supplementary Table 3-2**) was added to the RNP at a final concentration of 3μM along with $5x10^5$ 1iDOA iPSCs in P3 Primary Cell Nucleofector solution (Lonza). The single-cell suspension was then nucleofected in a Lonza Nucleofector cuvette (S) using electroporation program CA-137 on a Lonza 4D-nucleofector with X-unit (Lonza). Cells were cultured as a population in mTeSR plus, 1% Antibiotic-Antimycotic, and 10% Clone R. Clone R was removed after 24 hours. To facilitate clonal selection, the population of edited cells was subsequently plated in Matrigel-coated 96 well plates at a density of 1 cell/well in mTeSR plus, 1% Antibiotic-Antimycotic, and 10% Clone R. Clone R was removed once colonies reached ~20 cells. Once single cell-derived colonies were large enough, they were expanded for two passages, after which genomic DNA was isolated using the Purelink genomic DNA mini kit (Invitrogen). The region surrounding the G insertion mutation in exon 19 of *OPA1* was amplified via PCR using Hot Star Taq DNA Polymerase (Qiagen) and the PCR primers XJY1366 and XJY1367 (**Supplementary Table 3-3**). Thermocycler conditions were as follows: 15 min at 95°C; 37 cycles of 30 seconds at 94°C, 30s at 57°C, and 1 min at 72°C; and 10 min at 72°C. PCR products of clones were Sanger sequenced with primers XJY1424-2 and XJY1367 (**Supplementary Table 3-3**) and aligned to a non-edited UCLA1 control sequence using the ICE tool (Synthego) to screen

for correctly edited clones. One clone was identified (1iDOA-CR) and correction was further verified by restriction digest.

3.4.4 Restriction digest/PCR

Genomic DNA was isolated using the Purelink genomic DNA mini kit (Invitrogen). 200 ng of genomic DNA was amplified via PCR for the region surrounding the G insertion mutation in exon 19 of *OPA1* using primers XJY1366 and XJY1367 (**Supplementary Table 3-3**) and Hot Star Taq DNA Polymerase reagents (Qiagen). Thermocycler conditions were as follows: 15 min at 95°C; 35 cycles of 30 seconds at 94°C, 30s at 57°C, and 1 min at 72°C; and 10 min at 72°C. PCR products were incubated with or without BstBI (New England Biolabs Inc.), resolved on an agarose gel containing Ethidium Bromide, and visualized using a FluorChem® Q, MultiImage III (Alpha Innotech).

3.4.5 Karyotype

Standard G-band karyotyping was performed by Cedars Sinai as previously described[170] to verify that 1iDOA-CR iPSCs displayed a 46, XY normal male karyotype.

3.4.6 Immunofluorescent staining and imaging

PSCs grown on Matrigel-coated NUNC™ Thermanox™ 13 mm plastic coverslips (ThermoFisher Scientific) were fixed in 4% paraformaldehyde for 2 minutes and then incubated in blocking solution (0.1% TritonX-100, 2% donkey serum, 10% FBS in DMEM). Coverslips were stained with primary antibodies, followed by secondary antibodies and DAPI diluted in blocking solution (**Supplementary Table 3-4**). All incubations were for one hour at room temperature, and staining periods were followed by three, 5 minute washes in PBS with 0.1% Tween 20. Coverslips were mounted on glass slides (Fisher Scientific) with mounting media (Fluro-Gel, Electron Microscopy

Sciences) and imaged using the Olympus Flowview FV1000 (upright) scanning laser confocal microscope with Plan-APO objectives.

3.4.7 Western blot

PSCs were washed twice in cold PBS and then incubated with lysis buffer (10uM HEPES, 10uM KCL, 0.1% NP40, 1.3M MgCl) supplemented with 1X protease and phosphatase inhibitor (Cell Signaling) for 2 minutes at room temperature. Cells were manually dissociated and rotated at 4°C in lysis buffer with inhibitor for 15 minutes. Cells were pelleted at 13,000 rpm at 4°C for 10 minutes, after which supernatant was collected. The supernatant's protein concentration was quantified using the micro BCA protein assay kit (ThermoFisher Scientific). 20 μg of protein lysate per sample was loaded on a 4-12% NuPAGE gel (Invitrogen), and gels were run and transferred to a PVDF membrane (Millipore) under reducing conditions according to the NuPAGE technical guide (Invitrogen). Membranes were stained with primary and secondary antibodies (**Supplementary Table 3-4**) according to the Near Infrared Western Blot Detection technical guide (LI-COR Biosciences). Blots were imaged using the Odyssey® CLx Imaging System (LI-COR Biosciences).

3.4.8 Super resolution imaging

PSCs were grown on #1.5 coverslips (Warner Instruments) coated with Matrigel (Corning) and then fixed and stained as described under "Immunofluorescent staining and imaging," section 3.4.6. Cells were incubated with the primary antibodies TOM20 and OPA1 and then with DAPI and secondary antibodies (**Supplementary Table 3-4**). Coverslips were mounted on glass slides using Vectashield mounting medium (Vectorlabs), and the coverslip/slide was sealed with CoverGrip (Biotium). Super resolution images were captured using the General Electric DeltaVision OMX microscope for structure illumination microscopy (SIM) with a PlanApoN

60x/1.42 NA oil objective (Olympus). Immersion oil with a refractive index of 1.516 was used. Images were acquired in 3D-SIM mode using a Z-spacing of 0.125 µm and reconstructed using Softworx software (GE Healthcare).

3.4.9 Seahorse XF analysis

Human PSCs were dissociated using Accutase and seeded at a density of 10,000 cells/well (H9, UCLA1, E10, and D9) or 15,000 cells/well (H9, 1iDOA, 2iDOA, 1iDOA-CR) in a Matrigel coated-Seahorse XF96 well plate (Agilent) in 60 µL of mTeSR plus supplemented with 1% Antibiotic Antimycotic and 10 µM Y-27632. The outer 36 wells of the plate were filled with PBS for the duration of the assay to minimize evaporative effects across the plate. The oxygen consumption rate (OCR) and the extracellular acidification rate (ECAR) were measured in parallel in a Seahorse XF96 Extracellular Flux Analyzer (Agilent) the following day when cells were approximately 80% confluent. Approximately 1 hour prior to analysis, cellular media was changed to XF assay media (unbuffered DMEM supplemented with 10 mM glucose, 2 mM glutamine, 1 mM pyruvate, and 5 mM HEPES) and the plate was incubated at 37°C, without CO_2. Compounds were injected sequentially throughout the assay via injection ports A-D. Final concentrations of injected compounds included: 2 µM oligomycin (Port A), 0.5 µM (Port B) and 0.9 µM (Port C) FCCP, and 2 µM antimycin A and 2 µM rotenone (Port D). Upon assay completion, the plate was washed with PBS and fixed with 4% PFA. Nuclei were stained with 10 ng/mL of Hoescht 33342 (ThermoFisher) and counted with an Operetta High-Content Imaging System (PerkinElmer). Rate measurements were normalized to the number of Hoechst-positive nuclei stained before analysis. Data was analyzed using the Seahorse Wave Desktop software (Agilent) and exported to Microsoft Excel and GraphPad Prism #9.4.1 for analysis. ATP production rates were calculated as previously described[186,187].

3.4.10 Statistical analysis

Data was analyzed using GraphPad Prism #9.4.1 software. Ordinary one-way ANOVA and Tukey's multiple comparisons tests were used for seahorse analyses. All error bars are presented as mean value ± SEM. * represents p≤0.05, ** p≤ 0.01, *** p≤ 0.001, and **** p≤0.0001.

3.5 Figures

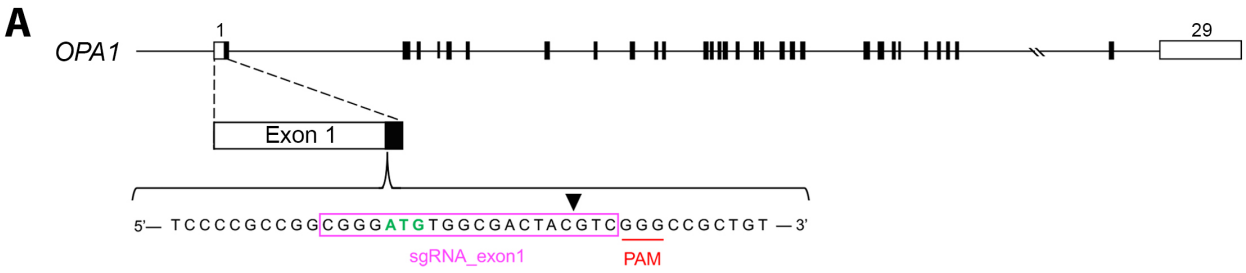
A
OPA1
1
29
Exon 1
5'— TCCCCGCCGGCGGGGATGTGGCGACTACGTCGGGCCGCTGT —3'
sgRNA_exon1
PAM

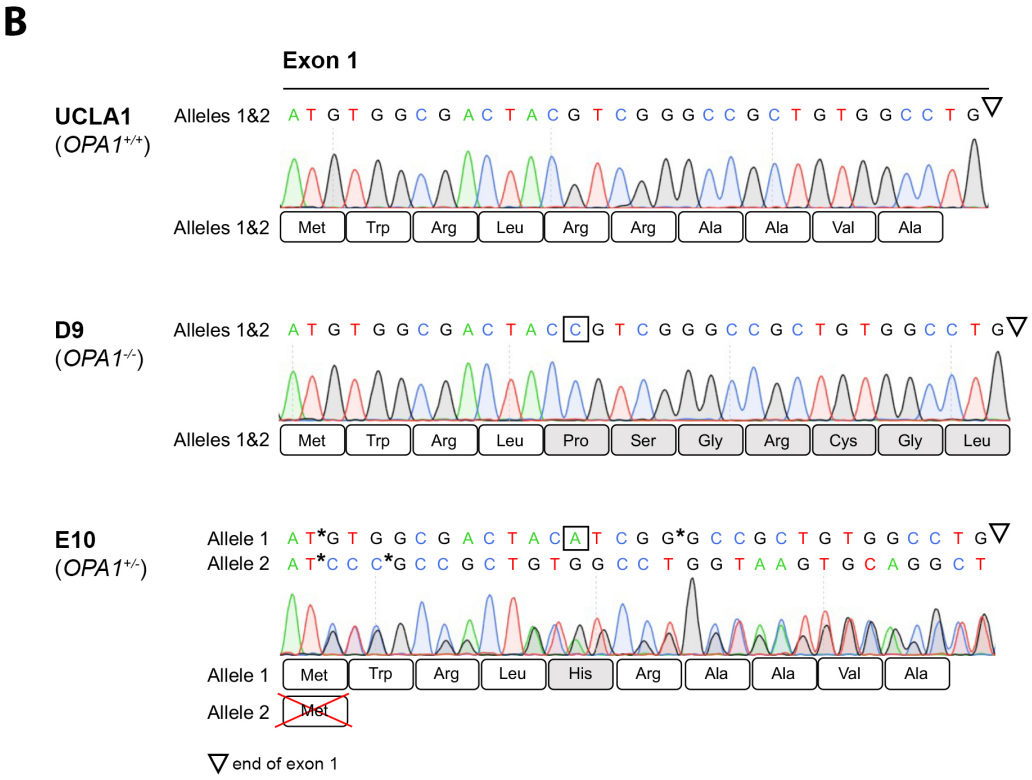
B
Exon 1
UCLA1
(OPA1+/+)
Alleles 1&2
Met Trp Arg Leu Arg Arg Ala Ala Val Ala
D9
(OPA1-/-)
Met Trp Arg Leu Pro Ser Gly Arg Cys Gly Leu
E10
(OPA1+/-)
Allele 1
Allele 2
Met Trp Arg Leu His Arg Ala Ala Val Ala
Met
end of exon 1

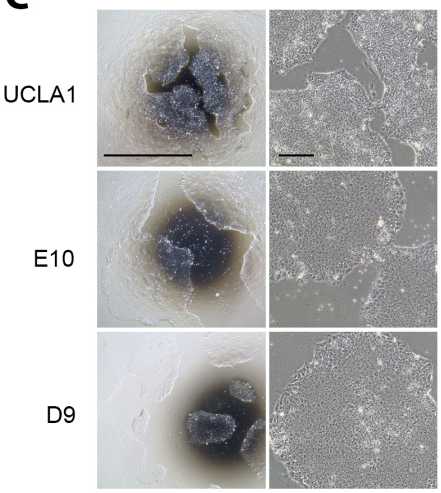
C
UCLA1
E10
D9

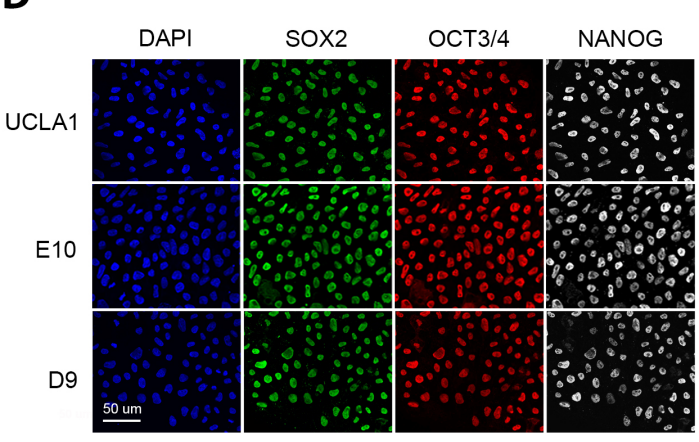
D
DAPI
SOX2
OCT3/4
NANOG
UCLA1
E10
D9
50 um

Figure 3- 1. Generation of *OPA1* heterozygous and homozygous mutant ESC lines isogenic to the *OPA1* WT ESC line, UCLA1

(A) Schematic of the *OPA1* gene, which contains 31 exons (1-29, 4b, and 5b). Exons or areas of exons that are white are untranslated, exons or areas of exons shaded in black are translated. Below the gene, the area of exon 1 that was edited to generate the heterozygous mutant line, E10, and homozygous mutant line, D9, is depicted. The sgRNA (boxed in pink) binds to the region containing the *OPA1* translation start site (bolded in green). Cas9 induces a double-stranded DNA break (indicated by a black triangle) upstream of the PAM site (underlined in red). sgRNA: single guide RNA; PAM: protospacer adjacent motif. **(B)** Alignment of Sanger sequencing traces of the CRISPR-Cas9 gene-edited UCLA1 ESC clones, D9 and E10, with the Sanger sequencing trace of nonedited, WT UCLA1 ESCs. Sequence traces begin at the *OPA1* translation start site in exon 1. The amino acid sequence of each allele is displayed under the sequence trace. Amino acids that differ from the WT protein sequence are shaded in grey. D9 has the same one base pair insertion (boxed) on both alleles that results in an early stop codon at the start of exon 2 (not shown). Consequently, both alleles are predicted to produce a truncated protein product of only 11 amino acids (see amino acids below the D9 trace). E10 has *OPA1* mutations on both alleles. Allele 1 has a G>A missense mutation (boxed), but is otherwise identical to the WT sequence. Allele 2 has a 16 base pair deletion (the bases between the asterisks on allele 1 are deleted) and a 3 base pair insertion [three Cs are inserted (between the asterisks on allele 2) in the same location the deletion occurred] that disrupts the ATG start codon. Allele 2 is predicted to not produce any OPA1 protein (indicated with a red X over the methionine start codon). **(C)** Brightfield images at two different magnifications demonstrate that E10 and D9 display normal pluripotent stem cell morphology comparable to the UCLA1 WT line from which they were derived. Scale bars: 500 μm, each applies to all panels in their respective column. **(D)** E10 and D9 express pluripotent stem cell markers SOX2, OCT3/4, and NANOG similarly to the WT ESC line, UCLA1. DAPI stains nuclei. Scale bar: 50 μm, all panels.

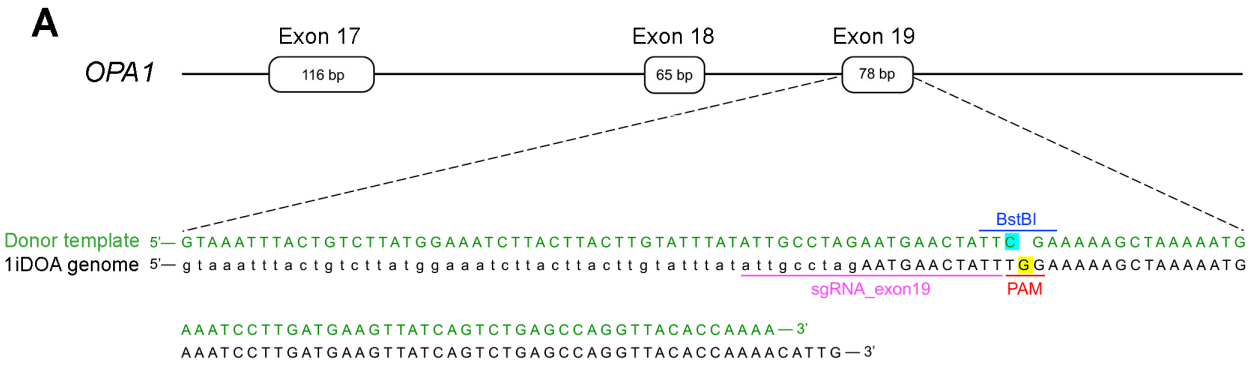
A
OPA1
Exon 17
116 bp
Exon 18
65 bp
Exon 19
78 bp
BstBI
Donor template 5'— GTAAATTTACTGTCTTATGGAAATCTTACTTACTTGTATTTATATTGCCTAGAATGAACTATTC GAAAAAGCTAAAAATG
1iDOA genome 5'— gtaaatttactgtcttatggaaatcttacttacttgtatttatattgcctagAATGAACTATTTGGAAAAAGCTAAAAATG
sgRNA_exon19
PAM
AAATCCTTGATGAAGTTATCAGTCTGAGCCAGGTTACACCAAAA— 3'
AAATCCTTGATGAAGTTATCAGTCTGAGCCAGGTTACACCAAAACATTG— 3'

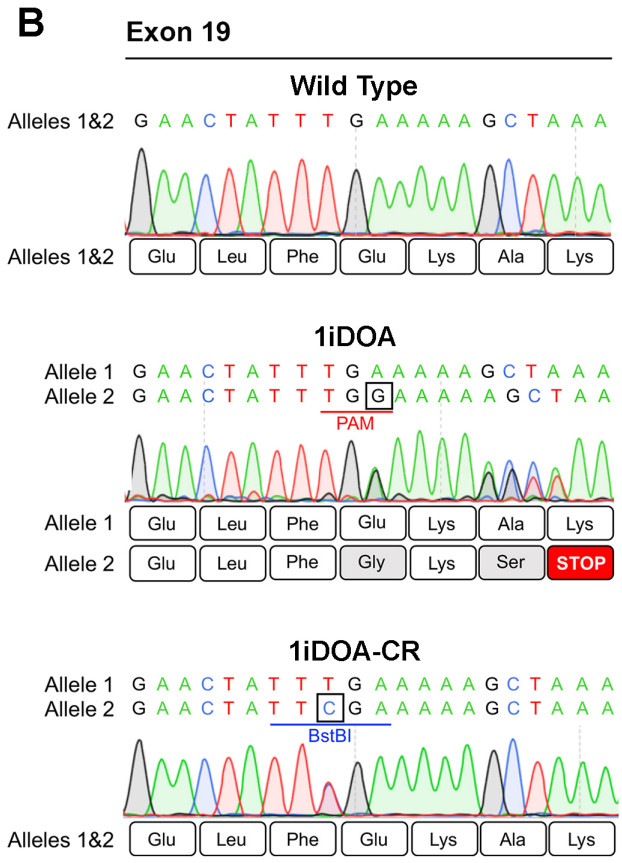
B
Exon 19
Wild Type
Alleles 1&2 G A A C T A T T T G A A A A A G C T A A A
Alleles 1&2 Glu Leu Phe Glu Lys Ala Lys
1iDOA
Allele 1 G A A C T A T T T G A A A A A G C T A A A
Allele 2 G A A C T A T T T G G A A A A A G C T A A A
PAM
Allele 1 Glu Leu Phe Glu Lys Ala Lys
Allele 2 Glu Leu Phe Gly Lys Ser STOP
1iDOA-CR
Allele 1 G A A C T A T T T G A A A A A G C T A A A
Allele 2 G A A C T A T T T C G A A A A A G C T A A A
BstBI
Alleles 1&2 Glu Leu Phe Glu Lys Ala Lys

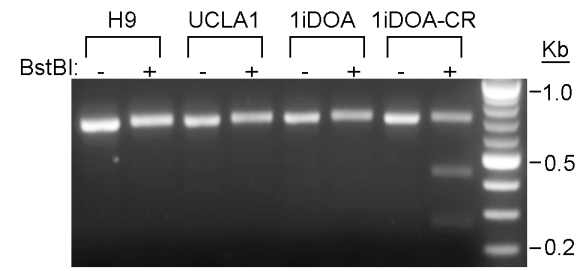
C
H9
UCLA1
1iDOA
1iDOA-CR
Kb
BstBI: - + - + - + - +
1.0
0.5
0.2

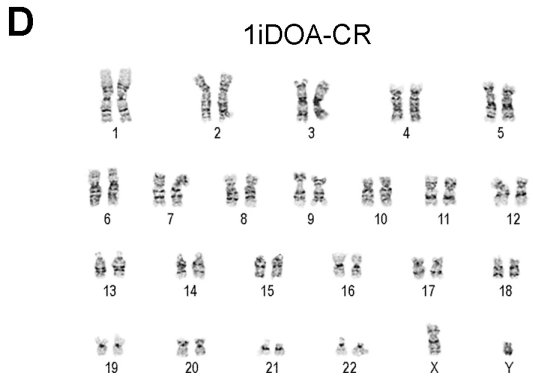
D
1iDOA-CR
1 2 3 4 5
6 7 8 9 10 11 12
13 14 15 16 17 18
19 20 21 22 X Y

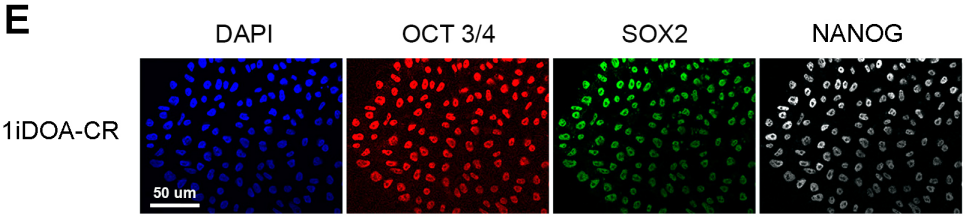
E
DAPI
OCT 3/4
SOX2
NANOG
1iDOA-CR
50 um

Figure 3- 2. Generation of the iPSC line 1iDOA-CR via CRISPR-Cas9-mediated correction of the *OPA1* c.1948dup mutation in 1iDOA iPSCs

(A) Schematic depicting the region of the allele in the 1iDOA genome that contains the G insertion *OPA1* mutation (highlighted in yellow) and was targeted for HDR. The sgRNA_exon19 (underlined in pink) and Cas9 will only target the *OPA1* mutant allele, as the mutation creates a PAM site unique to that allele. The 124 base pair ssODN acts as the HDR donor template (green text). It removes the G insertion and introduces a silent mutation (T>C, highlighted in blue). The silent mutation creates a novel BstBI restriction site (labeled in blue) on the edited allele that allows the correctly edited cell line, 1iDOA-CR, to be distinguished from other, *OPA1* WT cell lines. Uppercase letters in the 1iDOA genome (black text) indicate the sequence of *OPA1*'s exon 19 whereas lowercase letters represent intronic sequence. HDR: homology directed repair; ssODN: single-stranded oligodeoxynucleotide. **(B)** Sanger sequencing traces of WT control, 1iDOA, and 1iDOA-CR PSCs spanning the area of *OPA1*'s exon 19 that was targeted for correction. The DNA sequences of both alleles are displayed above the sequence trace, and the amino acid sequence of each allele is displayed under the sequence trace. Amino acids that differ from the WT protein sequence are shaded in grey. 1iDOA contains the heterozygous mutation c.1948dup. This G insertion mutation (boxed in black) changes the amino acid Glu to Gly, resulting in an early stop codon on one allele. As seen in the 1iDOA-CR sequence trace, successful CRISPR-Cas9 mediated HDR removes the G insertion mutation and introduces a silent T>C mutation (boxed in black). The silent mutation creates a BstBI restriction site (underlined in blue) that allows 1iDOA-CR to be distinguished from other WT lines. **(C)** Agarose gel demonstrating that the HDR corrected line, 1iDOA-CR, uniquely contains a BstBI restriction site. A 704 bp region spanning the area of *OPA1* targeted for HDR was amplified via PCR, and PCR products from the *OPA1* WT PSC lines H9 and UCLA1, the *OPA1* mutant line 1iDOA, and the HDR corrected line 1iDOA-CR, were digested with or without BstBI. Only 1iDOA-CR iPSCs incubated with BstBI display two additional bands at 436 and 268 bp, indicating it is the only cell line that contains the silent T>C

mutation that creates the novel BstBI restriction site. Some 704 bp product is still seen in the BstBI digested 1iDOA-CR lane because only one allele contains the restriction site. Bp: base pair(s). **(D)** 1iDOA-CR iPSCs display a normal karyotype after undergoing CRISPR-Cas9 gene editing. **(E)** Immunofluorescent staining of 1iDOA-CR iPSCs with OCT3/4, SOX2, and NANOG demonstrates that the cells' pluripotency was not altered after undergoing CRISPR-Cas9-mediated HDR. Scale bar, 50 μm.

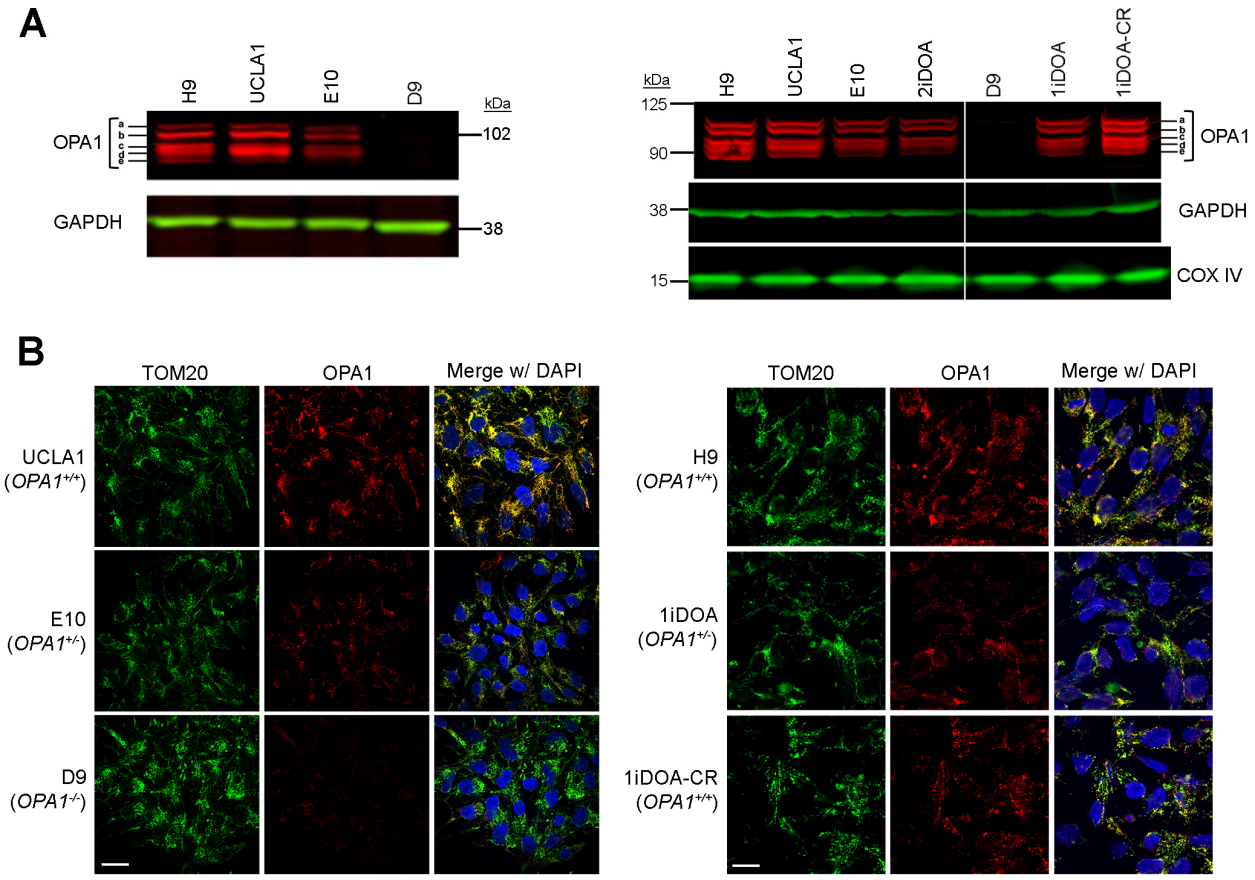

Figure 3- 3. OPA1 protein expression in WT and *OPA1* mutant PSCs

(A) Western blots comparing OPA1 protein levels between WT and *OPA1* mutant PSCs. Left: WT control ESC lines (H9 and UCLA1) express higher levels of OPA1 than *OPA1* heterozygous mutant ESCs (E10). *OPA1* homozygous mutant ESCs (D9) do not express OPA1. Right: Comparison of OPA1 and COX IV expression across the *OPA1* mutant ESC lines (E10 and D9), *OPA1* heterozygous mutant iPSC lines (1iDOA and 2iDOA) and 1iDOA CRISPR corrected iPSC line (1iDOA-CR). All PSC lines express long (a and b) and short (c-e) OPA1 protein isoforms (~80-100kDa). 20 μg of protein lysate was loaded per lane, and GAPDH was used as a loading control. **(B)** Representative images of WT and *OPA1* mutant PSC lines immunostained with an anti-OPA1 antibody. An anti-TOM20 antibody was used to visualize mitochondria and DAPI was used to visualize nuclei. Scale bars: 20 μm (all panels, left) and 10 μm (all panels, right).

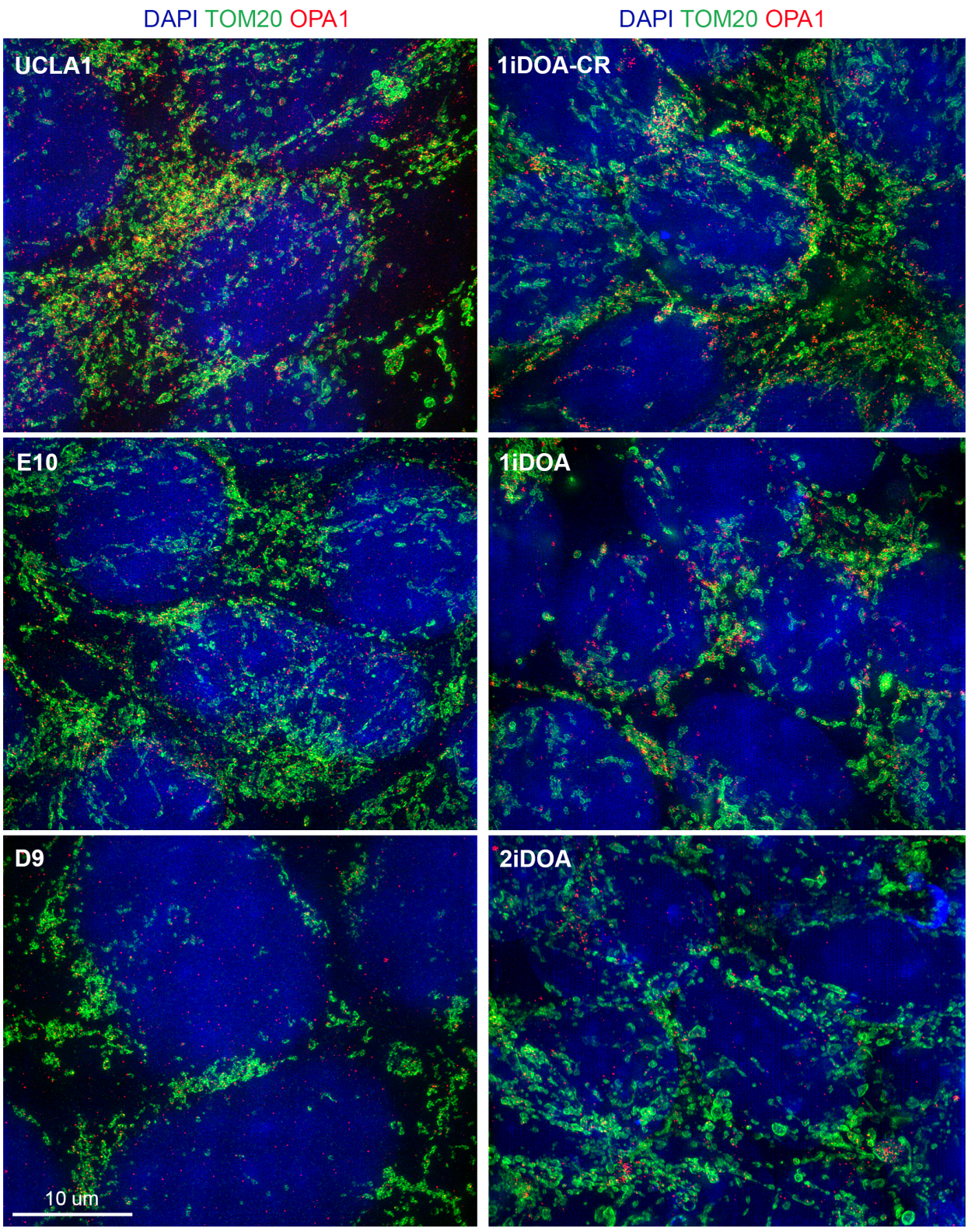
DAPI TOM20 OPA1
DAPI TOM20 OPA1
UCLA1
1iDOA-CR
E10
1iDOA
D9
2iDOA
10 um

Figure 3- 4. Super resolution imaging of WT and *OPA1* mutant PSC mitochondria

Mitochondrial morphology (as visualized via TOM20 staining) and OPA1 expression were examined across the isogenic WT (UCLA1), *OPA1* heterozygous mutant (E10), and *OPA1* homozygous mutant (D9) ESC lines (left column), and across the *OPA1* WT (1iDOA-CR) and heterozygous mutant (1iDOA and 2iDOA) iPSC lines (right column). 1iDOA and 1iDOA-CR are an isogenic pair. DAPI stains nuclei. Scale bar: 10 μm, all panels.

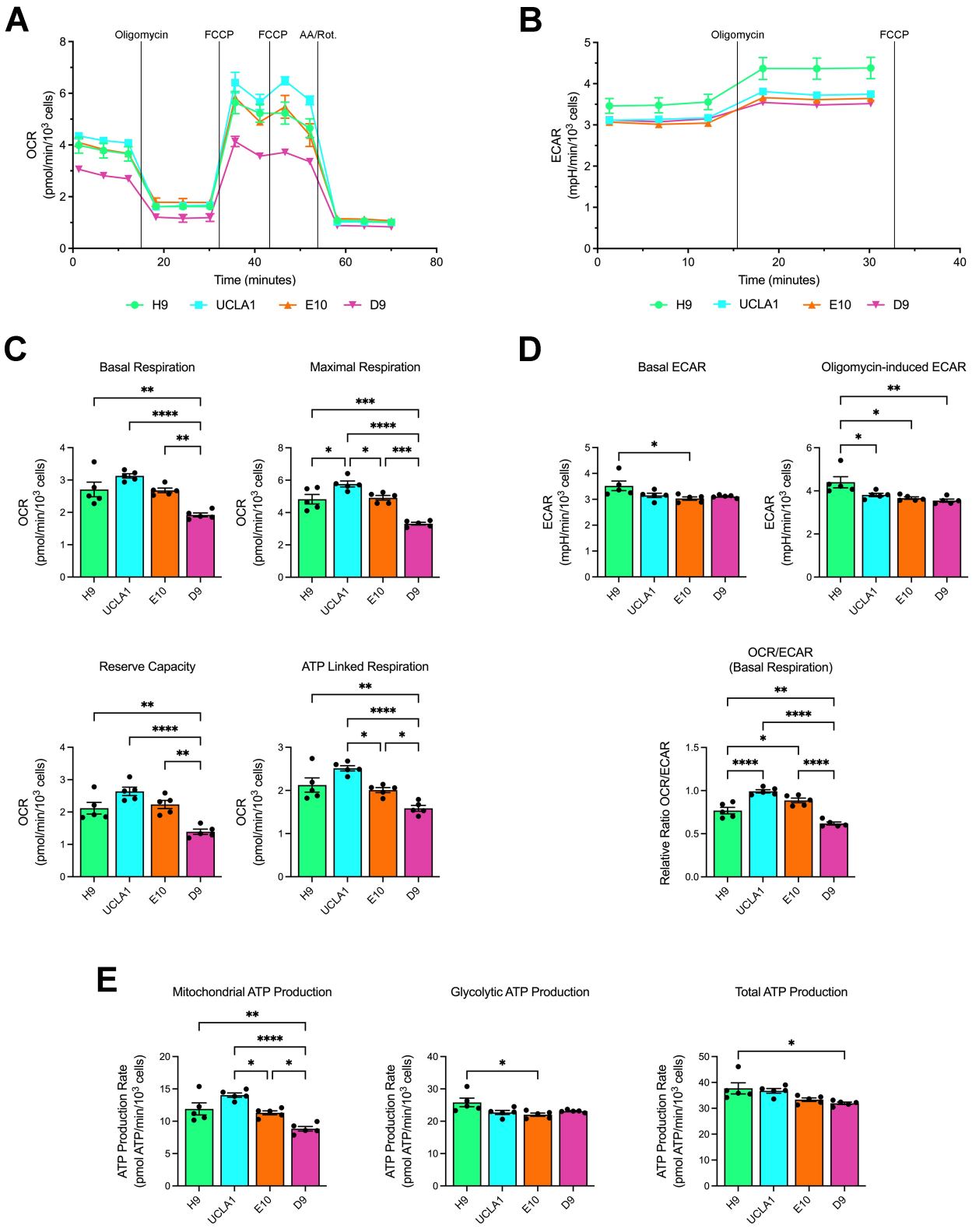
A
Oligomycin
FCCP
FCCP
AA/Rot.
OCR (pmol/min/10^3 cells)
Time (minutes)
H9
UCLA1
E10
D9
B
Oligomycin
FCCP
ECAR (mpH/min/10^3 cells)
Time (minutes)
H9
UCLA1
E10
D9
C
Basal Respiration
Maximal Respiration
Reserve Capacity
ATP Linked Respiration
OCR (pmol/min/10^3 cells)
D
Basal ECAR
Oligomycin-induced ECAR
ECAR (mpH/min/10^3 cells)
OCR/ECAR (Basal Respiration)
Relative Ratio OCR/ECAR
E
Mitochondrial ATP Production
Glycolytic ATP Production
Total ATP Production
ATP Production Rate (pmol ATP/min/10^3 cells)

Figure 3- 5. Bioenergetic characterization of the *OPA1* heterozygous and homozygous mutant ESCs, E10 and D9, and the *OPA1* WT ESCs, H9 and UCLA1

The OCR **(A)** and ECAR **(B)** of *OPA1* WT control ESCs (H9 and UCLA1), *OPA1* heterozygous mutant ESCs (E10), and *OPA1* homozygous mutant ESCs (D9) were assessed using a Seahorse XFe96 Analyzer. E10 and D9 are isogenic to UCLA1. Compounds [oligomycin, carbonyl cyanide p-trifluoro-methoxyphenyl hydrazone (FCCP), or antimycin A and rotenone] were injected into assay media at the designated time points (black, vertical lines). Analyses of bioenergetic profiles **(C-E)** demonstrate that E10 has lower OCR and mitochondrial ATP production than UCLA1, and that D9 has lower OCR and mitochondrial ATP production than E10. n=5 replicates per cell line. Bar graphs display each n as a separate data point, and data points are presented as mean values +/- SEM. * represents $p \leq 0.05$, ** $p \leq 0.01$, *** $p \leq 0.001$, and **** $p \leq 0.0001$. Rate measurements were normalized to the number of Hoechst-positive nuclei and displayed/10^3 cells. OCR: oxygen consumption rate; ECAR: extracellular acidification rate; AA/Rot.: antimycin A and rotenone.

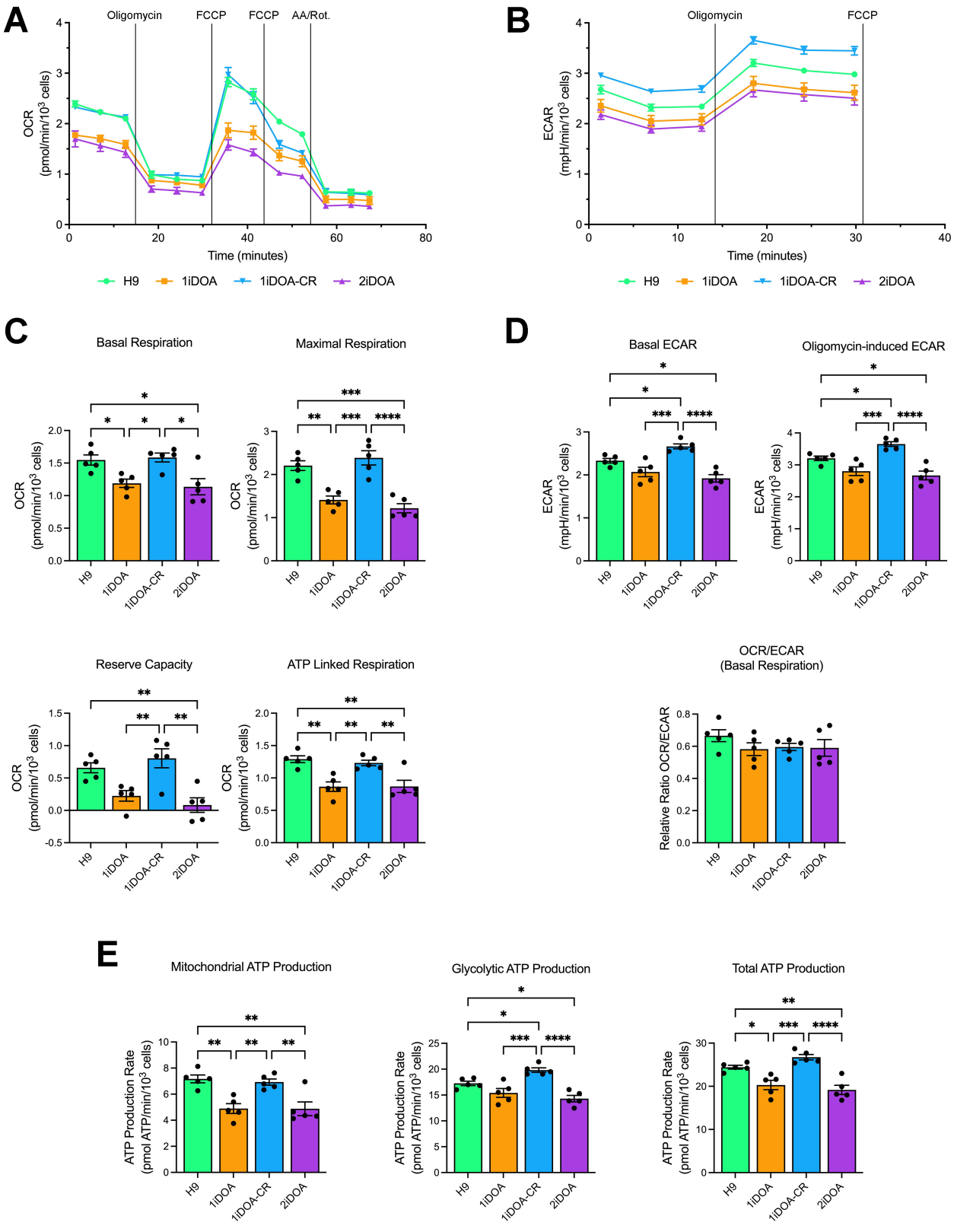
A
Oligomycin
FCCP
FCCP
AA/Rot.
OCR (pmol/min/10^3 cells)
Time (minutes)
H9
1iDOA
1iDOA-CR
2iDOA
B
Oligomycin
FCCP
ECAR (mpH/min/10^3 cells)
Time (minutes)
H9
1iDOA
1iDOA-CR
2iDOA
C
Basal Respiration
Maximal Respiration
Reserve Capacity
ATP Linked Respiration
OCR (pmol/min/10^3 cells)
H9
1iDOA
1iDOA-CR
2iDOA
D
Basal ECAR
Oligomycin-induced ECAR
OCR/ECAR (Basal Respiration)
ECAR (mpH/min/10^3 cells)
Relative Ratio OCR/ECAR
E
Mitochondrial ATP Production
Glycolytic ATP Production
Total ATP Production
ATP Production Rate (pmol ATP/min/10^3 cells)

Figure 3- 6. Bioenergetic characterization of the *OPA1* heterozygous mutant iPSCs, 1iDOA and 2iDOA, and the *OPA1* WT PSCs, H9 and 1iDOA-CR

The OCR **(A)** and ECAR **(B)** of *OPA1* WT control ESCs (H9), *OPA1* mutant iPSCs (1iDOA and 2iDOA), and 1iDOA CRISPR corrected iPSCs (1iDOA-CR) were assessed using a Seahorse XFe96 Analyzer. 1iDOA and 1iDOA-CR are isogenic. Compounds (oligomycin, FCCP, or antimycin A and rotenone) were injected into assay media at the designated time points (black, vertical lines). Analyses of bioenergetic profiles demonstrate that the *OPA1* heterozygous mutant iPSCs, 1iDOA and 2iDOA, have lower OCR, ECAR, and ATP production compared to the *OPA1* WT lines, H9 and 1iDOA-CR. n=5 replicates per cell line. Bar graphs display each n as a separate data point, and data points are presented as mean values +/- SEM. * represents $p \leq 0.05$, ** $p \leq 0.01$, *** $p \leq 0.001$, and **** $p \leq 0.0001$. Rate measurements were normalized to the number of Hoechst-positive nuclei and displayed/10^3 cells. OCR: oxygen consumption rate; ECAR: extracellular acidification rate; AA/Rot.: antimycin A and rotenone.

3.6 Supplementary Tables

Supplementary Table 3- 1. Pluripotent stem cell line *OPA1* genotypes

Line	*OPA1* Genotype	*OPA1* mutation(s)	Effect
UCLA1	+/+	c.473G>A(;)2274T>C p.(Ser158Asn)(;)(Ala758=)	Changes serine 158 to asparagine (both amino acids have polar, uncharged side chains); silent mutation—no effect
UCLA1-E10[#]	+[*]/-	c.[14G>A];[3_18delinsCCC] p.[Arg5His];[Met1?]	Changes arginine 5 to histidine (both amino acids are hydrophilic, basic, and have positively charged side chains); disrupts ATG start codon, no protein translated
UCLA1-D9[#]	-/-	c.[13dup];[13dup] p.[Arg5ProfsTer8];[Arg5ProfsTer8]	Truncated protein (11 vs 1,015 amino acids)
1iDOA	+/-	c.[1948dup];[1948=] p.[Glu650GlyfsTer4];[Glu650=]	Truncated protein (652 vs 1,015 amino acids)
1iDOA-CR	+/+	c.[1947T>C];[1947=] p.(Phe649=)	Silent mutation that inserts a novel BstBI restriction site
2iDOA	+/-	c.[1417_1418del];[1417_1418=] p.[Ile473PhefsTer12];[Ile473=]	Truncated protein (483 vs 1,015 amino acids)
H9	+/+	None reported	N/A

Base positions and amino acid positions refer to reference transcript NM_130837.3 and protein sequence NP_570850.2, respectively. +/+: *OPA1* WT; +/-: *OPA1* heterozygous mutant; -/-: *OPA1* homozygous mutant. *E10 has *OPA1* mutations on both alleles, but the c.14G>A missense mutation on allele 1 is not predicted to affect protein function. [#] Lines derived from UCLA1 also contain its indicated *OPA1* mutations in exons 4 and 21.

Supplementary Table 3- 2. CRISPR-related reagent sequences

Reagent	Sequence (5'→3')
sgRNA_exon1	CGGGATGTGGCGACTACGTC
sgRNA_exon19	ATTGCCTAGAATGAACTATT
Alt-R HDR Donor Oligo	/Alt-R-HDR1/G*T* AAA TTT ACT GTC TTA TGG AAA TCT TAC TTA CTT GTA TTT ATA TTG CCT AGA ATG AAC TAT TCG AAA AAG CTA AAA ATG AAA TCC TTG ATG AAG TTA TCA GTC TGA GCC AGG TTA CAC CAA* A* A/Alt-R-HDR2/

The ssODN included IDT's Alt-R HDR modifications [2 phosphorothioate (PS) bonds between the first and last three bases (indicated by *) and a proprietary end-blocking group on both the 5' and 3' end of ssODN (indicated by Alt-R-HDR#)]. The ssODN contains modifications from the 1iDOA genome highlighted in red (it introduces a silent T>C mutation and removes the G insertion mutation so there is only one G, as opposed to two, immediately following the silent mutation).

Supplementary Table 3- 3. PCR and Sequencing Primers

Location	Name	Direction, Use	Sequence
Exon 1	XJY1349	Forward, PCR	5'—TCTCGGCGCCTGCGTGACCT—3'
	XJY1350	Reverse, PCR and Sequencing	5'—TAAGCCCAGCCAGGGCTCCT—3'
	XJY1361	Forward, PCR and Sequencing	5'—TGGATTGCTCCAGTCCGTTC—3'
	XJY1362	Reverse, PCR	5'—GCAATGTACACATGGCGTGG—3'
Exon 19	XJY1366	Forward, PCR	5'—CACATAACGTGAACAAGTGT—3'
	XJY1424-2	Forward, Sequencing	5'—CCTCCCTTTGGTTATCTCTG—3'
	XJY1367	Reverse, PCR and Sequencing	5'—TACTCAGAATGGAGAACCTG—3'

Supplementary Table 3- 4. Antibodies and Dyes

	Antibody	Company	Catalog Number	Dilution	Use
Primary	SOX2 (Y-17)	Santa Cruz	sc17320	1:50	IF
	NANOG	abcam	ab21624	1:100	IF
	OCT3/4 (C-10)	Santa Cruz	sc5279	1:50	IF
	OPA1	BD Transduction Laboratories™	612606	1:100; 1:2,000	IF, SIM, WB
	GAPDH	Proteintech	10494-I-Ap	1:5,000	WB
	COX IV (3E11)	Cell Signaling	4850S	1:5,000	WB
	TOMM20	abcam	ab186734	1:150	IF, SIM
Secondary	Donkey α goat Alexa Fluor® 488	Invitrogen	A-11055	1:500	IF
	Donkey α rabbit Alexa Fluor® 488	Invitrogen	A-21206	1:500	SIM
	Donkey α mouse Alexa Fluor® 594	Invitrogen	A-21203	1:500	IF, SIM
	Donkey α rabbit Alexa Fluor® 647	Invitrogen	A-31573	1:500	IF
	IRDye® 800CW goat anti-rabbit IgG	LI-COR	925-32211	1:20,000	WB
	IRDye® 680RD goat anti-mouse IgG	LI-COR	925-68070	1:20,000	WB
Other	DAPI	Sigma	D9542	10 μg/mL final concentration	IF, SIM

IF: Immunofluorescence, WB: Western blot, SIM: Structure illumination microscopy.

CHAPTER 4

Initial characterizations of *OPA1* mutant human pluripotent stem cell-derived retinal organoids

4.1 Introduction

Inherited optic neuropathies (IONs), diseases that affect the optic nerve, have historically been difficult to study given the scarcity and inaccessibility of human retinal ganglion cells (RGCs), (the neurons that make up the optic nerve)[14-16]. One of the most common IONs, dominant optic atrophy (DOA), is caused by mutations in the nuclear gene *optic atrophy 1* (*OPA1*)[17,18]. OPA1 protein localizes to the inner mitochondrial membrane (IMM), where it has essential roles in mitochondrial fusion, cristae structure, mitochondrial DNA (mtDNA) maintenance, and bioenergetic output[65,91,188]. Surprisingly, despite *OPA1*'s ubiquitous expression, RGCs are the only cells impaired by *OPA1* mutations in most individuals and their degeneration causes progressive bilateral vision loss[39,52,53]. Given the scarcity and inaccessibility of RGCs, other human cell types have predominantly been used to study DOA[19-21]. However, findings in other cell types are unlikely to explain why RGCs are particularly prone to degenerate in an *OPA1* mutant background.

Our research efforts seek to address the significant unmet need for developing human RGC models of DOA. Fortunately, over the past decade, key advances in human pluripotent stem cell (hPSC) and gene editing technologies have enabled the creation of human, tissue-specific disease models[189]. The overarching goal of our research efforts is to use these advances to establish hPSC-derived RGC models of DOA that can then be used to 1. elucidate the molecular mechanisms underlying *OPA1* dysfunction-driven RGC degeneration and 2. screen drugs and therapies on the human cell type actually affected by DOA, the RGCs.

Two independent research groups previously published reports with a similar goal to generate RGCs from *OPA1* mutant hPSCs that could be used to better understand DOA

disease mechanisms[132,138]. The first study[138] primarily relied on N-[N-(3,5-difluorophenacetyl)-Lalanyl]-S-phenylglycine t-butyl ester (DAPT), a Notch inhibitor, to induce RGC development from neural rosettes or neurospheres[190]. Under these conditions, the ability of induced pluripotent stem cells (iPSCs) carrying the heterozygous *OPA1* mutation, NM_015560.2:c.2496 + 1G>T, to differentiate into neural cells was severely impaired, and no RGCs were produced unless the culture medium was supplemented with Noggin or 17B-estradiol[138]. A second, more recent study[132] used small molecules (including DAPT) to induce iPSCs to directly differentiate into RGCs in 2D culture[142]. Of the three *OPA1* heterozygous mutant iPSC lines assessed, two had mutations confirmed to cause haploinsufficiency and one had a missense mutation associated with DOA+. Notably, the *OPA1* mutations examined did not affect the iPSCs' ability to generate RGCs, and expression levels of RGC-associated markers such as ISLET-1 and BRN3B did not vary between wild-type (WT) and *OPA1* mutant cultures throughout the 42-day RGC-differentiation time window examined[132].

Contrary to these two studies, our lab has previously established a hPSC-based protocol (initially pioneered by Jason Meyer and colleagues[127,144]) to derive 3D retinal organoids (ROs), which spontaneously produce RGCs[164]. Compared to RGCs that develop from 2D cell monolayers or neurospheres[142,190], RGCs that develop in 3D ROs undergo a differentiation process that more faithfully recapitulates the developmental stages that occur *in vivo*[127]. Furthermore, unlike 2D cultures, ROs are spatially organized very similarly to human retinas. As cells acquire a RGC fate, they migrate away from the surface of the organoid and occupy a distinct inner layer, similar to the human RGC layer *in vivo*[147,148]. Additionally, as the RO is organized similarly to an *in vivo* retina, RGCs have a higher chance of interacting with some of the same cellular partners they would *in vivo*. Furthermore, it does not take longer to generate RGCs using 3D over 2D culture methods[146]. Therefore, using hPSC-to-3D RO differentiation protocols to generate RGCs is ideal because 1. the cells develop more similarly to how *in vivo* human retinal neurons develop, and 2. ROs allow a broader range of scientific questions to be probed than 2D differentiation protocols

do (i.e., if *OPA1* mutations affect the proportion of RGCs generated relative to other retinal cell types, if *OPA1* mutations affect the thickness of the RGC layer, etc.). Additionally, if assays are better suited for 2D RGC cultures, we have demonstrated that 3D ROs can be dissociated into 2D monolayers that contain high percentages of RGCs.

In Chapter 2, we derived iPSC lines from two DOA patients carrying distinct heterozygous *OPA1* mutations, and in Chapter 3, we generated isogenic *OPA1* mutant embryonic stem cell (ESC) lines using CRISPR-Cas9 genome editing. In this chapter, I describe how I modified the hPSC-derived RO differentiation protocol so that it could be used to compare ROs generated from hPSC lines with differing genetic backgrounds. Using this protocol, we proceed to show that all WT and *OPA1* heterozygous mutant pluripotent stem cell (PSC) lines examined are able to form ROs that contain RGCs. For the first time, I also report which OPA1 protein isoforms are expressed by the WT and *OPA1* mutant human ROs.

4.2 Results

4.2.1 Improving the standardization of embryoid bodies used to generate ROs

The protocol initially used to generate ROs in the lab was modified from a previously described protocol[127,143] (see section 4.4.2). Briefly, this process involves generating embryoid bodies (EBs) from PSCs and then directing the EBs towards a neural fate using various culture mediums. Under this protocol, the process of dissociating PSCs to generate starting material from which EBs can form yields a mixture of heterogeneously sized cell clusters (**Figure 4-1A**, Day 0). Unsurprisingly, the population of EBs formed from these PSC clusters is non-uniformly sized (**Figure 4-1A**, Day 1), and the population does not self-standardize over time (**Figure 4-1A**, Day 3). I refer to this method of EB formation as the “original method” (**Figure 4-1A**). Notably, although this differentiation procedure reproducibly generates ROs, the size and amount of ROs produced varies from batch to batch. The ratio of EBs to ROs is not 1:1—not every EB becomes an organoid, and organoids other than ROs are often generated. Around Days 21-25 in culture, our

lab separates putative ROs from cellular debris and from other "brain organoids". [We synonymously call ROs "optic vesicles" (OVs), and brain organoids "brain vesicles" (BVs)]. These putative ROs are monitored as they mature to ensure they are indeed ROs. True ROs are circular or oval-shaped, lack folds, and have an outer, transparent layer of neural epithelium that does not substantially thin with age, as well as an inner RGC layer that appears blue-grey in color under a light microscope (see **Figure 4-1A**, Day 36 and **B**, Day 35).

As our lab previously only used the WT H9 ESC line to generate ROs, the heterogeneity present throughout the stages of RO development was not a concern. However, to reliably compare RO development across a range of PSC lines, the differentiation procedure must be standardized at its earliest stages. Changes observed can then be more definitively attributed to genetic differences rather than differences inherent in the culture conditions.

Therefore, to more reliably determine the effects of *OPA1* mutations on retinal organoid development, I modified a protocol[191] previously used to generate brain (cortical) organoids that uses the AggreWell™ 800 plate (Stemcell Technologies, #344811) to generate uniformly sized EBs (see section 4.4.3). Each individual "aggrewell," in the plate houses 300 "microwells," and each microwell gives rise to a single EB. To generate EBs, PSCs are dissociated into a single-cell suspension that is aliquoted at a given density into the aggrewells. The plate is then centrifuged to evenly distribute the PSCs across the microwells (**Figure 4-1B**, Day 0). The following day, uniformly sized EBs are transferred from the aggrewell into a suspension culture dish (**Figure 4-1B**, Day 1). If EBs do not fuse to one another, the culture largely maintains uniformity as the EBs continue to grow (**Figure 4-1B**, Day 3). I refer to this method of EB formation as the "aggrewell method" (**Figure 4-1B**).

The total number of cells seeded per aggrewell is calculated by multiplying the number of cells one chooses to seed per individual microwell by 300 microwells. I tested seeding PSCs at densities of 1,000, 4,000, and 10,000 cells per microwell (data not shown). All yielded ROs, but we found a density of 4,000 cells per microwell to be optimal (**Figure 4-1B**). EBs that are too

small or large often do not yield cultures with high levels of neural induction during days 8-16 of the developmental protocol (see section 4.4.2).

Using the aggrewell method, we found that a higher proportion of putative ROs matured into true ROs than did using the original method (**Figure 4-1A**, Day 36 and **B**, Day 35). Although all variability is not eliminated—fusion of EBs can introduce differences in EB size and RO size still varies within each batch—using the aggrewell method significantly reduces the size variability seen in populations of EBs generated using the original method, and increases the probability that immature organoids that appear to be ROs are in fact ROs/will remain ROs. Notably, in addition to improving standardization, the aggrewell plate also improves throughput. The low percentage yield of organoids obtained per batch is a major limiting factor regarding the amount of experiments that can be performed and the statistical power to which they can be performed, and the aggrewell plate makes it easier to initially generate a larger number of EBs[192].

4.2.2 All *OPA1* WT and heterozygous mutant PSC lines tested generate ROs and produce RGCs

By seeding the same number of PSCs per microwell and then subjecting all cell lines to the same culture conditions, differences observed between the PSC lines throughout the RO development process can be more definitely attributed to a cell line's genetic background or particular *OPA1* mutation. To examine the ability of the *OPA1* WT and *OPA1* heterozygous mutant PSC lines generated in Chapters 2 and 3 to differentiate into ROs, we subjected them to both the original and aggrewell methods of EB formation, followed by the RO differentiation protocol described in section 4.4.2. Both WT and *OPA1* heterozygous mutant PSC lines were able to generate organoids from EBs generated using both the original and aggrewell methods. ROs generated by each WT and *OPA1* heterozygous mutant PSC line are depicted in **Figure 4-2**, and images were selected to demonstrate that all lines are able to generate ROs that have a transparent outer layer of neural epithelium and an inner RGC layer[164].

As mentioned in section 4.2.1, the yield of ROs generated from each differentiation procedure is often low. The aggrewell plate makes generating a larger number of EBs faster and simpler, allowing one to increase the number of ROs generated per protocol. Looking across multiple RO batches that were generated from seeding either 3,000 or 4,000 PSCs per microwell, the average number of ROs (partial or full) made per batch using H9, 1iDOA-CR, 1iDOA, and 2iDOA PSCs was 37.64 (n=10 experiments), 18.86 (n=8 experiments), 6.51 (n=8 experiments), and 29.17 (n=6 experiments), respectively, after normalizing RO counts to the number of aggrewells that were used to generate EBs. There was no blatant difference in the size or morphology of ROs generated from any of the PSC lines tested; each line produced a range of differently sized ROs and had varied rates of RO production from batch to batch.

Given our goal is to use *OPA1* mutant ROs to study DOA, a disease that causes the preferential loss of RGCs, we next investigated whether the *OPA1* heterozygous mutant PSC lines we generated were able to produce RGCs similarly to the WT ESC line, H9. Our lab has previously reported that H9-derived ROs are able to produce RGCs and shown that the RGCs comprise the inner cell layer of the RO[164]. As mentioned, like WT ROs, all *OPA1* heterozygous mutant ROs also appeared to have an inner RGC layer when visualized using brightfield microscopy (**Figure 4-2**). Notably, this layer was visible prior to Day 35 (**Figure 4-2**), although the peak period of RGC growth in ROs is between Days 35-55[164]. Immunofluorescent staining of sections taken from WT (H9) and *OPA1* heterozygous mutant (1iDOA and 2iDOA) ROs that were fixed on Day 36 of development confirmed that the inner layer of cells in *OPA1* heterozygous mutant ROs contained RGCs (ISLET-1 and NF145 positive cells) (**Figure 4-3**). Furthermore, as is the case in live human retinal tissue and in WT ROs, the RGCs in 1iDOA and 2iDOA ROs were largely retained to the inner organoid, where they form a distinct layer as previously mentioned (**Figure 4-3**).

Unfortunately, as ROs mature and produce later-stage retinal neurons such as photoreceptors, RGCs in the inner organoid begin to retract their processes and deteriorate, as

previously reported[150]. To prolong RGC life in culture, ROs can be dissociated and plated as 2D monolayer cultures. Interestingly, after optimizing RO dissociation and 2D culture conditions (cell density, culture medium), we observed that monolayers of dissociated RO cells contained a significant number of cells that stained positive for RGC markers (**Figure 4-4**). For instance, in **Figure 4-4A**, H9 and 1iDOA-CR WT ROs and 2iDOA *OPA1* heterozygous mutant ROs were dissociated on Day 31 and evenly plated as 2D monolayer cultures. After four days, both WT and *OPA1* heterozygous mutant cultures appeared healthy, as evidenced by a robust neurite network, and contained a visibly higher percentage of ISLET-1 and NF145 positive cells than was observed previously in non-dissociated RO cultures[164]. In **Figure 4-4B**, we demonstrate that WT and *OPA1* heterozygous mutant 2D RO cultures express a wide range of RGC markers in addition to ISLET-1 and NF145, including TUJ1, DCX, γ-SNCG, BRN3, RBPMS, NFASC, and NeuN. H9 and 1iDOA ROs were dissociated at Day 43, cultured for 24 days, and fixed on Day 67. 2iDOA ROs were dissociated on Day 49, cultured for 4 days similarly to the cells in **Figure 4-4A**, and fixed on Day 53. 1iDOA-CR ROs were dissociated on Day 52, cultured significantly longer for 46 days, and fixed on Day 98. Overall, these results show that WT and *OPA1* heterozygous mutant ROs can be dissociated over a period of more than 20 days and form a robust monolayer culture that supports RGC survival in a relatively short number of days. Notably, when WT and *OPA1* heterozygous mutant ROs are able to be dissociated similarly, are evenly plated, and are exposed to the same culture conditions, both are able to generate robust neuronal cultures that contain a considerable percentage of RGC marker-positive cells (**Figure 4-4B**, H9 and 1iDOA). If cells are not plated too sparsely, these monolayer cultures can be cultured for over 6 weeks (46 days was the longest culture condition depicted; **Figure 4-4B**, 1iDOA-CR). However, I have observed that the health of 2D monolayer cultures, of which RGCs are a part, does decline with age across all cell lines tested.

4.2.3 OPA1 protein isoforms expressed by WT and *OPA1* mutant ROs

After demonstrating that the H9, UCLA1, and 1iDOA-CR WT PSC lines as well as the E10, 1iDOA, and 2iDOA *OPA1* heterozygous mutant PSCs can all generate ROs, we sought to determine which OPA1 protein isoforms the ROs express. As discussed in section 1.4, the *OPA1* gene encodes eight mRNA isoforms, which are proteolytically processed into long (L-OPA1) and short (S-OPA1) protein isoforms. These OPA1 protein isoforms were previously thought to run as five bands on a polyacrylamide gel, named a-e[94]. However, a more recent study detected an additional sixth band, which was named d'[93]. Bands a and b correspond to L-OPA1 isoforms and bands c-e correspond to S-OPA1 isoforms[90,93]. Interestingly, I found that WT (H9 and 1iDOA-CR) and *OPA1* heterozygous mutant (1iDOA and 2iDOA) ROs (also called optic vesicles, or OVs) appear to express the same protein isoforms at the same ratios. All ROs predominantly expressed OPA1 isoforms corresponding to bands b, d', and e, and more weakly expressed OPA1 isoforms corresponding to bands a and d. H9 and 1iDOA-CR ROs also weakly expressed band c, but it is unclear from the images obtained whether 1iDOA and 2iDOA ROs also express band c (**Figure 4-5A,i** and **B**). The RO OPA1 expression pattern contrasts with that of WT and *OPA1* heterozygous mutant PSCs, which express five OPA1 protein isoforms at relatively equal ratios to one another (see section 3.2.3; **Figure 4-5A,ii**).

For clarification purposes, I have only ever detected five, as opposed to six, OPA1 isoform bands from PSC lysates. Under the same western blot experimental conditions, I detect six OPA1 isoform bands from RO lysates. In order to maintain the naming convention established by Wang *et al.*, I labeled the six bands expressed by ROs a-e, in which the band d' falls between bands d and e[93]. However, in comparing the PSC and RO samples' banding patterns, band d in **Figure 4-5A,ii** is likely band d' in **Figure 4-5A,i** and **B**. It is unclear whether band c in **Figure 4-5A,ii** is band c or d in **Figure 4-5A,i** and **B**.

As rodent retinal and brain tissues have been reported to express the same *Opa1* mRNA and protein isoforms[90,98], I also examined whether brain organoids (also called brain vesicles, or

BVs) expressed the same OPA1 protein isoforms as retinal organoids (also called optic vesicles, or OVs). Protein lysate was collected from 1iDOA-CR BVs on the same day lysate was collected from the OVs (Day 43). A partial OV and full BV that were part of the respective organoid populations analyzed in **Figure 4-5A,i** are depicted in **Figure 4-5A,iii**. Notably, to ensure OPA1 isoforms reflected a "pure" OV population, protein lysate was only collected from portions of OVs that maintained some transparency and clear structure as opposed to any OVs that had become overly opaque or lost their individual structure through fusion with other ROs (**Figure 4-5A,iii**, left**)**. BVs are morphologically different from OVs, containing multiple internal folds (**Figure 4-5A,iii**, right). In agreement with findings in rodents, the human OV and BV populations expressed the same OPA1 isoforms, and the expression levels of each isoform did not differ between the two organoid populations (**Figure 4-5A,i**).

Figure 4-5B confirms the findings of **Figure 4-5A,i,** and provides higher resolution results. Lanes 2 and 3 also demonstrate that the expression pattern of OPA1 isoforms remains the same, regardless of how protein lysate was collected (by manually or enzymatically dissociating ROs) (**Figure 4-5B,** Lanes 2 and 3).

Lastly, I examined whether the expression pattern of OPA1 protein isoforms was altered in WT or *OPA1* heterozygous mutant ROs when they were subjected to FCCP (carbonylcyanide-p-trifluoromethoxyphenylhydrazone), an uncoupler of oxidative phosphorylation. FCCP treatment causes cells to lose mitochondrial membrane potential and provides a scenario in which one can assess if cells' *OPA1* mutations compromise their ability to respond to stress. H9 WT and 2iDOA *OPA1* heterozygous mutant ROs were treated with or without 5 uM of FCCP for 20 minutes, after which protein lysates were harvested. FCCP treatment has been shown to increase the expression of S-OPA1 isoforms[95], but surprisingly, I saw no difference in the expression of L-OPA1 and S-OPA1 isoforms in WT or *OPA1* mutant ROs with or without FCCP treatment (**Figure 4-5B**, Lanes 3-6).

4.3 Discussion

Given our goal is to develop a human, *in vitro* disease model that mimics DOA pathogenesis *in vivo* as closely as possible, we thought it best to use human PSC-derived ROs. In contrast to 2D monolayer cultures, ROs have a RGC layer and maintain a spatial organization highly similar to the human retina. This provides an environment that more closely recapitulates what a RGC would experience *in vivo*. Furthermore, ROs produce a range of retinal cell types that can be assessed relative to RGCs in order to identify factors unique to RGCs that may explain their particular susceptibility to degeneration.

Because DOA is a heterogeneous disease, we generated a range of *OPA1* mutant PSC lines (see Chapters 2 and 3) that we needed to assess for their ability to differentiate into ROs that produced RGCs. To be able to effectively compare ROs generated from different PSC lines and more confidently attribute differences observed across the lines to the presence or absence of a particular *OPA1* mutation, I implemented a protocol that standardized differentiation conditions at one of the earliest differentiation stages (embryoid body formation). This protocol significantly improved the uniformity of EBs and made it easier to scale the organoid differentiation procedure; all WT and *OPA1* heterozygous mutant PSCs were able to form ROs. (We are in the process of assessing the *OPA1* homozygous mutant PSC line, D9's, differentiation capacity). However, we continue to see batch-to-batch variability in the number of ROs produced, both within and across individual PSC lines. This variability remains a challenge in the organoid field, and efforts to improve standardization/consistency, as well as scalability to account for low organoid yield, are essential for organoids to become trusted and widespread research tools.

We briefly mention our preliminary findings regarding the average number of ROs produced from H9, 1iDOA-CR, 1iDOA, and 2iDOA PSCs, which were normalized to the number of aggrewells used to generate the EBs. Interestingly, H9 WT PSCs generated twice as many ROs than 1iDOA-CR WT PSCs, highlighting the effect one's genetic background can have. However, 1iDOA-CR PSCs generated 2.9 times as many ROs compared to their isogenic *OPA1* mutant

line, 1iDOA, indicating that correcting the patient's *OPA1* mutation can provide a beneficial effect. Surprisingly, the *OPA1* mutant line 2iDOA generated a higher number of organoids than 1iDOA-CR PSCs (but a lower number than H9 PSCs), which is interesting given Patient 2 is mostly asymptomatic and Patient 1 presents with more severe DOA symptoms.

Given the high amount of variability observed when generating organoids, further assessment and meticulous quantification of multiple metrics will be required to make definitive conclusions regarding the differential ability of a PSC line to produce ROs and RGCs. When assessing two lines' abilities to generate ROs and RGCs, the PSCs must be the same confluency when dissociated, dissociated to a completely single-cell solution, and seeded into aggrewells at the same density. EB diameters and circumferences can be measured at different time points to assess differences in growth and developmental potential. ROs would also have to be counted and measured at multiple time points for a more complete characterization, as opposed to counting how many ROs each PSC line has generated in total at a single time point (as some ROs develop later and others degrade faster). Trends we have observed but need to further validate are that UCLA1 ESCs consistently form smaller EBs and that 1iDOA iPSCs consistently produce a lower number of ROs.

Apart from demonstrating here that *OPA1* heterozygous mutant ROs can produce RGCs in 2D and 3D cultures similarly to WT PSCs, we have performed some initial characterizations quantifying the number of RGC marker positive cells relative to total cells 1. in freshly dissociated 3D ROs using flow cytometry and 2. in immunostained 2D monolayer cultures of dissociated RO cells using microscopy assisted counting programs. It is our hope that further and repeated analyses will provide insights as to whether *OPA1* mutations cause less RGCs to be made initially (reports have suggested that DOA patients may be born with smaller optic nerves[46,47]), or cause mature RGCs to degenerate faster.

Lastly, after generating ROs from both WT and *OPA1* heterozygous mutant PSCs, we assessed which OPA1 protein isoforms they expressed. To our knowledge, this is the first report

on OPA1 protein expression in human retinal organoids. Similar to what we and others have shown in other cell types and tissues, the pattern of *OPA1* isoforms expressed by WT and *OPA1* mutant ROs did not differ[19,89]. Interestingly however, three isoforms corresponding to bands b, d', and e were more strongly expressed than other isoforms, indicating they may be used for specialized functions in retinal tissues. Furthermore, the expression of both long and short OPA1 isoforms is ideal for proper mitochondrial functioning[82,96].

However, in order to definitively rule out that an imbalance of OPA1 isoforms is responsible for *OPA1* mutation-mediated RGC degeneration, we must assess the expression of OPA1 protein in a purified population of human RGCs. To our knowledge, this has never been reported, presumably as it is extremely difficult to obtain a large enough number of RGCs from which to collect sufficient amounts of protein. Increasing RO yield and improving RGC purification procedures will help on this front.

Going forward, we intend to investigate mitochondrial processes known to be disrupted by *OPA1* mutations in both WT and *OPA1* mutant ROs and RGCs. Results from these assays will allow us to further characterize the hPSC-derived ROs' ability to serve as reliable models of DOA that could be used to test potential therapies and identify the underlying mechanisms responsible for DOA pathogenesis. Importantly, ROs may need to be cultured under conditions that more closely mimic the *in vivo* retinal environment for *OPA1* mutations to have a noticeable effect on RGC functioning. RGCs primarily use oxidative phosphorylation, and ROs are grown in culture medium that contains a high level of glucose (and promotes utilizing glycolysis). Culturing the ROs in galactose will force the cells to use oxidative phosphorylation over glycolysis and presumably heighten the effects any *OPA1* mutations have on mitochondrial structure and functioning.

4.4 Methods

4.4.1 Human pluripotent stem cell culture

Human PSCs were maintained in mTeSR plus medium (Stemcell Technologies, #100-0276) supplemented with 1% Antibiotic Antimycotic (AA) (Gibco/ThermoFisher Scientific, #15240062) on Matrigel (Corning) coated plates. PSCs were passaged by dissociating monolayer cells into a single-cell suspension with Accutase (Stemcell Technologies, #07920). Single cells were plated in mTeSR plus supplemented with 1% Antibiotic Antimycotic and 10 μM Y-27632 (Stemcell Technologies, #72302) for 24 hours, after which media was replaced with mTeSR plus with 1% Antibiotic Antimycotic. Media was changed no less frequently than every other day. PSCs were maintained at 37°C, 5% CO_2.

4.4.2 Human retinal organoid derivation

Using the "original method," at the start of the culture (Day 0), PSC cells (at 80–90% confluency) were detached from culture plates as previously described, with the following modifications[143]. Briefly, PSCs were incubated in Dispase (Stemcell Technologies, #07923) for 7 minutes at 37°C, 5% CO_2 and washed with DMEM/F12 (Gibco/ThermoFisher Scientific, #11330). Cells were then scraped using the tip of a serological pipette in a grid pattern in mTeSR1 (Stemcell Technologies, #85850) and manually lifted using a cell lifter (Corning, #3008). Cell clusters were titrated and then dispensed to culture dishes where they spontaneously form embryoid bodies (EBs). EBs are grown in the same culture media as described using the "aggrewell method", except mTeSR1 was used in place of mTeSR plus. Using the "aggrewell method," PSC cells (at 80–90% confluency) were enzymatically detached using Accutase, and the AggreWell™ 800 plate (Stemcell Technologies, #344811) was used to generate uniformly sized embryoid bodies (see section 4.4.3 for instructions pertaining through Day 6 of the RO derivation protocol). EBs generated using the original and aggrewell methods were treated the same way from Day 4 onwards to generate retinal organoids based on a previously described protocol[127,143] with noted

modifications. On Day 7, 10% FBS (Sigma-Aldrich, #12103C) was added to promote EB attachment to the culture wells. The following day, media with FBS was replaced with neural induction medium (NIM) supplemented with 27.5 ng/mL of BMP4 (R&D Systems, #314-BP-010). One-half of the media was replaced with fresh NIM every 2-3 days until Day 16. At Day 16, the visible neural rosettes formed from attached EBs were manually lifted, collected, and further cultured in suspension in Retinal Differentiation Medium (RDM) consisting of DMEM/F12=3:1 [half from DMEM/F12 (Gibco/ThermoFisher Scientific, #11330), half from DMEM (Gibco/ThermoFisher Scientific, #12430)], 1x B27 supplement (ThermoFisher, #1754044), 1x non-essential amino acids (NEAA; ThermoFisher, #11140050), and 1x Antibiotic Antimycotic (AA) (Gibco/ThermoFisher Scientific, #15240062). Around Day 20, translucent optic vesicle-like structures were manually separated from the rest of the suspension culture, collected, and cultured as retinal organoids in RDM. From Day 40, 10% FBS was added to the RDM and medium was changed every three days.

4.4.3 Generation of embryoid bodies using the AggreWell™ 800 plate

This protocol was modified from that of Yoon *et al*[191].

Note: I refer to the AggreWell™ 800 plate (Stemcell Technologies, #344811) as the aggrewell plate. I refer to the 24 individual wells that make up the aggrewell plate as individual aggrewells. Each individual aggrewell is composed of 300 microwells. The density of cells refers to the number of cells that are seeded per microwell. For instance, seeding 4,000 cells per microwell is equivalent to seeding $1.2x10^6$ cells per individual aggrewell (4,000 cells/microwell x 300 microwells/aggrewell).

Day 0

1. Pretreat each individual aggrewell of the AggreWell™ 800 plate that you will use that day with 500 μL of Anti-Adherence Rinsing Solution (Stemcell Technologies, #07010). Centrifuge the plate at 1300 g for 5 min.
2. Make sure bubbles are removed. Rinse each well with 2 mL of DMEM/F12.
3. Remove the DMEM/F12 and add 1 mL of mTeSR plus supplemented with 1% AA and 10 μM Y-27632 per aggrewell. Place the plate at 37°C, 5% CO_2.
4. Prepare a single-cell suspension of pluripotent stem cells (PSCs) for each cell line you will use. At the time of use, PSCs should be 80-90% confluent and cultured in mTeSR plus. Wash PSCs 2 times with Dulbecco's phosphate-buffered saline (DPBS) without calcium or magnesium (Gibco/ThermoFisher Scientific, #14190144).
5. Add 800 μL of Accutase per 6 well (6W) of PSCs and incubate for 4-7 min at 37°C, 5% CO_2.
6. Add cells to a 15 mL conical. Add 1-2 mL of mTeSR plus with 1% AA and 10 μM Y-27632 per well to rinse, then add to the same 15 mL conical.
7. Spin down cells at 200 g (~1000 rpm) for 2 min.
8. Resuspend the cell pellet in mTeSR plus with 1% AA and 10 μM Y-27632, and count.
9. Make a suspension of total cells needed per individual aggrewell in a total volume of 1 mL. Multiply 1. the volume of cells and 2. the media to add per number of aggrewells that you will seed, to make a common mix. For example, if one wishes to seed 4,000 total cells per microwell, there are 300 microwells per aggrewell, so one would need $1.2x10^6$ cells per 1 mL to plate into one aggrewell. If you are plating three aggrewells of one cell line, you would resuspend $3.6x10^6$ cells in 3 mL and seed 1 mL per aggrewell.
10. Add 1 mL of cells in mTeSR plus with 1% AA and 10 μM Y-27632 per aggrewell. The aggrewell plate should already have 1 mL of mTeSR plus with 1% AA and 10 μM Y-27632 in each aggrewell you will use, so there will be a 2 mL total volume per aggrewell upon addition of the cells.

11. Centrifuge the plate at 100 g for 3 min to evenly distribute the cells across the microwells.
12. Place the aggrewell plate at 37°C, 5% CO_2 for 24 hours.

Day 1

Note: Sometimes there is a fused strand of EBs in the well. This can be removed in step 5. Most EBs appear similar in size, except EBs at the edges of the aggrewell are often smaller.

1. Wet a wide tip P1000 to prevent EBs from sticking to the inside of the pipette tip.
2. Pipette media up and down gently with a wide tip P1000 to dislodge the embryoid bodies from the microwells. Add EBs to a 15 or 50 mL conical tube.
3. Wash the aggrewell with DMEM/F12 to collect all EBs. Repeat until all EBs are collected from the aggrewell.
4. Allow EBs from each aggrewell to sink by gravity in their respective conical tube. Aspirate supernatant as soon as EBs have all sank to minimize the time EBs can stick together at the bottom of the tube. Resuspend each aggrewell's EBs in 4-5 mL of media that consists of mTeSR plus and NIM at a 3:1 ratio and transfer them to a 60 mm suspension dish (Corning, #430589).

Neural Induction Medium (NIM) consists of DMEM/F12 supplemented with 1x N2 (ThermoFisher, #17502048), 1x NEAA, 1x AA, and 2 µg/ml of Heparin (ThermoFisher, H7482).

5. Remove aggregates of EBs that have fused together. Place dish(es) at 37°C, 5% CO_2 and shake to evenly distribute EBs to prevent them from fusing.

Day 2

1. Remove large aggregates.

2. Swirl EBs to the center of the dish and add them to an Eppendorf tube using a wide tip P1000.
3. Aspirate old medium and add new medium to the suspension dish consisting of mTeSR plus and NIM at a 1:1 ratio.
4. Let EBs sink by gravity. Aspirate supernatant and add back EBs to the 1:1 media in the suspension dish.

Day 3

1. Remove large aggregates.
2. Swirl EBs to the center of the dish and add them to an Eppendorf tube using a wide tip P1000.
3. Aspirate old medium and add new medium to the suspension dish consisting of mTeSR plus and NIM at a 1:3 ratio.
4. Let EBs sink by gravity. Aspirate supernatant and add back EBs to the 1:3 media in the suspension dish.

Day 4

1. Remove large aggregates.
2. Swirl EBs to the center of the dish and add them to an Eppendorf tube using a wide tip P1000.
3. Change media to full NIM.
5. Let EBs sink by gravity. Aspirate supernatant and add back EBs to the NIM in the suspension dish.

Day 6

Transfer EBs to tissue culture-treated 6-well plates (Corning, #3516) and replace media with NIM supplemented with 55ng/mL of BMP4[126].

From Day 7 forward, refer to section 4.4.2.

4.4.4 Embedding and sectioning of 3D ROs

ROs were fixed in 4% PFA on Day 36 for 30 min at 4°C. They were then incubated for 30 min to 1 hour in 30% sucrose in PBS and then in a solution composed of 30% sucrose in PBS and OCT at a 1:1 ratio for another 1 hour at 4°C. ROs were embedded in OCT, flash frozen, and sectioned via cryostat (ThermoFisher Scientific). Sections were stained as described in section 4.4.6.

4.4.5 2D dissociated retinal organoid cultures

Retinal organoids were manually cut into small pieces between Days 31 and 52 and then enzymatically dissociated with Trypsin (Sigma-Aldrich, #T9935) or Accumax (Stemcell Technologies, # 07921) into a single-cell suspension, incubated with DNAse for 10 minutes, and plated on glass coverslips coated with poly-D-lysine and laminin (Corning, #354087). Dissociated RO cells were cultured in BrainPhys neuronal medium (Stemcell Technologies, #05790) supplemented with SM1 (Stemcell Technologies, #05711) and N2 supplements (ThermoFisher, #17502048), 20 ng/mL of BDNF (PeproTech, #450-02), 20 ng/mL of GDNF (Stemcell Technologies, #78058), 1 mM of dibutyryl cyclic-AMP (Stemcell Technologies, #73882), and 200 nM of ascorbic acid (Stemcell Technologies, #72132). One-half medium was changed every three days until cells were fixed for analysis.

4.4.6 Immunofluorescent staining and imaging

Dissociated ROs were grown on poly-D-lysine and laminin-coated glass coverslips (Corning, #354087). Cells were fixed in 4% paraformaldehyde for 5 minutes and then incubated in blocking solution (0.1% TritonX-100, 2% donkey serum, 10% FBS in DMEM). Coverslips were stained with primary antibodies, followed by secondary antibodies and DAPI diluted in blocking solution (**Supplementary Table 4-1**). All incubations were for 1 hour at room temperature, and staining periods were followed by three, 5 minute washes in PBS with 0.1% Tween 20.

Coverslips were mounted on glass slides (Fisher Scientific, #12-550-25) with mounting media (Fluro-Gel; Electron Microscopy Sciences, #17985-10) and imaged using the Olympus Flowview FV1000 (upright or inverted) scanning laser confocal microscope with Plan-APO objectives.

4.4.7 Western blot

PSCs were washed twice in cold PBS and then incubated with lysis buffer (10uM HEPES, 10uM KCL, 0.1% NP40, 1.3M MgCl) supplemented with 1X protease and phosphatase inhibitor (Cell Signaling, #5872S) for 2 minutes at room temperature. Cells were manually dissociated from the culture plate and rotated at 4°C in the lysis buffer with inhibitor for 15 minutes. Organoids were either enzymatically dissociated as described in section 4.4.2 and resuspended in lysis buffer (10uM HEPES, 10uM KCL, 0.1% NP40, 1.3M MgCl) supplemented with 1X protease and phosphatase inhibitor or washed twice in cold PBS and then manually dissociated in an Eppendorf tube with 100 μL of lysis buffer supplemented with 1X protease and phosphatase inhibitor. Some organoids were incubated with 5μM of FCCP in HBSS without calcium or magnesium for 20 min prior to being manually dissociated. All organoid cells were then rotated at 4°C in lysis buffer with inhibitor for 15 minutes. Lysed PSCs and organoids were pelleted at 13,000 rpm at 4°C for 10 minutes, after which supernatant was collected. Each supernatant's protein concentration was quantified using the micro BCA protein assay kit (ThermoFisher Scientific, #23235). 15 μg of protein lysate per sample was loaded on an 8% Bolt Bis-Tris gel (Invitrogen, #NW00080BOX), and gels were run and transferred to PVDF membranes (Millipore) under reducing conditions according to the NuPAGE technical guide (Invitrogen). Membranes were stained with primary and secondary antibodies (**Supplementary Table 4-1**) according to the Near Infrared Western Blot Detection technical guide (LI-COR Biosciences), and blots were imaged using the Odyssey® CLx Imaging System (LI-COR Biosciences).

4.5 Figures

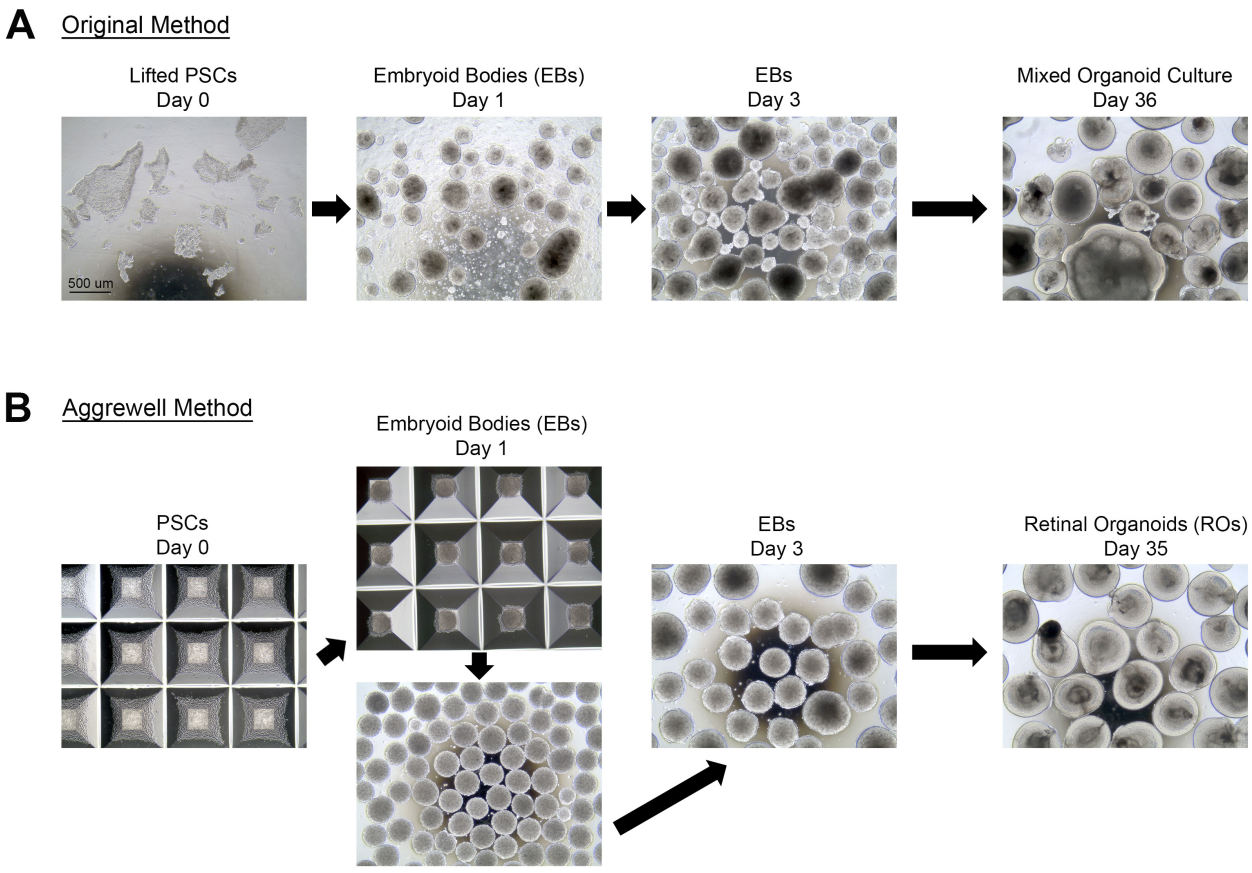

Figure 4- 1. Using the AggreWell™ 800 plate minimizes variability across EBs used to generate ROs

(A) Using the "original method," different-sized clusters of PSCs are used as starting material (Day 0), and consequentially, EBs are non-uniform in size (Day 1, Day 3). **(B)** Using the "aggrewell method," equal numbers of PSCs are evenly distributed across the microwells within an individual aggrewell (Day 0), producing more uniformly sized EBs (Day 1 and Day 3). After separating out putative ROs from lifted cultures around Days 21-23, more putative ROs generated using the aggrewell method (**B**, Day 35), as opposed to the original method (**A**, Day 36), mature into true ROs. Scale bar: 500 μm, all images.

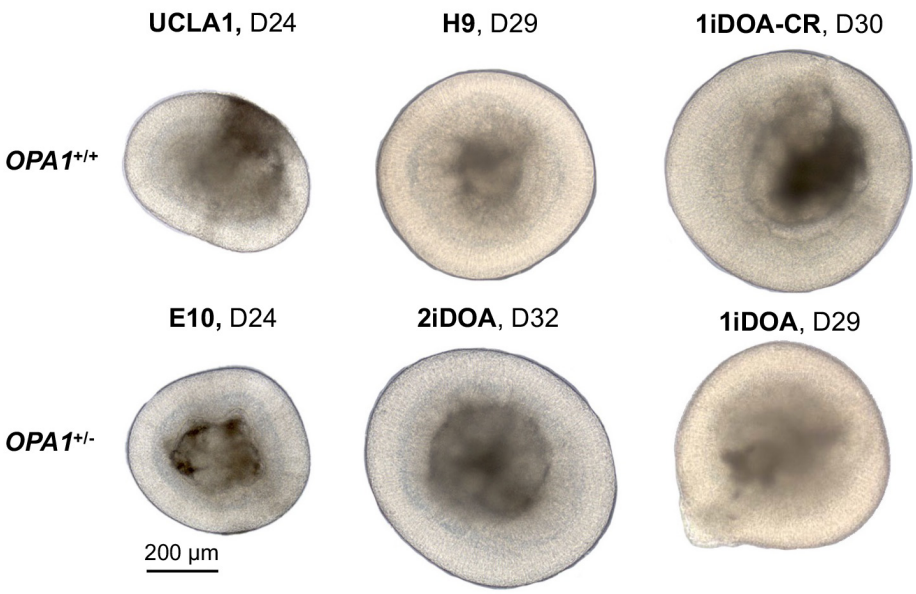

Figure 4- 2. All WT and *OPA1* heterozygous mutant PSC lines tested generate ROs

ROs can be generated from UCLA1, H9, and 1iDOA-CR *OPA1* WT (*OPA1*$^{+/+}$) PSCs and from E10, 1iDOA, and 2iDOA *OPA1* heterozygous mutant (*OPA1*$^{+/-}$) PSCs. ROs were imaged between culture Days 24-32 when the outer layer of neural epithelium is still transparent. The inner layer of cells is the RGC layer (blue-grey in color). UCLA1 and E10, and 1iDOA and 1iDOA-CR, are isogenic pairs. Scale bar: 200 μm, all organoids.

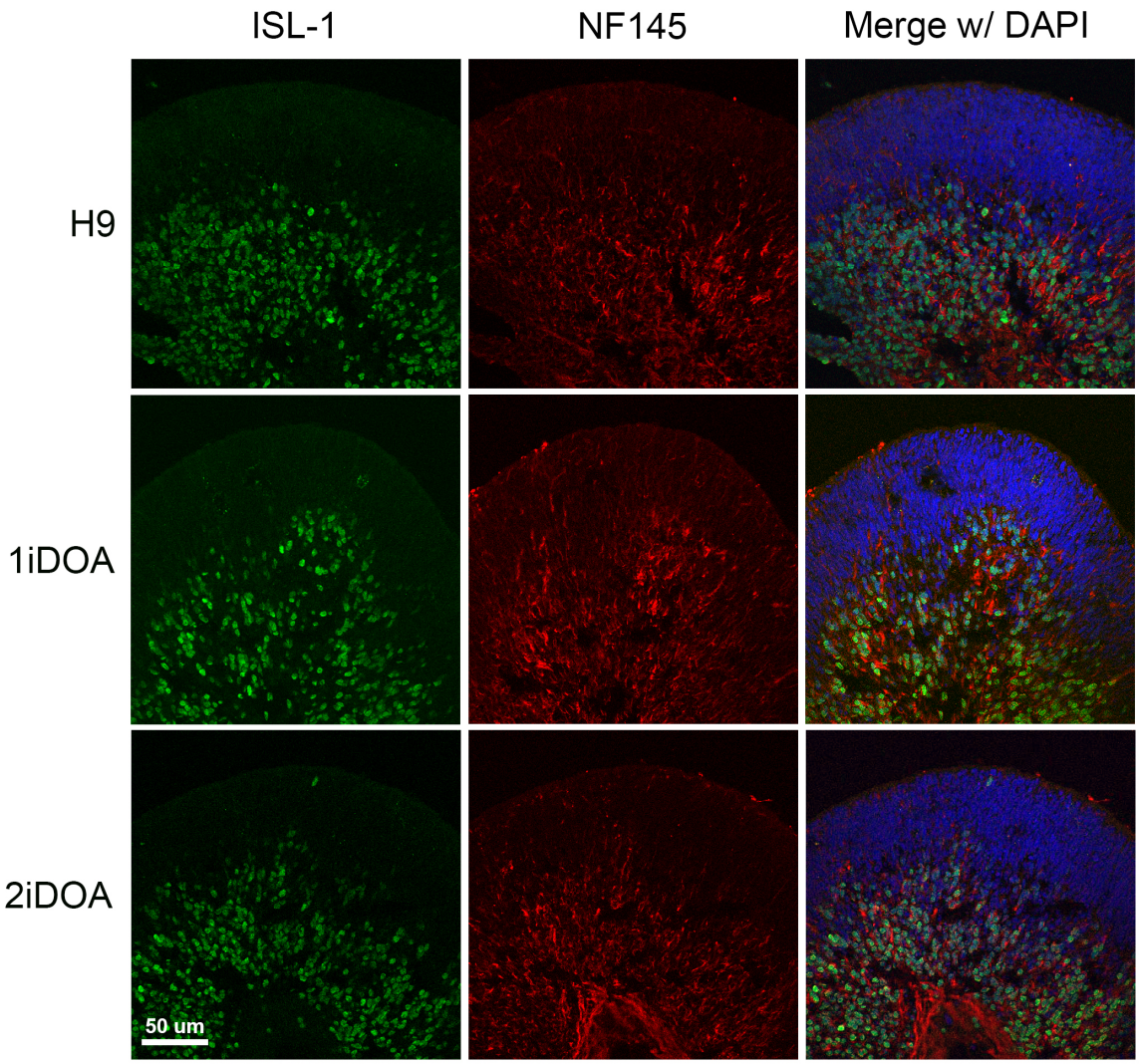

Figure 4- 3. *OPA1* heterozygous mutant iPSC-derived ROs produce RGCs that correctly localize to the RGC layer

ROs derived from *OPA1* heterozygous mutant iPSCs (1iDOA and 2iDOA) and WT H9 ESCs were fixed and embedded at Day 36 of development. Immunofluorescent staining of RO sections demonstrates that 1iDOA and 2iDOA ROs produce cells that express the RGC markers ISLET-1 and NF145 and that these cells occupy the inner layer of the RO similarly to what is observed in WT H9 ROs (top row). Scale bar: 50 μm, all panels.

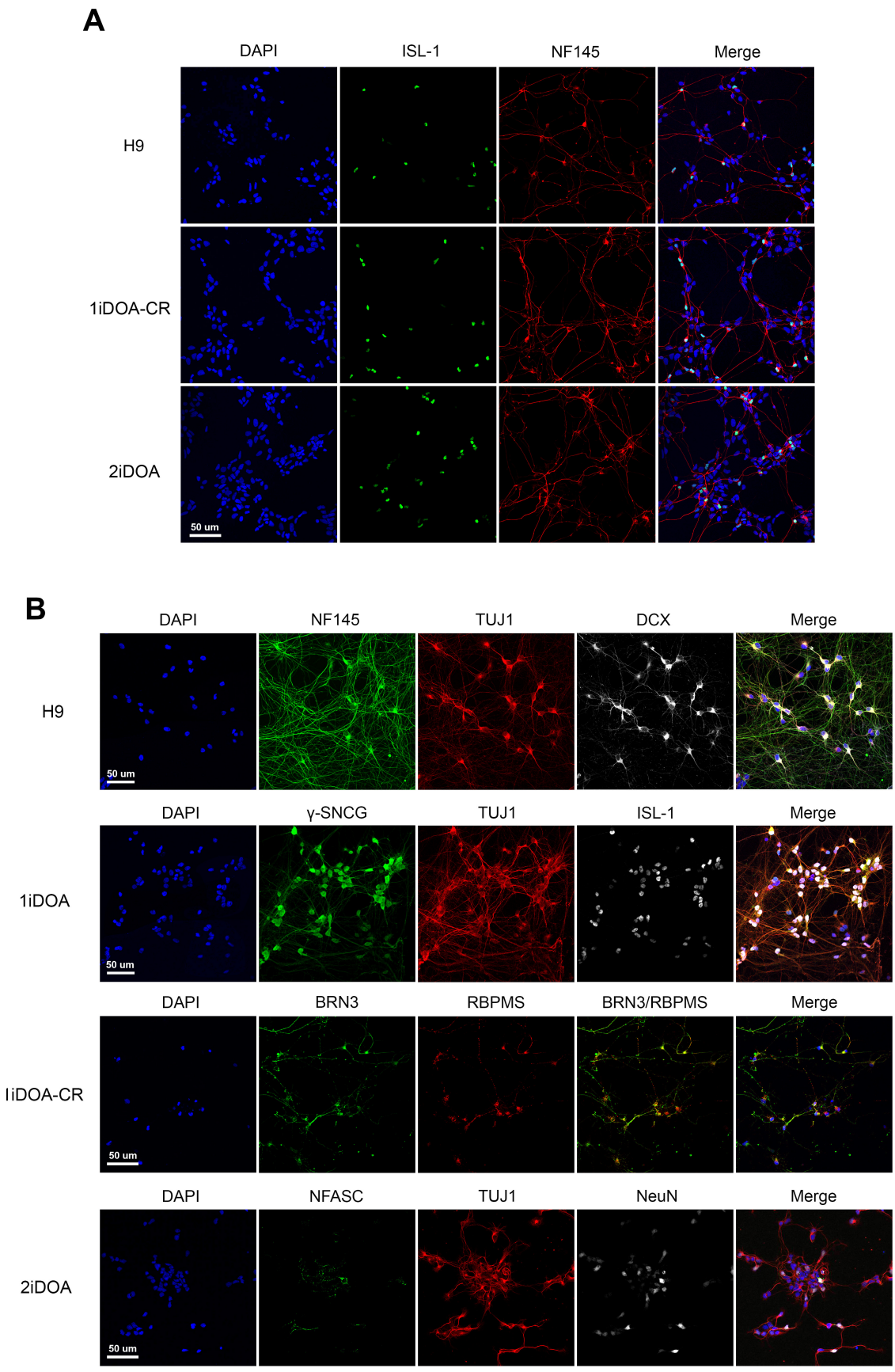
A
DAPI
ISL-1
NF145
Merge
H9
1iDOA-CR
2iDOA
50 um
B
DAPI
NF145
TUJ1
DCX
Merge
H9
50 um
DAPI
γ-SNCG
TUJ1
ISL-1
Merge
1iDOA
50 um
DAPI
BRN3
RBPMS
BRN3/RBPMS
Merge
1iDOA-CR
50 um
DAPI
NFASC
TUJ1
NeuN
Merge
2iDOA
50 um

Figure 4- 4. Dissociated RO cultures grown as 2D monolayers express RGC markers

(A) WT H9 and 1iDOA-CR ROs and *OPA1* heterozygous mutant 2iDOA ROs were dissociated on Day 31 with trypsin, cultured in BrainPhys for four days, and fixed on Day 35. Staining with the RGC-associated markers ISLET-1 and NF145 demonstrates that WT and *OPA1* mutant ROs of the same age produce RGCs that extend neurites. Scale bar: 50 μm, all panels. **(B)** H9 and 1iDOA ROs were dissociated in trypsin on Day 43, cultured for 24 days in BrainPhys, and fixed on Day 67. 1iDOA-CR ROs were dissociated in trypsin on Day 52, cultured for 46 days in BrainPhys, and fixed on Day 98. 2iDOA ROs were dissociated in Accumax on Day 49, cultured for four days in BrainPhys, and fixed on Day 53. Staining with the RGC-associated markers NF145, TUJ1, DCX, γ-SNCG, ISLET-1, BRN3, RBPMS, NFASC, and NeuN demonstrates that WT and *OPA1* mutant 2D RO cultures support RGC growth across a range of dissociation ages and time periods. Scale bars depicted apply to all panels in a given row.

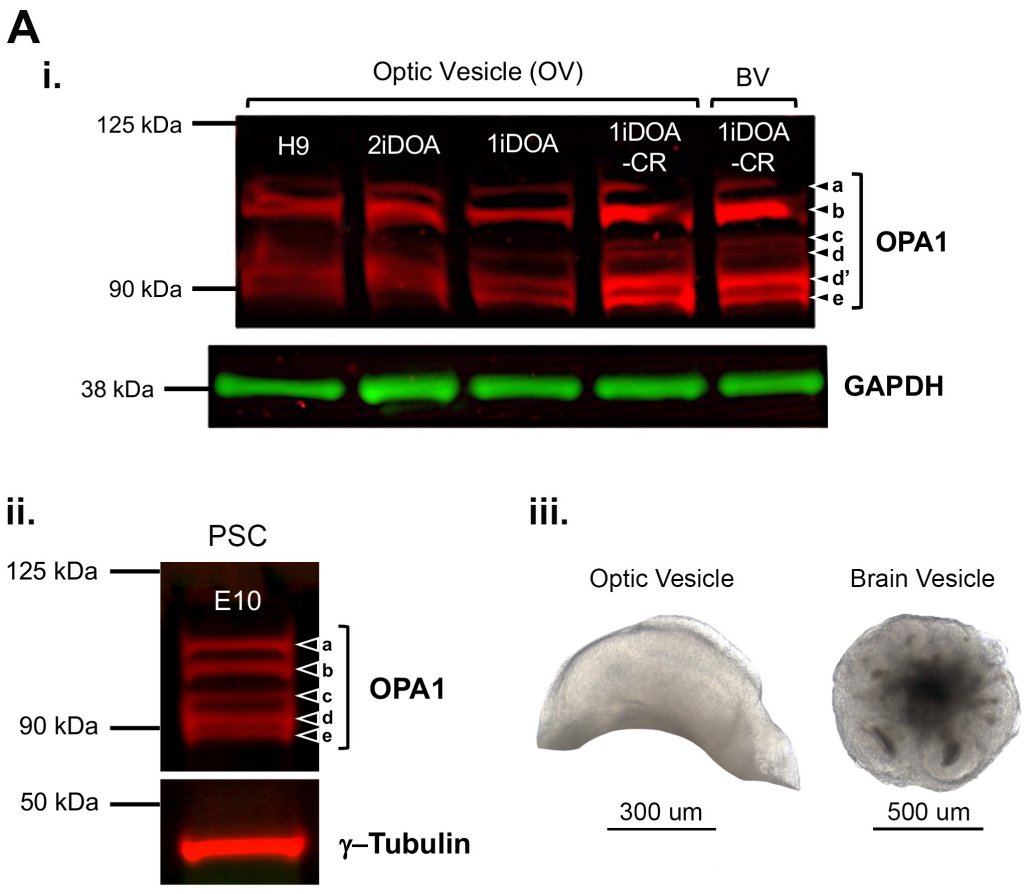
A
i.
Optic Vesicle (OV)
BV
125 kDa
H9
2iDOA
1iDOA
1iDOA -CR
1iDOA -CR
a
b
c
d
d'
e
OPA1
90 kDa
38 kDa
GAPDH
ii.
PSC
125 kDa
E10
OPA1
90 kDa
50 kDa
γ–Tubulin
iii.
Optic Vesicle
Brain Vesicle
300 um
500 um

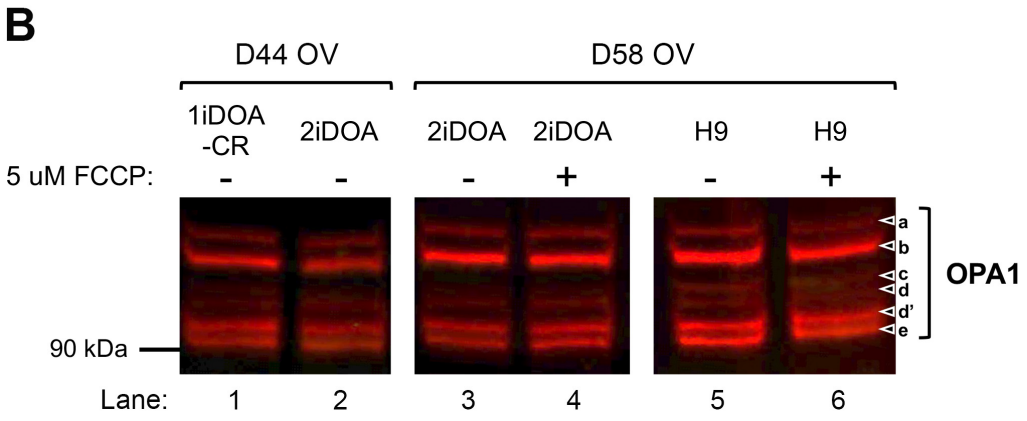
B
D44 OV
D58 OV
1iDOA -CR
2iDOA
2iDOA
2iDOA
H9
H9
5 uM FCCP:
-
-
-
+
-
+
a
b
c
d
d'
e
OPA1
90 kDa
Lane:
1
2
3
4
5
6

Figure 4- 5. OPA1 protein isoform expression in WT and *OPA1* heterozygous mutant ROs

(A) i. Western blot analysis demonstrates that OPA1 isoforms corresponding to bands b, d', and e are expressed more strongly than isoforms corresponding to bands a, c, and d in both WT and *OPA1* heterozygous mutant OVs. There is no difference in the OPA1 isoforms expressed by OVs and BVs. Protein lysate was collected from ROs, also called optic vesicles (OVs), and brain vesicles (BVs) at developmental Day 43. H9 and 1iDOA ROs were enzymatically dissociated and 2iDOA and 1iDOA-CR organoids were manually dissociated. GAPDH was used as a loading control. **ii.** Example gel excerpt demonstrating that unlike OVs, PSCs express isoforms a-e at relatively equal levels, regardless of *OPA1* mutation status. γ-Tubulin was used as a loading control. **iii.** Representative organoids from the 1iDOA-CR OV and BV populations that the protein lysates analyzed in **A,i.** were obtained from demonstrate that OVs and BVs are morphologically different. The OV and BV depicted were imaged on Day 43. **(B)** Protein lysate was collected from ROs on developmental Day 44 (Lanes 1 and 2) or Day 58 (Lanes 3-6). ROs were enzymatically (Lanes 1 and 2) or manually (Lanes 3-6) dissociated. Western blot analysis confirms the results of **A,i.** that WT and *OPA1* heterozygous mutant ROs predominantly express OPA1 isoforms corresponding to bands b, d', and e. The expression pattern of OPA1 isoforms was not affected whether ROs were enzymatically or manually dissociated (Lanes 2 and 3) or by 20 minutes of treatment with 5 μM FCCP (Lanes 3 and 4 and Lanes 5 and 6).

4.6 Supplementary Tables

Supplementary Table 4- 1. Antibodies and Dyes

	Antibody	Company	Catalog Number	Dilution	Use
Primary	ISLET	DSHB	39.4D5	1:10	IF
	NF145	Millipore	AB1987	1:200-1:500	IF
	Beta tubulin 3 (TUJ1)	Aves Labs	TUJ	1:500	IF
	DCX (E-6)	Santa Cruz	sc-271390	1:100	IF
	γ-SNCG	abcam	Ab55424	1:200	IF
	BRN3 (A-4)	Santa Cruz	sc-390780	1:100	IF
	RBPMS	phosphosolutions	1830-RBPMS	1:200	IF
	Neurofascin (A12/18)	Neuromab	RRID:AB_2282826	1:100	IF
	NeuN	abcam	ab177487	1:200	IF
	OPA1	BD Transduction Laboratories™	612606	1:100; 1:2,000	WB
	GAPDH	Proteintech	10494-I-Ap	1:5,000	WB
	γ-Tubulin (GTU-88)	Sigma	T6557	1:10,000	WB
Secondary	Donkey α mouse Alexa Fluor® 488	Invitrogen	A-21202	1:500	IF
	Donkey α rabbit Alexa Fluor® 488	Invitrogen	A-21206	1:500	IF
	Donkey α mouse Alexa Fluor® 594	Invitrogen	A-21203	1:500	IF

	Donkey α rabbit Alexa Fluor® 594	Invitrogen	A-21207	1:500	IF
	Donkey α chicken Alexa Fluor® 594	Invitrogen	A78951	1:500	IF
	Donkey α mouse Alexa Fluor® 647	Invitrogen	A-31571	1:500	IF
	Donkey α rabbit Alexa Fluor® 647	Invitrogen	A-31573	1:500	IF
	IRDye® 800CW goat anti-rabbit IgG	LI-COR	925-32211	1:20,000	WB
	IRDye® 680RD goat anti-mouse IgG	LI-COR	925-68070	1:20,000	WB
Other	DAPI	Sigma	D9542	10 μg/mL final concentration	IF

IF: Immunofluorescence, WB: Western blot.

CHAPTER 5

Concluding Remarks

Dominant optic atrophy (DOA) is the most prevalent inherited optic neuropathy[35,37-39]. The majority of DOA cases are caused by mutations in the gene *optic atrophy 1* (*OPA1*), a nuclear gene that encodes a dynamin-related GTPase that localizes to the mitochondria[17,18,45,104]. Puzzlingly, although *OPA1* is expressed ubiquitously, most individuals with *OPA1* mutations only exhibit mitochondrial dysfunction in their retinal ganglion cells (RGCs). This dysfunction ultimately causes RGCs to degenerate, resulting in progressive bilateral vision loss[41]. The field has attempted to understand why RGCs are particularly sensitive to *OPA1* mutations, but the inaccessibility and scarcity of human RGCs have historically limited such efforts[14-16]. My research has sought to overcome the shortage of accessible, live, human RGCs so that the pathological mechanisms underlying the *OPA1*-mutation-driven, RGC-specific degeneration observed in DOA patients can be elucidated. Using advances in gene editing and pluripotent stem cell (PSC) technology, I generated a range of *OPA1* mutant, human PSC lines that can be differentiated into 3D retinal organoids (ROs) that spontaneously produce human RGCs. I then characterized the molecular and mitochondrial phenotypes observed across the wild-type (WT) control and *OPA1* mutant cells at the PSC and RO/RGC levels to evaluate the PSC lines' abilities to serve as reliable, *in vitro*, DOA disease models.

To generate starting material from which human RGC models of DOA can ultimately be generated, we established induced pluripotent stem cell (iPSC) lines from DOA patients with distinct heterozygous *OPA1* mutations (1iDOA and 2iDOA) in Chapter 2, and we generated both *OPA1* heterozygous (E10) and homozygous (D9) loss-of-function human embryonic stem cell (ESC) lines using CRIPSR-Cas9 gene editing in Chapter 3. To generate an isogenic control iPSC line, we also corrected 1iDOA's mutation using CRISPR-Cas9-mediated homology

directed repair (HDR) (described in Chapter 3). As DOA is a genetically and phenotypically heterogeneous disease, a range of PSC lines containing distinct *OPA1* mutations is necessary to properly model and understand *OPA1*-driven DOA. Therefore, the PSC lines we generated have *OPA1* mutations that are distinct from those previously reported in the literature (**Supplementary Table 3-1**; section 1.5.1).

Using both ESC and iPSC lines for disease modeling is ideal, as they each confer their own specific advantages as a model. Editing a WT ESC cell line is advantageous in that all derivative lines will be isogenic to one another, or have the same genetic background. This allows phenotypic differences across the lines to be more confidently attributed to a line's *OPA1* mutation(s) (or lack thereof). Notably, editing WT ESCs also allowed us to generate *OPA1* mutant ESC lines that lack a functional OPA1 protein on either one or both alleles. To our knowledge, this is the first report of an *OPA1* homozygous loss-of-function human PSC line. On the other hand, iPSCs are advantageous to use for disease modeling as *in vitro* phenotypes of DOA patients' iPSC-derived RGCs can be directly compared back to the patients' ophthalmological data. Observations from a patient's cells *in vitro* and his/her clinical manifestations of disease can provide reciprocal insights that will aid in validating how closely our PSC-derived disease model recapitulates the DOA patient's disease symptoms and in informing which molecular mechanisms underlie these symptoms.

After generating a range of *OPA1* mutant PSC lines that can ultimately be used to generate human RGC models of DOA, we first confirmed that the *OPA1* heterozygous mutant PSC lines (E10, 1iDOA, and 2iDOA) had reduced levels of OPA1 protein, and that the *OPA1* homozygous mutant PSC line (D9) did not express OPA1 protein. Notably, all of the *OPA1* heterozygous mutant lines we generated have mutations that lead to an early stop codon on one allele, and are predicted to cause pathogenesis via haploinsufficiency. However, DOA can also be caused by *OPA1* missense mutations that lead to pathogenesis via a dominant negative mechanism; these mutations do not affect the total levels of OPA1 protein expressed.

Separately, as expected, correcting 1iDOA's *OPA1* mutation restored OPA1 protein expression to WT levels. Western blot analyses showed that both wild-type (WT) and *OPA1* heterozygous mutant PSCs expressed similar levels of the same five OPA1 protein isoforms, and that the five isoforms were expressed relatively equally to one another.

Next, we examined the mitochondrial morphology and cellular respiration of the *OPA1* WT and mutant PSC lines, as OPA1 plays important roles in mitochondrial fusion, cristae integrity, and bioenergetic function. Interestingly, structured illumination microscopy (SIM) revealed that D9 *OPA1* homozygous loss-of-function ESCs exhibited a more diffuse/less structured mitochondrial morphology than both WT PSCs and PSCs with *OPA1* haploinsufficiency. However, cellular respiration assays showed that both *OPA1* heterozygous and homozygous mutant PSCs had significantly lower oxygen consumption rates (OCR) and mitochondrial ATP production rates than isogenic WT control PSCs.

Interestingly, we did not observe any obvious growth defects across the different WT, *OPA1* heterozygous mutant, and *OPA1* homozygous mutant PSCs. As PSCs are known to predominantly use glycolysis (which is independent of the mitochondria) over oxidative phosphorylation (which is reliant on healthy mitochondria) as an energy source, *OPA1* mutations—and even a complete lack of OPA1 expression as seen in D9 PSCs—do not appear to affect the mitochondrial functioning of PSCs under normal culture conditions (glucose supplementation) in a significant enough way to affect growth (and in the case of E10 and D9 PSCs, the total ATP production rate).

Lastly, in Chapter 4, after modifying the human PSC-derived RO differentiation protocol so that it could be used to compare ROs generated from PSC lines with differing genetic backgrounds, I proceeded to show that all WT and *OPA1* heterozygous mutant PSC lines examined were able to form ROs that contain RGCs. Interestingly, as was observed between WT and *OPA1* haploinsufficient PSCs, WT and *OPA1* haploinsufficient PSC-derived ROs did not differ in the OPA1 isoforms they expressed. This suggests that *OPA1* haploinsufficient cells do not have

altered transcriptional or post-translational OPA1 processing, which would cause them to express a different ratio of long to short OPA1 isoforms from WT cells, and that functional differences observed between WT and *OPA1* heterozygous mutant cells may result from differences in total OPA1 protein expression levels. However, where WT and *OPA1* haploinsufficient PSCs expressed five OPA1 isoforms relatively equally to one another, WT and *OPA1* haploinsufficient ROs more strongly expressed three isoforms (corresponding to bands b, d', and e). This result indicates that these three isoforms may be used for specialized functions in retinal tissues.

Nonetheless, to definitively conclude that an imbalance of OPA1 isoforms is or is not responsible for the observed *OPA1*-mutation-mediated RGC degeneration in DOA patients, OPA1 protein expression must be measured in purified populations of WT and *OPA1* mutant human RGCs. Increasing RO yield and improving RGC purification procedures are necessary to obtain a large enough number of RGCs for this analysis to be possible.

Going forward, it will be interesting to assess if the observations we made regarding the mitochondrial morphology and functioning of WT and *OPA1* mutant PSCs are also observed in WT and *OPA1* mutant ROs and RGCs. As our results and the DOA patient population demonstrate, genetic background influences the severity of effects an *OPA1* mutation can have. Given the heterogeneity of genotypes and phenotypes present in the DOA population and DOA's incomplete penetrance, it is advisable to compare findings across many WT and *OPA1* mutant isogenic pairs, and for each pair of lines to have a different genetic background.

Additionally, as mentioned briefly, it will be important to also generate DOA disease models from *OPA1* heterozygous mutant PSC lines that contain missense, as opposed to nonsense, mutations to further elucidate how all *OPA1* mutations ultimately cause RGC degeneration. It will also likely be important to more closely mimic culture conditions that recapitulate the *in vivo* retinal environment for *OPA1* mutations to have a noticeable effect on RGC functioning. RGCs primarily use oxidative phosphorylation *in vivo*, but ROs are grown in culture medium containing a high level of glucose that promotes utilizing glycolysis. Culturing

the ROs in galactose would force the cells to use oxidative phosphorylation over glycolysis and presumably heighten the effects any *OPA1* mutations have on mitochondrial structure and functioning.

In summary, I generated multiple *OPA1* mutant, human PSC lines (including the first reported human *OPA1* homozygous loss-of-function PSC line, D9) that can be differentiated into ROs and RGCs *in vitro* to model DOA (D9's ability to differentiate into ROs and RGCs is still being assessed). I validated the cell lines' OPA1 expression at the PSC and RO levels, and demonstrated that WT and *OPA1* mutant ROs favor the expression of three specific OPA1 protein isoforms whereas WT and *OPA1* mutant PSCs uniformly express five OPA1 isoforms. Interestingly, although no changes in the growth of *OPA1* mutant PSCs were detected, *OPA1* mutant PSCs had reduced OCRs and mitochondrial ATP production rates compared to isogenic control PSCs. Research is ongoing to characterize functional differences between WT and *OPA1* mutant ROs and RGCs to better understand why *OPA1* mutations cause RGC-specific degeneration. Furthermore, *OPA1* mutant PSC-derived RGCs can be used to screen for and test therapies that could preserve or rescue vision in DOA patients and can provide important insights into other neurodegenerative diseases that share common metabolic deficiencies with DOA.

On a final note, I have focused on using the *OPA1* mutant PSC lines I generated to create *in vitro* models of DOA, but more broadly speaking, the lines can serve as valuable research tools to better understand *OPA1*'s role in development and disease. By differentiating the PSC lines into various tissue and cell types, one can investigate *OPA1*'s mitochondrial roles across a broad range of biomedical research topics related to metabolism, aging, and degenerative diseases.

REFERENCES

1 in *Webvision: The Organization of the Retina and Visual System* (eds H. Kolb, E. Fernandez, & R. Nelson) (University of Utah Health Sciences Center, 1995).

2 Edward, D. P. & Kaufman, L. M. Anatomy, development, and physiology of the visual system. *Pediatric Clinics of North America* **50**, 1-23 (2003). https://doi.org:https://doi.org/10.1016/S0031-3955(02)00132-3

3 Fuhrmann, S. in *Current Topics in Developmental Biology* Vol. 93 (eds Ross L. Cagan & Thomas A. Reh) 61-84 (Academic Press, 2010).

4 Graw, J. Eye development. *Curr Top Dev Biol* **90**, 343-386 (2010). https://doi.org:10.1016/s0070-2153(10)90010-0

5 Ptito, M., Bleau, M. & Bouskila, J. The Retina: A Window into the Brain. *Cells* **10**, 3269 (2021).

6 Zhang, K. Y. & Johnson, T. V. The internal limiting membrane: Roles in retinal development and implications for emerging ocular therapies. *Exp Eye Res* **206**, 108545 (2021). https://doi.org:10.1016/j.exer.2021.108545

7 Kobat, S. G. & Turgut, B. Importance of Müller Cells. *Beyoglu Eye J* **5**, 59-63 (2020). https://doi.org:10.14744/bej.2020.28290

8 Lazdinyte, S., Schorderet, D. F., Schaller, A., Valmaggia, C. & Todorova, M. G. Analysis of Inherited Optic Neuropathies. *Klin Monbl Augenheilkd* **236**, 451-461 (2019). https://doi.org:10.1055/a-0829-6828

9 Carelli, V., Morgia, C. L., Ross-Cisneros, F. N. & Sadun, A. A. Optic neuropathies: The tip of the neurodegeneration iceberg. *Human Molecular Genetics* **26**, R139-R150 (2017). https://doi.org:10.1093/hmg/ddx273

10 Liu, H. & Prokosch, V. Energy Metabolism in the Inner Retina in Health and Glaucoma. *Int J Mol Sci* **22** (2021). https://doi.org:10.3390/ijms22073689

11 Chen, H. & Chan, D. C. Critical dependence of neurons on mitochondrial dynamics. *Current Opinion in Cell Biology* **18**, 453-459 (2006). https://doi.org:10.1016/j.ceb.2006.06.004

12 Ito, Y. A. & Di Polo, A. Mitochondrial dynamics, transport, and quality control: A bottleneck for retinal ganglion cell viability in optic neuropathies. *Mitochondrion* **36**, 186-192 (2017). https://doi.org:10.1016/j.mito.2017.08.014

13 Wang, L., Dong, J., Cull, G., Fortune, B. & Cioffi, G. A. Varicosities of intraretinal ganglion cell axons in human and nonhuman primates. *Invest Ophthalmol Vis Sci* **44**, 2-9 (2003). https://doi.org:10.1167/iovs.02-0333

14 Mellough, C. B. *et al.* An integrated transcriptional analysis of the developing human retina. *Development (Cambridge)* (2019). https://doi.org:10.1242/dev.169474

15 Hoshino, A. *et al.* Molecular Anatomy of the Developing Human Retina. *Developmental Cell* **43**, 763-779.e764 (2017). https://doi.org:10.1016/j.devcel.2017.10.029

16 Hendrickson, A. Development of Retinal Layers in Prenatal Human Retina. *American Journal of Ophthalmology* (2016). https://doi.org:10.1016/j.ajo.2015.09.023

17 Alexander, C. *et al.* OPA1, encoding a dynamin-related GTPase, is mutated in autosomal dominant optic atrophy linked to chromosome 3q28. *Nature Genetics* **26**, 211-215 (2000). https://doi.org:10.1038/79944

18 Delettre, C. *et al.* Nuclear gene OPA1, encoding a mitochondrial dynamin-related protein, is mutated in dominant optic atrophy. *Nature Genetics* **26**, 207-210 (2000). https://doi.org:10.1038/79936

19 van Bergen, N. J. *et al.* Mitochondrial oxidative phosphorylation compensation may preserve vision in patients with OPA1-linked autosomal dominant optic atrophy. *PLoS ONE* **6** (2011). https://doi.org:10.1371/journal.pone.0021347

20 Olichon, A. *et al.* Loss of OPA1 perturbates the mitochondrial inner membrane structure and integrity, leading to cytochrome c release and apoptosis. *Journal of Biological Chemistry* (2003). https://doi.org:10.1074/jbc.C200677200

21 Lodi, R. *et al.* Deficit of in vivo mitochondrial ATP production in OPA1-related dominant optic atrophy. *Annals of Neurology* (2004). https://doi.org:10.1002/ana.20278

22 Williams, P. A., Morgan, J. E. & Votruba, M. Mouse models of dominant optic atrophy: What do they tell us about the pathophysiology of visual loss? *Vision Research* **51**, 229-234 (2011). https://doi.org:10.1016/j.visres.2010.08.031

23 White, K. E. *et al.* OPA1 deficiency associated with increased autophagy in retinal ganglion cells in a murine model of dominant optic atrophy. *Invest Ophthalmol Vis Sci* **50**, 2567-2571 (2009). https://doi.org:10.1167/iovs.08-2913

24 Alavi, M. V. *et al.* A splice site mutation in the murine Opa1 gene features pathology of autosomal dominant optic atrophy. *Brain* **130**, 1029-1042 (2007). https://doi.org:10.1093/brain/awm005

25 Alavi, M. V. *et al.* Subtle neurological and metabolic abnormalities in an Opa1 mouse model of autosomal dominant optic atrophy. *Exp Neurol* **220**, 404-409 (2009). https://doi.org:10.1016/j.expneurol.2009.09.026

26 Dayanithi, G. *et al.* Characterization of Ca2+ signalling in postnatal mouse retinal ganglion cells: involvement of OPA1 in Ca2+ clearance. *Ophthalmic Genet* **31**, 53-65 (2010). https://doi.org:10.3109/13816811003698117

27 Heiduschka, P. *et al.* Electrophysiological and histologic assessment of retinal ganglion cell fate in a mouse model for OPA1-associated autosomal dominant optic atrophy. *Invest Ophthalmol Vis Sci* **51**, 1424-1431 (2010). https://doi.org:10.1167/iovs.09-3606

28 Williams, P. A. *et al.* Opa1 is essential for retinal ganglion cell synaptic architecture and connectivity. *Brain* **135**, 493-505 (2012). https://doi.org:10.1093/brain/awr330

29 Williams, P. A., Morgan, J. E. & Votruba, M. Opa1 deficiency in a mouse model of dominant optic atrophy leads to retinal ganglion cell dendropathy. *Brain* **133**, 2942-2951 (2010). https://doi.org:10.1093/brain/awq218

30 Rahn, J. J., Stackley, K. D. & Chan, S. S. Opa1 is required for proper mitochondrial metabolism in early development. *PLoS One* **8**, e59218 (2013). https://doi.org:10.1371/journal.pone.0059218

31 Varanita, T. *et al.* The OPA1-dependent mitochondrial cristae remodeling pathway controls atrophic, apoptotic, and ischemic tissue damage. *Cell Metab* **21**, 834-844 (2015). https://doi.org:10.1016/j.cmet.2015.05.007

32 Chao de la Barca, J. M. *et al.* Targeted Metabolomics Reveals Early Dominant Optic Atrophy Signature in Optic Nerves of Opa1delTTAG/+ Mice. *Invest Ophthalmol Vis Sci* **58**, 812-820 (2017). https://doi.org:10.1167/iovs.16-21116

33 Cowan, C. S. *et al.* Cell Types of the Human Retina and Its Organoids at Single-Cell Resolution. *Cell* **182**, 1623-1640.e1634 (2020). https://doi.org:10.1016/j.cell.2020.08.013

34 Peng, Y. R. *et al.* Molecular Classification and Comparative Taxonomics of Foveal and Peripheral Cells in Primate Retina. *Cell* (2019). https://doi.org:10.1016/j.cell.2019.01.004

35 Kjer, B., Eiberg, H., Kjer, P. & Rosenberg, T. Dominant optic atrophy mapped to chromosome 3q region. II. Clinical and epidemiological aspects. *Acta Ophthalmol Scand* **74**, 3-7 (1996). https://doi.org:10.1111/j.1600-0420.1996.tb00672.x

36 Eiberg, H., Kjer, B., Kjer, P. & Rosenberg, T. Dominant optic atrophy (OPA1) mapped to chromosome 3q region. I. Linkage analysis. *Hum Mol Genet* **3**, 977-980 (1994). https://doi.org:10.1093/hmg/3.6.977

37 Kivlin, J. D., Lovrien, E. W., Bishop, D. T. & Maumenee, I. H. Linkage analysis in dominant optic atrophy. *American Journal of Human Genetics* (1983).

38 Yu-Wai-Man, P., Griffiths, P. G. & Chinnery, P. F. Mitochondrial optic neuropathies - disease mechanisms and therapeutic strategies. *Prog Retin Eye Res* **30**, 81-114 (2011). https://doi.org:10.1016/j.preteyeres.2010.11.002

39 Yu-Wai-Man, P. *et al.* The Prevalence and Natural History of Dominant Optic Atrophy Due to OPA1 Mutations. *Ophthalmology* **117**, 1538-1546.e1531 (2010). https://doi.org:https://doi.org/10.1016/j.ophtha.2009.12.038

40 Yu-Wai-Man, P. & Chinnery, P. F. Dominant Optic Atrophy: Novel OPA1 Mutations and Revised Prevalence Estimates. *Ophthalmology* **120**, 1712-1712.e1711 (2013). https://doi.org:https://doi.org/10.1016/j.ophtha.2013.04.022

41 Amati-Bonneau, P. *et al.* OPA1-associated disorders: phenotypes and pathophysiology. *Int J Biochem Cell Biol* **41**, 1855-1865 (2009). https://doi.org:10.1016/j.biocel.2009.04.012

42 Kjer, P. Infantile optic atrophy with dominant mode of inheritance: a clinical and genetic study of 19 Danish families. *Acta Ophthalmol Suppl* **164**, 1-147 (1959).

43 Eliott, D., Traboulsi, E. I. & Maumenee, I. H. Visual prognosis in autosomal dominant optic atrophy (Kjer type). *Am J Ophthalmol* **115**, 360-367 (1993). https://doi.org:10.1016/s0002-9394(14)73589-5

44 Han, J., Li, Y., You, Y., Fan, K. & Lei, B. Autosomal dominant optic atrophy caused by six novel pathogenic OPA1 variants and genotype-phenotype correlation analysis. *BMC Ophthalmol* **22**, 322 (2022). https://doi.org:10.1186/s12886-022-02546-0

45 Cohn, A. C. *et al.* Autosomal dominant optic atrophy: penetrance and expressivity in patients with OPA1 mutations. *Am J Ophthalmol* **143**, 656-662 (2007). https://doi.org:10.1016/j.ajo.2006.12.038

46 Barboni, P. *et al.* OPA1 mutations associated with dominant optic atrophy influence optic nerve head size. *Ophthalmology* **117**, 1547-1553 (2010). https://doi.org:10.1016/j.ophtha.2009.12.042

47 Barboni, P. *et al.* Retinal nerve fiber layer thickness in dominant optic atrophy measurements by optical coherence tomography and correlation with age. *Ophthalmology* **118**, 2076-2080 (2011). https://doi.org:10.1016/j.ophtha.2011.02.027

48 Delettre, C. *et al.* Mutation spectrum and splicing variants in the OPA1 gene. *Human Genetics* **109**, 584-591 (2001). https://doi.org:10.1007/s00439-001-0633-y

49 Toomes, C. *et al.* Spectrum, frequency and penetrance of OPA1 mutations in dominant optic atrophy. *Human Molecular Genetics* **10**, 1369-1378 (2001). https://doi.org:10.1093/hmg/10.13.1369

50 Le Roux, B. *et al.* OPA1: 516 unique variants and 831 patients registered in an updated centralized Variome database. *Orphanet Journal of Rare Diseases* **14**, 1-9 (2019). https://doi.org:10.1186/s13023-019-1187-1

51 Ferré, M. *et al.* Improved Locus-Specific Database for OPA1 Mutations Allows Inclusion of Advanced Clinical Data. *Human Mutation* **36**, 20-25 (2015). https://doi.org:https://doi.org/10.1002/humu.22703

52 Hoyt, C. S. Autosomal dominant optic atrophy. A spectrum of disability. *Ophthalmology* **87**, 245-251 (1980). https://doi.org:10.1016/s0161-6420(80)35247-0

53 Delettre, C., Lenaers, G., Pelloquin, L., Belenguer, P. & Hamel, C. P. OPA1 (Kjer type) dominant optic atrophy: a novel mitochondrial disease. *Mol Genet Metab* **75**, 97-107 (2002). https://doi.org:10.1006/mgme.2001.3278

54 Yu-Wai-Man, P. *et al.* Multi-system neurological disease is common in patients with OPA1 mutations. *Brain* **133**, 771-786 (2010). https://doi.org:10.1093/brain/awq007

55 Maeda-Katahira, A. *et al.* Autosomal dominant optic atrophy with OPA1 gene mutations accompanied by auditory neuropathy and other systemic complications in a Japanese cohort. *Mol Vis* **25**, 559-573 (2019).

56 Amati-Bonneau, P. *et al.* OPA1 mutations induce mitochondrial DNA instability and optic atrophy 'plus' phenotypes. *Brain* **131**, 338-351 (2008). https://doi.org:10.1093/brain/awm298

57 Treft, R. L. *et al.* Dominant optic atrophy, deafness, ptosis, ophthalmoplegia, dystaxia, and myopathy. A new syndrome. *Ophthalmology* **91**, 908-915 (1984). https://doi.org:10.1016/s0161-6420(84)34214-2

58 Carelli, V. *et al.* 'Behr syndrome' with OPA1 compound heterozygote mutations. *Brain* **138**, e321 (2015). https://doi.org:10.1093/brain/awu234

59 Othman, B. A., Ong, J. E. & Dumitrescu, A. V. Biallelic Optic Atrophy 1 (OPA1) Related Disorder-Case Report and Literature Review. *Genes (Basel)* **13** (2022). https://doi.org:10.3390/genes13061005

60 Zerem, A. *et al.* Metabolic stroke in a patient with bi-allelic OPA1 mutations. *Metab Brain Dis* **34**, 1043-1048 (2019). https://doi.org:10.1007/s11011-019-00415-2

61 Lee, J. *et al.* Recessive optic atrophy, sensorimotor neuropathy and cataract associated with novel compound heterozygous mutations in OPA1. *Mol Med Rep* **14**, 33-40 (2016). https://doi.org:10.3892/mmr.2016.5209

62 Schaaf, C. P. *et al.* Early-onset severe neuromuscular phenotype associated with compound heterozygosity for OPA1 mutations. *Molecular Genetics and Metabolism* **103**, 383-387 (2011). https://doi.org:10.1016/j.ymgme.2011.04.018

63 Bonneau, D. *et al.* Early-onset Behr syndrome due to compound heterozygous mutations in OPA1. *Brain* **137**, e301 (2014). https://doi.org:10.1093/brain/awu184

64 Nasca, A. *et al.* Not only dominant, not only optic atrophy: expanding the clinical spectrum associated with OPA1 mutations. *Orphanet Journal of Rare Diseases* **12**, 1-10 (2017). https://doi.org:10.1186/s13023-017-0641-1

65 Lenaers, G. *et al.* Dominant optic atrophy: Culprit mitochondria in the optic nerve. *Progress in retinal and eye research* **83**, 100935-100935 (2021). https://doi.org:10.1016/j.preteyeres.2020.100935

66 Cerrada, V. *et al.* Derivation of a human DOA iPSC line, IISHDOi006-A, with a mutation in the ACO2 gene: c.1999G>A; p.Glu667Lys. *Stem Cell Research* **40**, 101566-101566 (2019). https://doi.org:10.1016/j.scr.2019.101566

67 Carelli, V. *et al.* Idebenone Treatment In Leber's Hereditary Optic Neuropathy. *Brain* **134**, e188-e188 (2011). https://doi.org:10.1093/brain/awr180

68 Romagnoli, M. *et al.* Idebenone increases chance of stabilization/recovery of visual acuity in OPA1-dominant optic atrophy. *Annals of Clinical and Translational Neurology* **7**, 590-594 (2020). https://doi.org:10.1002/acn3.51026

69 Mordente, A., Martorana, G. E., Minotti, G. & Giardina, B. Antioxidant Properties of 2,3-Dimethoxy-5-methyl- 6-(10-hydroxydecyl)-1,4-benzoquinone (Idebenone). *Chemical Research in Toxicology* **11**, 54-63 (1998). https://doi.org:10.1021/tx970136j

70 Willems, Peter H. G. M., Rossignol, R., Dieteren, Cindy E. J., Murphy, Michael P. & Koopman, Werner J. H. Redox Homeostasis and Mitochondrial Dynamics. *Cell Metabolism* **22**, 207-218 (2015). https://doi.org:10.1016/j.cmet.2015.06.006

71 Millet, A. M. C. *et al.* Loss of functional OPA1 unbalances redox state: Implications in dominant optic atrophy pathogenesis. *Annals of Clinical and Translational Neurology* (2016). https://doi.org:10.1002/acn3.305

72 Quintana-Cabrera, R. *et al.* Opa1 relies on cristae preservation and ATP synthase to curtail reactive oxygen species accumulation in mitochondria. *Redox Biology* **41** (2021). https://doi.org:10.1016/j.redox.2021.101944

73 Zhang, J. *et al.* A novel ADOA-associated OPA1 mutation alters the mitochondrial function, membrane potential, ROS production and apoptosis. *Scientific Reports* (2017). https://doi.org:10.1038/s41598-017-05571-y

74 Haefeli, R. H. *et al.* NQO1-Dependent Redox Cycling of Idebenone: Effects on Cellular Redox Potential and Energy Levels. *PLOS ONE* **6**, e17963 (2011). https://doi.org:10.1371/journal.pone.0017963

75 Zanna, C. *et al.* OPA1 mutations associated with dominant optic atrophy impair oxidative phosphorylation and mitochondrial fusion. *Brain* (2008). https://doi.org:10.1093/brain/awm335

76 Kutz, K., Drewe, J. & Vankan, P. Pharmacokinetic properties and metabolism of idebenone. *Journal of Neurology* **256**, 31-35 (2009). https://doi.org:10.1007/s00415-009-1006-z

77 Carelli, V. *et al.* International Consensus Statement on the Clinical and Therapeutic Management of Leber Hereditary Optic Neuropathy. *Journal of Neuro-Ophthalmology* **37** (2017).

78 Ahmed, Z., Suggate, E. L., Logan, A. & Berry, M. Retinal Ganglion Cell Survival and Axon Regeneration after Optic Nerve Transection is Driven by Cellular Intravitreal Sciatic Nerve Grafts. *Cells* **9** (2020). https://doi.org:10.3390/cells9061335

79 Vrathasha, V. *et al.* Transplanted human induced pluripotent stem cells- derived retinal ganglion cells embed within mouse retinas and are electrophysiologically functional. *iScience* **25**, 105308 (2022). https://doi.org:10.1016/j.isci.2022.105308

80 Zhou, H. *et al.* Glia-to-Neuron Conversion by CRISPR-CasRx Alleviates Symptoms of Neurological Disease in Mice. *Cell* **181**, 590-603.e516 (2020). https://doi.org:10.1016/j.cell.2020.03.024

81 Aijaz, S., Erskine, L., Jeffery, G., Bhattacharya, S. S. & Votruba, M. Developmental expression profile of the optic atrophy gene product: OPA1 is not localized exclusively in the mammalian retinal ganglion cell layer. *Investigative Ophthalmology and Visual Science* **45**, 1667-1673 (2004). https://doi.org:10.1167/iovs.03-1093

82 Del Dotto, V. *et al.* OPA1 Isoforms in the Hierarchical Organization of Mitochondrial Functions. *Cell Reports* **19**, 2557-2571 (2017). https://doi.org:10.1016/j.celrep.2017.05.073

83 Maloney, D. M. *et al.* Optimized OPA1 Isoforms 1 and 7 Provide Therapeutic Benefit in Models of Mitochondrial Dysfunction. *Frontiers in Neuroscience* **14**, 1-19 (2020). https://doi.org:10.3389/fnins.2020.571479

84 Sarzi, E. *et al.* OPA1 gene therapy prevents retinal ganglion cell loss in a Dominant Optic Atrophy mouse model. *Scientific Reports* **8**, 1-6 (2018). https://doi.org:10.1038/s41598-018-20838-8

85 Griparic, L., Van Der Wel, N. N., Orozco, I. J., Peters, P. J. & Van Der Bliek, A. M. Loss of the Intermembrane Space Protein Mgm1/OPA1 Induces Swelling and Localized Constrictions along the Lengths of Mitochondria. *Journal of Biological Chemistry* **279**, 18792-18798 (2004). https://doi.org:10.1074/jbc.M400920200

86 Olichon, A. *et al.* Effects of OPA1 mutations on mitochondrial morphology and apoptosis: Relevance to ADOA pathogenesis. *Journal of Cellular Physiology* **211**, 423-430 (2007). https://doi.org:https://doi.org/10.1002/jcp.20950

87 Sarzi, E. *et al.* The human OPA1^{delTTAG} mutation induces premature age-related systemic neurodegeneration in mouse. *Brain* **135**, 3599-3613 (2012). https://doi.org:10.1093/brain/aws303

88 Alavi, M. V. *et al.* A splice site mutation in the murine Opa1 gene features pathology of autosomal dominant optic atrophy. *Brain* **130**, 1029-1042 (2007). https://doi.org:10.1093/brain/awm005

89 Davies, V. J. *et al.* Opa1 deficiency in a mouse model of autosomal dominant optic atrophy impairs mitochondrial morphology, optic nerve structure and visual function. *Human Molecular Genetics* **16**, 1307-1318 (2007). https://doi.org:10.1093/hmg/ddm079

90 Akepati, V. R. *et al.* Characterization of OPA1 isoforms isolated from mouse tissues. *Journal of Neurochemistry* **106**, 372-383 (2008). https://doi.org:10.1111/j.1471-4159.2008.05401.x

91 Olichon, A. *et al.* The human dynamin-related protein OPA1 is anchored to the mitochondrial inner membrane facing the inter-membrane space. *FEBS Letters* **523**, 171-176 (2002). https://doi.org:10.1016/S0014-5793(02)02985-X

92 Ishihara, N., Fujita, Y., Oka, T. & Mihara, K. Regulation of mitochondrial morphology through proteolytic cleavage of OPA1. *EMBO Journal* **25**, 2966-2977 (2006). https://doi.org:10.1038/sj.emboj.7601184

93 Wang, R. *et al.* Identification of new OPA1 cleavage site reveals that short isoforms regulate mitochondrial fusion. *Molecular Biology of the Cell* **32**, 157-168 (2021). https://doi.org:10.1091/MBC.E20-09-0605

94 Song, Z., Chen, H., Fiket, M., Alexander, C. & Chan, D. C. OPA1 processing controls mitochondrial fusion and is regulated by mRNA splicing, membrane potential, and Yme1L. *Journal of Cell Biology* **178**, 749-755 (2007). https://doi.org:10.1083/jcb.200704110

95 Griparic, L., Kanazawa, T. & Van Der Bliek, A. M. Regulation of the mitochondrial dynamin-like protein Opa1 by proteolytic cleavage. *Journal of Cell Biology* **178**, 757-764 (2007). https://doi.org:10.1083/jcb.200704112

96 Del Dotto, V., Fogazza, M., Carelli, V., Rugolo, M. & Zanna, C. Eight human OPA1 isoforms, long and short: What are they for? *Biochimica et Biophysica Acta - Bioenergetics* **1859**, 263-269 (2018). https://doi.org:10.1016/j.bbabio.2018.01.005

97 Olichon, A. *et al.* OPA1 alternate splicing uncouples an evolutionary conserved function in mitochondrial fusion from a vertebrate restricted function in apoptosis. *Cell Death and Differentiation* **14**, 682-692 (2007). https://doi.org:10.1038/sj.cdd.4402048

98 Kamei, S. *et al.* Expression of the Opa1 mitochondrial protein in retinal ganglion cells: Its downregulation causes aggregation of the mitochondrial network. *Investigative Ophthalmology and Visual Science* **46**, 4288-4294 (2005). https://doi.org:10.1167/iovs.03-1407

99 Head, B., Griparic, L., Amiri, M., Gandre-Babbe, S. & Van Der Bliek, A. M. Inducible proteolytic inactivation of OPA1 mediated by the OMA1 protease in mammalian cells. *Journal of Cell Biology* (2009). https://doi.org:10.1083/jcb.200906083

100 Ehses, S. *et al.* Regulation of OPA1 processing and mitochondrial fusion by m-AAA protease isoenzymes and OMA1. *Journal of Cell Biology* (2009). https://doi.org:10.1083/jcb.200906084

101 Wang, A. G., Fann, M. J., Yu, H. Y. & Yen, M. Y. OPA1 expression in the human retina and optic nerve. *Experimental Eye Research* **83**, 1171-1178 (2006). https://doi.org:10.1016/j.exer.2006.06.004

102 Pesch, U. E. A. *et al.* OPA1, the disease gene for autosomal dominant optic atrophy, is specifically expressed in ganglion cells and intrinsic neurons of the retina. *Investigative Ophthalmology and Visual Science* **45**, 4217-4225 (2004). https://doi.org:10.1167/iovs.03-1261

103 Belenguer, P. & Pellegrini, L. The dynamin GTPase OPA1: More than mitochondria? *Biochimica et Biophysica Acta - Molecular Cell Research* **1833**, 176-183 (2013). https://doi.org:10.1016/j.bbamcr.2012.08.004

104 Ferré, M. *et al.* Molecular screening of 980 cases of suspected hereditary optic neuropathy with a report on 77 novel OPA1 mutations. *Human Mutation* **30**, 692-705 (2009). https://doi.org:10.1002/humu.21025

105 Griparic, L. & Van Der Bliek, A. M. Assay and properties of the mitochondrial dynamin related protein Opa1. *Methods in Enzymology* **404**, 620-631 (2005). https://doi.org:10.1016/S0076-6879(05)04054-1

106 Li, D., Wang, J., Jin, Z. & Zhang, Z. Structural and evolutionary characteristics of dynamin-related GTPase OPA1. *PeerJ* **7**, e7285 (2019). https://doi.org:10.7717/peerj.7285

107 Lee, H. & Yoon, Y. Mitochondrial membrane dynamics—functional positioning of OPA1. *Antioxidants* (2018). https://doi.org:10.3390/antiox7120186

108 Olichon, A. *et al.* in *Biochimica et Biophysica Acta - Molecular Cell Research* (2006).

109 Cipolat, S., De Brito, O. M., Dal Zilio, B. & Scorrano, L. OPA1 requires mitofusin 1 to promote mitochondrial fusion. *Proceedings of the National Academy of Sciences of the United States of America* (2004). https://doi.org:10.1073/pnas.0407043101

110 Chen, H. *et al.* Mitofusins Mfn1 and Mfn2 coordinately regulate mitochondrial fusion and are essential for embryonic development. *Journal of Cell Biology* (2003). https://doi.org:10.1083/jcb.200211046

111 Ban, T. *et al.* Molecular basis of selective mitochondrial fusion by heterotypic action between OPA1 and cardiolipin. *Nature Cell Biology* **19**, 856-863 (2017). https://doi.org:10.1038/ncb3560

112 Anand, R. *et al.* The i-AAA protease YME1L and OMA1 cleave OPA1 to balance mitochondrial fusion and fission. *The Journal of cell biology* **204**, 919-929 (2014). https://doi.org:10.1083/jcb.201308006

113 Lee, H., Smith, S. B. & Yoon, Y. The short variant of the mitochondrial dynamin OPA1 maintains mitochondrial energetics and cristae structure. *Journal of Biological Chemistry* **292**, 7115-7130 (2017). https://doi.org:10.1074/jbc.M116.762567

114 Gomes, L. C., Benedetto, G. D. & Scorrano, L. During autophagy mitochondria elongate, are spared from degradation and sustain cell viability. *Nature Cell Biology* (2011). https://doi.org:10.1038/ncb2220

115 Strauss, M., Hofhaus, G., Schröder, R. R. & Kühlbrandt, W. Dimer ribbons of ATP synthase shape the inner mitochondrial membrane. *EMBO Journal* (2008). https://doi.org:10.1038/emboj.2008.35

116 Rambold, A. S., Kostelecky, B., Elia, N. & Lippincott-Schwartz, J. Tubular network formation protects mitochondria from autophagosomal degradation during nutrient starvation. *Proceedings of the National Academy of Sciences of the United States of America* (2011). https://doi.org:10.1073/pnas.1107402108

117 Frezza, C. *et al.* OPA1 Controls Apoptotic Cristae Remodeling Independently from Mitochondrial Fusion. *Cell* (2006). https://doi.org:10.1016/j.cell.2006.06.025

118 Cogliati, S. *et al.* Mitochondrial cristae shape determines respiratory chain supercomplexes assembly and respiratory efficiency. *Cell* (2013). https://doi.org:10.1016/j.cell.2013.08.032

119 Arnoult, D., Grodet, A., Lee, Y. J., Estaquier, J. & Blackstone, C. Release of OPA1 during apoptosis participates in the rapid and complete release of cytochrome c and

subsequent mitochondrial fragmentation. *Journal of Biological Chemistry* (2005). https://doi.org:10.1074/jbc.M505970200

120 Alavi, M. V. & Fuhrmann, N. Dominant optic atrophy, OPA1, and mitochondrial quality control: Understanding mitochondrial network dynamics. *Molecular Neurodegeneration* **8** (2013). https://doi.org:10.1186/1750-1326-8-32

121 Kang, E. Y.-C. *et al.* Role of Oxidative Stress in Ocular Diseases Associated with Retinal Ganglion Cells Degeneration. *Antioxidants (Basel, Switzerland)* **10** (2021). https://doi.org:10.3390/antiox10121948

122 Pham, J. H. & Stankowska, D. L. Mitochondria-associated endoplasmic reticulum membranes (MAMs) and their role in glaucomatous retinal ganglion cell degeneration—a mini review. *Frontiers in Neuroscience* **17** (2023). https://doi.org:10.3389/fnins.2023.1198343

123 Agier, V. *et al.* Defective mitochondrial fusion, altered respiratory function, and distorted cristae structure in skin fibroblasts with heterozygous OPA1 mutations. *Biochimica et Biophysica Acta - Molecular Basis of Disease* **1822**, 1570-1580 (2012). https://doi.org:10.1016/j.bbadis.2012.07.002

124 Iannielli, A. *et al.* Pharmacological Inhibition of Necroptosis Protects from Dopaminergic Neuronal Cell Death in Parkinson's Disease Models. *Cell Reports* **22**, 2066-2079 (2018). https://doi.org:10.1016/j.celrep.2018.01.089

125 Yarosh, W. *et al.* The Molecular Mechanisms of OPA1-Mediated Optic Atrophy in Drosophila Model and Prospects for Antioxidant Treatment. *PLOS Genetics* **4**, e6 (2008). https://doi.org:10.1371/journal.pgen.0040006

126 Kuwahara, A. *et al.* Generation of a ciliary margin-like stem cell niche from self-organizing human retinal tissue. *Nature Communications* (2015). https://doi.org:10.1038/ncomms7286

127 Ohlemacher, S. K., Iglesias, C. L., Sridhar, A., Gamm, D. M. & Meyer, J. S. Generation of highly enriched populations of optic vesicle-like retinal cells from human pluripotent stem cells. *Current Protocols in Stem Cell Biology* (2015). https://doi.org:10.1002/9780470151808.sc01h08s32

128 Langer, K. B. *et al.* Retinal Ganglion Cell Diversity and Subtype Specification from Human Pluripotent Stem Cells. *Stem Cell Reports* **10**, 1282-1293 (2018). https://doi.org:10.1016/j.stemcr.2018.02.010

129 Jonikas, M. *et al.* Stem cell modeling of mitochondrial parkinsonism reveals key functions of OPA1. *Annals of Neurology* **83**, 915-925 (2018). https://doi.org:10.1002/ana.25221

130 Cartes-Saavedra, B. *et al.* OPA1 disease-causing mutants have domain-specific effects on mitochondrial ultrastructure and fusion. *Proc Natl Acad Sci U S A* **120**, e2207471120 (2023). https://doi.org:10.1073/pnas.2207471120

131 Thiselton, D. L. *et al.* A comprehensive survey of mutations in the OPA1 gene in patients with autosomal dominant optic atrophy. *Invest Ophthalmol Vis Sci* **43**, 1715-1724 (2002).

132 Sladen, P. E. *et al.* Modelling autosomal dominant optic atrophy associated with OPA1 variants in iPSC-derived retinal ganglion cells. *Hum Mol Genet* **31**, 3478-3493 (2022). https://doi.org:10.1093/hmg/ddac128

133 Sun, Z. *et al.* Generation of a human induced pluripotent stem cell line PUMCHi019-A from a dominant optic atrophy patient with an OPA1 mutation. *Stem Cell Research* **60**, 102705 (2022). https://doi.org:https://doi.org/10.1016/j.scr.2022.102705

134 Sladen, P. E. *et al.* CRISPR-Cas9 correction of OPA1 c.1334G>A: p.R445H restores mitochondrial homeostasis in dominant optic atrophy patient-derived iPSCs. *Molecular Therapy - Nucleic Acids* **26**, 432-443 (2021). https://doi.org:10.1016/j.omtn.2021.08.015

135 Chan, Y. H. *et al.* Generation of induced pluripotent stem cells from a patient with hearing loss carrying OPA1 c.1468T>C (p.Cys490Arg) variant. *Stem Cell Res* **64**, 102903 (2022). https://doi.org:10.1016/j.scr.2022.102903

136 Galera-Monge, T. *et al.* Generation of a human iPSC line from a patient with an optic atrophy 'plus' phenotype due to a mutation in the OPA1 gene. *Stem Cell Res* **16**, 673-676 (2016). https://doi.org:10.1016/j.scr.2016.03.011

137 Zurita-Díaz, F. *et al.* Establishment of a human DOA 'plus' iPSC line, IISHDOi003-A, with the mutation in the OPA1 gene: c.1635C>A; p.Ser545Arg. *Stem Cell Research* **24**, 81-84 (2017). https://doi.org:https://doi.org/10.1016/j.scr.2017.08.017

138 Chen, J., Riazifar, H., Guan, M. X. & Huang, T. Modeling autosomal dominant optic atrophy using induced pluripotent stem cells and identifying potential therapeutic targets. *Stem Cell Research and Therapy* **7**, 1-14 (2016). https://doi.org:10.1186/s13287-015-0264-1

139 Zhang, X. H., Xie, Y., Xu, K. & Li, Y. Generation of an induced pluripotent stem cell line BIOi002-A from a patient with autosomal dominant optic atrophy. *Stem Cell Research* **53**, 17-20 (2021). https://doi.org:10.1016/j.scr.2021.102278

140 Weisschuh, N. *et al.* Mutation spectrum of the OPA1 gene in a large cohort of patients with suspected dominant optic atrophy: Identification and classification of 48 novel variants. *PLoS ONE* **16**, 1-22 (2021). https://doi.org:10.1371/journal.pone.0253987

141 Chavali, V. R. M. *et al.* Dual SMAD inhibition and Wnt inhibition enable efficient and reproducible differentiations of induced pluripotent stem cells into retinal ganglion cells. *Scientific Reports* **10**, 1-14 (2020). https://doi.org:10.1038/s41598-020-68811-8

142 Sluch, V. M. *et al.* Enhanced Stem Cell Differentiation and Immunopurification of Genome Engineered Human Retinal Ganglion Cells. *Stem Cells Translational Medicine* **6**, 1972-1986 (2017). https://doi.org:10.1002/sctm.17-0059

143 Fligor, C. M., Huang, K. C., Lavekar, S. S., VanderWall, K. B. & Meyer, J. S. *Differentiation of retinal organoids from human pluripotent stem cells*. 1 edn, Vol. 159 (Elsevier Inc., 2020).

144 Meyer, J. S. *et al.* Optic Vesicle-like Structures Derived from Human Pluripotent Stem Cells Facilitate a Customized Approach to Retinal Disease Treatment. *Stem Cells* **29**, 1206-1218 (2011). https://doi.org:10.1002/stem.674

145 Nakano, T. *et al.* Self-Formation of Optic Cups and Storable Stratified Neural Retina from Human ESCs. *Cell Stem Cell* **10**, 771-785 (2012). https://doi.org:10.1016/j.stem.2012.05.009

146 García-López, M., Arenas, J. & Gallardo, M. E. Hereditary Optic Neuropathies: Induced Pluripotent Stem Cell-Based 2D/3D Approaches. *Genes* **12** (2021). https://doi.org:10.3390/genes12010112

147 Fligor, C. M. *et al.* Three-Dimensional Retinal Organoids Facilitate the Investigation of Retinal Ganglion Cell Development, Organization and Neurite Outgrowth from Human Pluripotent Stem Cells. *Scientific Reports* **8**, 1-14 (2018). https://doi.org:10.1038/s41598-018-32871-8

148 Zhang, X. *et al.* in *Frontiers in Cell and Developmental Biology* Vol. 9 (2021).

149 Reichman, S. *et al.* From confluent human iPS cells to self-forming neural retina and retinal pigmented epithelium. *Proceedings of the National Academy of Sciences of the United States of America* (2014). https://doi.org:10.1073/pnas.1324212111

150 Capowski, E. E. *et al.* Reproducibility and staging of 3D human retinal organoids across multiple pluripotent stem cell lines. *Development (Cambridge)* **146** (2019). https://doi.org:10.1242/dev.171686

151 Olichon, A. *et al.* Loss of OPA1 perturbates the mitochondrial inner membrane structure and integrity, leading to cytochrome c release and apoptosis. *J Biol Chem* **278**, 7743-7746 (2003). https://doi.org:10.1074/jbc.C200677200

152 Olichon, A. *et al.* OPA1 alternate splicing uncouples an evolutionary conserved function in mitochondrial fusion from a vertebrate restricted function in apoptosis. *Cell Death Differ* **14**, 682-692 (2007). https://doi.org:10.1038/sj.cdd.4402048

153 Cipolat, S., Martins de Brito, O., Dal Zilio, B. & Scorrano, L. OPA1 requires mitofusin 1 to promote mitochondrial fusion. *Proc Natl Acad Sci U S A* **101**, 15927-15932 (2004). https://doi.org:10.1073/pnas.0407043101

154 Frezza, C. *et al.* OPA1 controls apoptotic cristae remodeling independently from mitochondrial fusion. *Cell* **126**, 177-189 (2006). https://doi.org:10.1016/j.cell.2006.06.025

155 Quintana-Cabrera, R. *et al.* The cristae modulator Optic atrophy 1 requires mitochondrial ATP synthase oligomers to safeguard mitochondrial function. *Nat Commun* **9**, 3399 (2018). https://doi.org:10.1038/s41467-018-05655-x

156 Agier, V. *et al.* Defective mitochondrial fusion, altered respiratory function, and distorted cristae structure in skin fibroblasts with heterozygous OPA1 mutations. *Biochim Biophys Acta* **1822**, 1570-1580 (2012). https://doi.org:10.1016/j.bbadis.2012.07.002

157 Ramonet, D. *et al.* Optic atrophy 1 mediates mitochondria remodeling and dopaminergic neurodegeneration linked to complex I deficiency. *Cell Death Differ* **20**, 77-85 (2013). https://doi.org:10.1038/cdd.2012.95

158 Le Roux, B. *et al.* OPA1: 516 unique variants and 831 patients registered in an updated centralized Variome database. *Orphanet J Rare Dis* **14**, 214 (2019). https://doi.org:10.1186/s13023-019-1187-1

159 Chao de la Barca, J. M. *et al.* Metabolomics hallmarks OPA1 variants correlating with their in vitro phenotype and predicting clinical severity. *Hum Mol Genet* **29**, 1319-1329 (2020). https://doi.org:10.1093/hmg/ddaa047

160 Osakada, F., Ikeda, H., Sasai, Y. & Takahashi, M. Stepwise differentiation of pluripotent stem cells into retinal cells. *Nat Protoc* **4**, 811-824 (2009). https://doi.org:10.1038/nprot.2009.51

161 Ohlemacher, S. K., Iglesias, C. L., Sridhar, A., Gamm, D. M. & Meyer, J. S. Generation of highly enriched populations of optic vesicle-like retinal cells from human pluripotent stem cells. *Curr Protoc Stem Cell Biol* **32**, 1H 8 1-1H 8 20 (2015). https://doi.org:10.1002/9780470151808.sc01h08s32

162 Rabesandratana, O. *et al.* Generation of a Transplantable Population of Human iPSC-Derived Retinal Ganglion Cells. *Front Cell Dev Biol* **8**, 585675 (2020). https://doi.org:10.3389/fcell.2020.585675

163 Sluch, V. M. *et al.* Enhanced Stem Cell Differentiation and Immunopurification of Genome Engineered Human Retinal Ganglion Cells. *Stem Cells Transl Med* **6**, 1972-1986 (2017). https://doi.org:10.1002/sctm.17-0059

164 Zhang, X. *et al.* Single Cell Transcriptomic Analyses Reveal the Impact of bHLH Factors on Human Retinal Organoid Development. *Front Cell Dev Biol* **9**, 653305 (2021). https://doi.org:10.3389/fcell.2021.653305

165 Chen, J., Riazifar, H., Guan, M. X. & Huang, T. Modeling autosomal dominant optic atrophy using induced pluripotent stem cells and identifying potential therapeutic targets. *Stem Cell Res Ther* **7**, 2 (2016). https://doi.org:10.1186/s13287-015-0264-1

166 Zurita-Diaz, F. *et al.* Establishment of a human DOA 'plus' iPSC line, IISHDOi003-A, with the mutation in the OPA1 gene: c.1635C>A; p.Ser545Arg. *Stem Cell Res* **24**, 81-84 (2017). https://doi.org:10.1016/j.scr.2017.08.017

167 Sun, Z. *et al.* Generation of a human induced pluripotent stem cell line PUMCHi019-A from a dominant optic atrophy patient with an OPA1 mutation. *Stem Cell Res* **60**, 102705 (2022). https://doi.org:10.1016/j.scr.2022.102705

168 Zhang, X. H., Xie, Y., Xu, K. & Li, Y. Generation of an induced pluripotent stem cell line BIOi002-A from a patient with autosomal dominant optic atrophy. *Stem Cell Res* **53**, 102278 (2021). https://doi.org:10.1016/j.scr.2021.102278

169 Jonikas, M. *et al.* Stem cell modeling of mitochondrial parkinsonism reveals key functions of OPA1. *Ann Neurol* **83**, 915-925 (2018). https://doi.org:10.1002/ana.25221

170 Toombs, J. *et al.* Generation of twenty four induced pluripotent stem cell lines from twenty four members of the Lothian Birth Cohort 1936. *Stem Cell Res* **46**, 101851 (2020). https://doi.org:10.1016/j.scr.2020.101851

171 Okita, K. *et al.* An efficient nonviral method to generate integration-free human-induced pluripotent stem cells from cord blood and peripheral blood cells. *Stem Cells* **31**, 458-466 (2013). https://doi.org:10.1002/stem.1293

172 Song, Z., Ghochani, M., McCaffery, J. M., Frey, T. G. & Chan, D. C. Mitofusins and OPA1 Mediate Sequential Steps in Mitochondrial Membrane Fusion. *Molecular Biology of the Cell* **20**, 3525-3532 (2009). https://doi.org:10.1091/mbc.e09-03-0252

173 Amati-Bonneau, P. *et al.* OPA1 R445H mutation in optic atrophy associated with sensorineural deafness. *Annals of Neurology* **58**, 958-963 (2005). https://doi.org:https://doi.org/10.1002/ana.20681

174 Chevrollier, A. *et al.* Hereditary optic neuropathies share a common mitochondrial coupling defect. *Annals of Neurology* **63**, 794-798 (2008). https://doi.org:https://doi.org/10.1002/ana.21385

175 Barron, M. J., Griffiths, P., Turnbull, D. M., Bates, D. & Nichols, P. The distributions of mitochondria and sodium channels reflect the specific energy requirements and conduction properties of the human optic nerve head. *Br J Ophthalmol* **88**, 286-290 (2004). https://doi.org:10.1136/bjo.2003.027664

176 Andrews, R. M., Griffiths, P. G., Johnson, M. A. & Turnbull, D. M. Histochemical localisation of mitochondrial enzyme activity in human optic nerve and retina. *Br J Ophthalmol* **83**, 231-235 (1999). https://doi.org:10.1136/bjo.83.2.231

177 Yu, D. Y. *et al.* Retinal ganglion cells: Energetics, compartmentation, axonal transport, cytoskeletons and vulnerability. *Progress in Retinal and Eye Research* **36**, 217-246 (2013). https://doi.org:10.1016/j.preteyeres.2013.07.001

178 Hsiau, T. *et al.* Inference of CRISPR Edits from Sanger Trace Data. *bioRxiv* (2018). https://doi.org:10.1101/251082

179 Ioannidis, N. M. *et al.* REVEL: An Ensemble Method for Predicting the Pathogenicity of Rare Missense Variants. *The American Journal of Human Genetics* **99**, 877-885 (2016). https://doi.org:10.1016/j.ajhg.2016.08.016

180 Skarnes, W. C., Pellegrino, E. & McDonough, J. A. Improving homology-directed repair efficiency in human stem cells. *Methods* **164-165**, 18-28 (2019). https://doi.org:10.1016/j.ymeth.2019.06.016

181 Choi, J. *et al.* A comparison of genetically matched cell lines reveals the equivalence of human iPSCs and ESCs. *Nature Biotechnology* **33**, 1173-1181 (2015). https://doi.org:10.1038/nbt.3388

182 Burrows, C. K. *et al.* Genetic Variation, Not Cell Type of Origin, Underlies the Majority of Identifiable Regulatory Differences in iPSCs. *PLOS Genetics* **12**, e1005793 (2016). https://doi.org:10.1371/journal.pgen.1005793

183 Olmer, R., Kropp, C. & Zweigerdt, R. Impact of Feeding Strategies on Expansion of Human Pluripotent Stem Cells in Stirred Tank Bioreactors Using mTeSR1. 4 (Leibniz Research Laboratories for Biotechnology and Artificial Organs (LEBAO), REBIRTH Cluster of Excellence, Hannover Medical School, Hannover, Germany, 2015).

184 Gu, W. *et al.* Glycolytic Metabolism Plays a Functional Role in Regulating Human Pluripotent Stem Cell State. *Cell Stem Cell* (2016). https://doi.org:10.1016/j.stem.2016.08.008

185 Sun, S., Erchova, I., Sengpiel, F. & Votruba, M. Opa1 deficiency leads to diminished mitochondrial bioenergetics with compensatory increased mitochondrial motility. *Investigative Ophthalmology and Visual Science* **61** (2020). https://doi.org:10.1167/IOVS.61.6.42

186 Divakaruni, A. S., Paradyse, A., Ferrick, D. A., Murphy, A. N. & Jastroch, M. in *Methods in Enzymology* Vol. 547 (eds Anne N. Murphy & David C. Chan) 309-354 (Academic Press, 2014).

187 Divakaruni, A. S. *et al.* Inhibition of the mitochondrial pyruvate carrier protects from excitotoxic neuronal death. *Journal of Cell Biology* **216**, 1091-1105 (2017). https://doi.org:10.1083/jcb.201612067

188 Del Dotto, V. *et al.* OPA1: How much do we know to approach therapy? *Pharmacological Research* **131**, 199-210 (2018). https://doi.org:10.1016/j.phrs.2018.02.018

189 Driehuis, E. & Clevers, H. CRISPR/Cas 9 genome editing and its applications in organoids. *American Journal of Physiology-Gastrointestinal and Liver Physiology* **312**, G257-G265 (2017). https://doi.org:10.1152/ajpgi.00410.2016

190 Riazifar, H., Jia, Y., Chen, J., Lynch, G. & Huang, T. Chemically Induced Specification of Retinal Ganglion Cells From Human Embryonic and Induced Pluripotent Stem Cells. *Stem Cells Translational Medicine* **3**, 424-432 (2014). https://doi.org:10.5966/sctm.2013-0147

191 Yoon, S.-J. *et al.* Reliability of human cortical organoid generation. *Nature Methods* **16**, 75-78 (2019). https://doi.org:10.1038/s41592-018-0255-0

192 Li, X., Zhang, L., Tang, F. & Wei, X. Retinal Organoids: Cultivation, Differentiation, and Transplantation. *Frontiers in Cellular Neuroscience* **15** (2021). https://doi.org:10.3389/fncel.2021.638439